Universidad Carlos III de Madrid

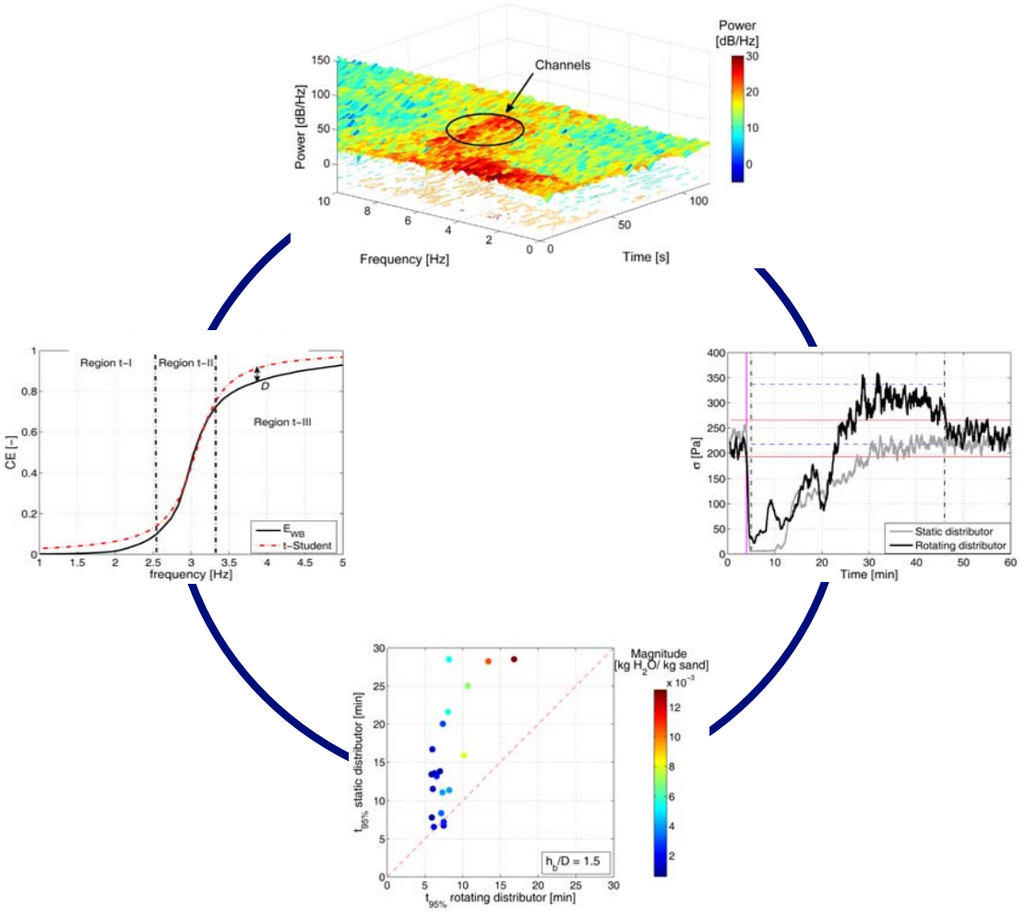

PASTE DRYING CONTROL IN A ROTATING-DISTRIBUTOR FLUIDIZED BED

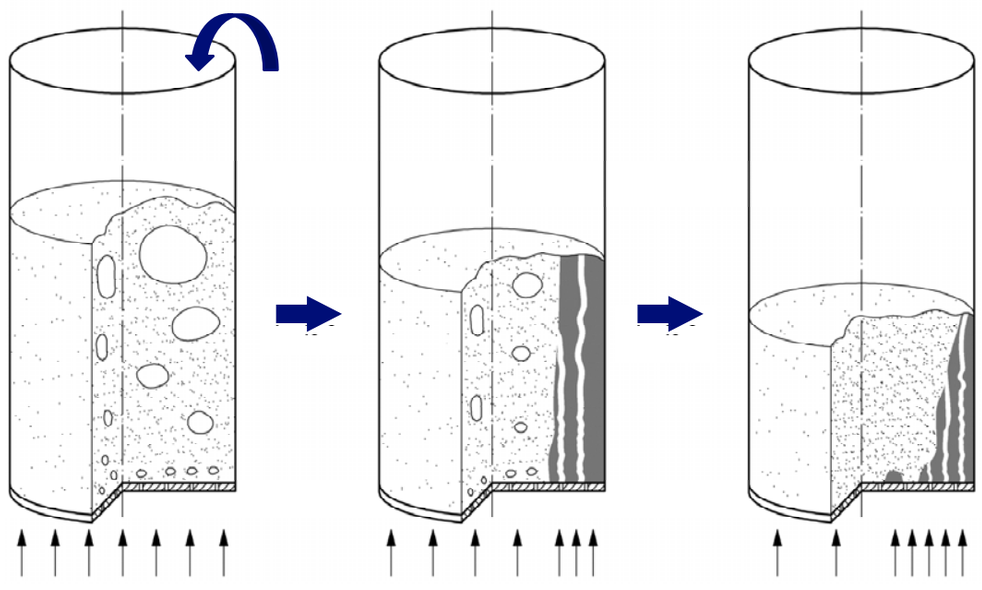

PASTE DRYING CONTROL IN A ROTATING-DISTRIBUTOR FLUIDIZED BED

JGH - 2014

Jesús Gómez Hernández

PhD Thesis

ISE RESEARCH GROUP
Dpto. Ingeniería Térmica y de Fluidos
Universidad Carlos III de Madrid
Leganés (Madrid, SPAIN), Dec. 2014

Tesis doctoral

Paste drying control in a rotating-distributor fluidized bed

Autor: Jesús Gómez Hernández

Director de Tesis: Domingo Santana Santana
Co-director de Tesis: Javier Villa Briongos

Firma del Tribunal Calificador:

Firma

Presidente:	Dr. Martin Olazar Aurrecoechea, Universidad del País Vasco
Secretario:	Dra. Lilian de Martín Montón, University College of London
Vocal:	Dr. David Pallarès i Tella, Chalmers University of Technology
Suplente:	Dra. Celia Sobrino Fernández, Universidad Carlos III de Madrid

Calificación:

Leganés (Madrid), 5 de Diciembre de 2014

A mis padres y a mi hermano,
fuente de toda mi resistencia.

DEPARTAMENTO DE INGENIERÍA TÉRMICA Y DE FLUIDOS
Escuela Politécnica Superior

Paste drying control in a rotating-distributor fluidized bed

Autor
Jesús Gómez Hernández

Director de Tesis
Domingo Santana Santana
Co-director de Tesis
Javier Villa Briongos

Leganés (Madrid), Diciembre 2014

Agradecimientos

Para terminar de escribir una tesis es fundamental tener la parte de los agradecimientos bien clara, ya que, una vez escrita, el resto está hecho. Así, aquí toca remarcar con palabras a los que, de una forma u otra, me han ayudado a recorrer este camino. Empezando por mis compañeros de trabajo, en primer lugar quiero agradecer el apoyo recibido de mis directores Domingo Santana y Javier Villa, que me ofrecieron la oportunidad que buscaba y me ayudaron a llevarla a término. Aquí quiero destacar la colaboración y dedicación de Antonio Soria para la consecución de esta tesis.

También quiero agradecer a los doctores del grupo ISE, Antonio Acosta, Ulpiano, María, Mercedes, Néstor, Celia, Sergio, Carol, Fernando, Luismi y María I. su apoyo, colaboración y buenos momentos compartidos dentro y fuera de la universidad. Agradecer a todos los miembros del grupo de Mecánica de Fluidos su generosidad y buena disposición para resolver cualquier cuestión. Agradecer a Cristina por su ayuda en todas las gestiones, relacionadas o no con la tesis.

Por supuesto, también quiero mencionar al resto de compañeros doctorandos con los que he compartido muy buenos momentos. En primer lugar a mis compañeras Reyes y a Lucía, por el buen ambiente y momentos compartidos en el 'despacho que mola'. A Alberto, Dani S. y Edu, compañeros de fatigas en múltiples deportes. A Dani M., Luis, Miguel, Elena, Paula, Matías, Ana y Wil, aunque ya terminó hace tiempo, por su simpatía, sonrisas y ganas de diversión en todo momento. A Mariano, Carlos, Pablo S., Alberto Q. y Dani M. por los buenos momentos que hemos disfrutado durante las comidas y cafés. Y por supuesto, agradecer todas las fatigas y risas a Javi S. y Juan, con mención especial para mi álter ego. Gracias a los técnicos de laboratorio del departamento, por su disposición en todo momento en lo referente a la instalación experimental.

Dicen que quien tiene un amigo, tiene un tesoro, así que, ¿cómo olvidarme de todos esos gambiteros que pueblan el mundo? A todos vosotros que os tengo muy presente a pesar de la distancia. En orden casi cronológico, a mi hermano Javier (o Javier^N), el primero y mejor, juntos hemos desarrollado un altísimo grado de tontería. Agradecer a los de Salamanca (Abel, Juan y Almudena) todos sus desvaríos y genialidades; a los compañeros y amigos de las carreras de

Albacete y Madrid los ratos y risas, destacando a Juan Carlos, Miguel, Vicente y Luis por ser auténticos como la vida misma; y a los nuevos amigos de Madrid y del Camino. Evidentemente, no se me pueden olvidar los más especiales: tooodos los de Albacete, Elías (tú el primero que eres un bacín), Gema (que no sé ya en qué grupo ponerte), Almu, Fran, Tere, Toni, Javi, Laura, Jose, Sandra, Sergio y Pilar, que llevan aguantándome muchos años, y que, sin pedir nada a cambio, han hecho posible que termine esta tesis.

Y, como los últimos son siempre los primeros, agradezco a toda mi familia su incondicional apoyo y cariño. Sin vuestro ejemplo de humildad y esfuerzo no lo habría conseguido, ya que 'si he logrado ver más lejos, ha sido porque he subido a vuestros hombros de gigantes'.

Acknowledgments

During the last few years, the ISE research group has welcomed the pleasant visits of several researchers during different conferences related to the main research lines of our group. I would like to thank all of them for their visits, which have been a great source of ideas for this thesis: Bo Leckner, *Chalmers University of Technology*, Naoko Ellis, *University of British Columbia*, David Pallarès, *Chalmers University of Technology* and Allan Hayhurst, *University of Cambridge*.

I would like to thank very much to professors Ruud van Ommen and Robert Mudde, from the to Product and Process Engineering (PPE) and Transport Phenomena (TP) groups respectively, of the Technical University of Delft (The Netherlands), for hosting me during my research stay in 2013. I would like to thank the personnel of both groups for its useful help and support, specially Mojgan, Yogesh, David, Aris, Fabio, Andrea and Lilian. Also, I would like to thank my Spanish family in Delft, specially Sito, for their laughs and support.

Resumen

Los lechos fluidizados se emplean en la industria debido a sus buenas propiedades de transferencia de calor y de masa. Esto hace que tengan un amplio rango de aplicaciones que comprende desde procesos de gasificación o combustión de biomasa hasta procesos de recubrimiento de partículas y procesos de secado. Todas estas aplicaciones tienen en común la importancia que tiene la zona adyacente al distribuidor sobre la dinámica del proceso. De esta forma, un mal mezclado entre las fases densa y gaseosa en esta zona induce la aparición de problemas como la segregación de partículas, la formación de zonas muertas en donde el mezclado es prácticamente inexistente, la mala distribución de temperaturas en el interior del lecho y la formación de canales o caminos preferentes a través de los cuales circula el gas de fluidización. Desde el punto de vista operativo, estos fenómenos suelen producir la parada o defluidización del lecho, con sus consecuentes costes económicos. Por ello, resulta necesario estudiar la dinámica del proceso para que, en caso de que aparezcan estos problemas operacionales, se pueda influir sobre la dinámica del lecho.

La presente tesis doctoral desarrolla los métodos para estudiar y controlar la dinámica de un lecho que dispone de un distribuidor rotatorio como herramienta para modificar el comportamiento del lecho. Estas herramientas fueron desarrolladas utilizando una instalación de escala laboratorio equipada con un motor eléctrico acoplado al plato distribuidor, lo que permite su giro en el plano horizontal.

Las condiciones experimentales de mal mezclado y baja calidad en la fluidización reportadas en la literatura fueron estudiadas para comprobar el efecto del giro del distribuidor sobre la dinámica del lecho. Estas condiciones de mala fluidización se consiguieron mediante la inyección de agua a la superficie del lecho cuando éste operaba en régimen de burbujeo. La inyección de líquido produjo la formación de aglomerados que, debido a su mayor densidad, tendieron a posarse sobre el distribuidor. De esta forma, aparecieron zonas muertas y canales produciendo la defluidización del lecho. La descripción de estos procesos de defluidización y posterior recuperación del régimen de burbujeo se realizó empleando las medidas de las fluctuaciones de presión en el gas fluidizante. Estas señales fueron estudiadas utilizando métodos de análisis en el dominio del tiempo, con la desviación típica, y en el dominio de la frecuencia mediante el

espectro de potencias de Welch, el espectro transitorio y la energía contenida en las regiones frecuenciales. Para este estado de defluidización, se demostró que el giro del distribuidor mejora el proceso de recuperación comparado con las condiciones convencionales de distribuidor estático. Los resultados demostraron que el giro rompe los aglomerados y canales que aparecen sobre el distribuidor, imponiendo una estructura sobre la dinámica de la fluidización. Esta mejora en el proceso de re-fluidización se comprobó para lechos profundos y poco profundos. Respecto a los métodos de análisis de la señal, se relacionaron los procesos de formación de canales con la codificación de la energía de la señal a altas frecuencias.

El método inicialmente empleado para estimar la energía contenida en las regiones frecuenciales utilizaba la inspección visual del espectro de potencias para dividir el dominio de frecuencias. Este método para dividir el dominio frecuencial está influenciado por el observador, lo que puede dar lugar a errores significativos especialmente si la señal de presión tiene ruido. Por ello, se propuso una metodología para dividir sistemáticamente el dominio de frecuencias. El procedimiento aproxima la distribución acumulada de energía del espectro de potencias a una distribución estadística. Después, el test de Kolmogorov-Smirnov determina cuáles son las zonas de coincidencia entre la distribución estadística y la distribución de energía acumulada de la señal. Usualmente la zona de coincidencia está centrada en el incremento de energía, mientras que las colas de la distribución quedan fuera de la aproximación. Para las condiciones experimentales consideradas, la distribución t-Student fue empleada para aproximar la distribución acumulada de energía. La fiabilidad del método fue demostrada utilizando sensores de presión de alta y baja calidad, y modificando la velocidad del gas y la relación de aspecto del lecho. Ensayos de defluidización inducida por la inyección de agua a la superficie del lecho fueron realizados para ilustrar el empleo de la energía contenida en las regiones frecuenciales como una herramienta de monitorización. Los resultados permitieron comparar el método de división visual con el método basado en la aproximación estadística. Se observó que la energía contenida en las regiones frecuenciales obtenidas de forma visual no era capaz de detectar cambios en la relación de aspecto o el inicio del giro del distribuidor. Por contra, la energía de las regiones frecuenciales de la t-Student varía en función de las condiciones experimentales, lo que facilita la identificación de procesos como la formación de canales o la defluidización del lecho.

Para establecer si la dinámica del lecho ha cambiado es necesario definir una

zona de control en la que se mantengan las condiciones de operación deseadas. Por ello, se propuso una metodología para la monitorización continua del estado del lecho. Esta metodología está basada en la teoría de control estadístico de procesos y fue aplicada a distintas variables obtenidas tras el análisis de la señal de presión para comprobar la aplicabilidad del método. Se obtuvo el tamaño de ventana de cada variable y la distribución estadística utilizada para calcular los límites de control. La buena sensibilidad mostrada por este esquema durante la monitorización de un proceso de secado estimula su empleo para cualquier tipo de variable.

Por último, una vez se demostró que el giro del distribuidor tiene un efecto beneficioso en lechos con problemas de fluidización, y que se desarrollaron las herramientas de análisis y control necesarias, se estudió una aplicación práctica como es el secado de pastas, que están formadas por arena y agua. Siguiendo el procedimiento experimental descrito en la literatura, los experimentos consistieron en dejar caer la pasta a un lecho trabajando en régimen de burbujeo y formado por partículas secas de arena. De esta forma, la pasta tiende a romperse y dispersarse homogéneamente dentro del lecho, comenzando así el proceso de secado. Este proceso fue caracterizado utilizando medidas de temperatura y humedad del aire a la entrada y salida del lecho, junto con la medición de las señales de presión. El análisis multi-resolución de las señales de presión relacionó los periodos del secado con la dinámica del lecho. Por otro lado, el empleo del esquema SPC permitió definir el tiempo necesario para recuperar las condiciones de control tras el secado de la pasta. Este parámetro característico del proceso demostró que tanto el fin del secado como la recuperación de la dinámica ocurren simultáneamente en lechos poco profundos, mientras que para lechos profundos se recupera la dinámica antes de que finalice por completo el secado operando con el distribuidor estático. Por contra, el giro del distribuidor disminuye tanto el tiempo de secado como el necesario para la recuperación de la dinámica, igualando además el comportamiento de lechos profundos y poco profundos. Por tanto, se puede concluir que el giro del distribuidor mejora el proceso de secado.

Abstract

Fluidized beds are used for a wide variety of processes due to its high rates of heat and mass transfer. Due to that, fluidized beds are used for a variety of applications ranging from the gasification or combustion of biomass, to coating and drying processes. All these industrial applications show the main influence of the zone close to the distributor on the bed dynamics. In this way, a non-homogeneous mixing in this zone between dense and gas phases leads to fluidization problems such as segregation of particles, formation of dead zones, heterogeneous distribution of temperatures inside the bed and appearance of channels or preference paths for the flowing fluidization gas. These phenomena usually cause the process stop or the bed defluidization, which increase operational costs. Therefore, it is necessary to study the bed dynamics in order to be able to detect these fluidization problems, and modify somehow the hydrodynamic structure of the bed.

This PhD thesis develops the methods needed to study and control the behaviour of a bed equipped with a rotating distributor as a tool to change the bed dynamics. These approaches were developed using a lab-scale facility with an electrical motor coupled to the distributor, capable of imposing its rotation in the horizontal plane.

The experimental conditions of poor fluidization quality typically shown in industrial applications are studied to assess the potential use of the rotating distributor on the bed dynamics. Punctual injections of water over the bed surface were carried out to replicate the experimental conditions reported in literature. This water injection improved the development of dead zones over the distributor plate, facilitating the bed defluidization. The defluidization and re-fluidization processes were characterized using pressure fluctuation signals recorded during the experiments. Methods of analysis in the time domain, standard deviation, and in the frequency domain, Welch′s power spectrum, transient spectrogram and wide band energy, were employed to describe the defluidization and re-fluidization processes. By using the rotating distributor, the fluidization quality was improved due to its breakage effect on the agglomerates and channels settled over of the distributor. Such an improvement was shown for both shallow and deep beds. Therefore, the distributor rotation introduces a dynamic structure into the gas-solid fluidized bed. Moreover, con-

cerning the methods of signal analysis, the channels appearance is related to an energy increase of the high frequencies within the pressure signal.

The approach initially employed for the computation of the wide band energy was based on the visual division of the frequency domain. However, the results obtained using this method are influenced by the observer, specially if the quality of the measured signal is low. Therefore, an unbiased methodology is proposed for the systematic division of the frequency domain. The approach is based on the statistic distribution fitting of the power spectrum cumulative energy. Hence, the Kolmogorov-Smirnov test is used to compare the cumulative energy with the statistic distribution. The differences that appear at the distribution tails when comparing the cumulative energy with the statistic distribution discriminate the cut-off frequencies that separate the three frequency regions of the frequency domain. For the operation conditions considered, the Student′s t-distribution was used to fit the cumulative energy distribution. The reliability of the method to divide the frequency domain was shown for different fluidization velocities, changing the bed aspect ratio and using different pressure probes. Water-induced defluidization tests were conducted to illustrate the use of the wide band energy as a monitoring tool. Both visual and statistical approaches were compared. The results showed that the energy contained within the frequency regions obtained by the visual method is not able to detect changes in the bed aspect ratio or the beginning of the rotating distributor. On the other hand, the sensitivity exhibited by the proposed frequency division approach, for the range of fluidization conditions tested, encouraged the use of the energy contained in these regions as a diagnostic tool in fluidized bed processes.

In order to determine whether or not the bed behavior has changed, the implementation of a monitoring system capable of ensuring the process operation at a certain level of efficiency is required. Therefore, an on-line monitoring methodology is proposed. This approach is based on the Statistical Process Control theory and it is applied to different variables, which were obtained through the analysis of the measured pressure signals. The statistical treatment of the variables allowed the definition of the control state through the study of the sample size and its underlying distribution. The good results showed by the different control variables encouraged the use of the proposed control scheme to any monitoring variable.

Finally, once the high influence of the rotating distributor on the bed dynamics was proved, and the analysis and monitoring tools needed were developed, a

practical application is presented. The paste drying process with inert particles as a support medium is analyzed recording humidity and temperature measurements together with pressure fluctuation signals. The experiments consisted on the paste-drop, which was composed of a mixture of silica sand and water, to a bed of dry silica sand particles. In this way, the paste tends to be homogeneously dispersed throughout the bed, beginning the drying process. The multi-resolution approach of the pressure fluctuation signals showed the effect of the paste-drop, relating the drying periods to the bed dynamics. To compare the results obtained from the humidity and temperature measurements with those of the pressure signals, a Statistical Process Control approach is applied to define the time needed to recover the bed dynamic. For the static distributor, similar values of the drying and recuperation times are obtained for shallow beds, while for deeper beds more time is needed to complete the drying than to recover the fluidization quality. For the rotating distributor, lower drying and dynamic times are needed for shallow and deep beds.

Contents

List of Figures

List of Tables

CHAPTER
ONE

Introduction

Contents

In this chapter, a brief introduction to gas-solid fluidized beds is presented, focusing on the agglomeration problems typically shown in many industrial applications, such as paste drying. These phenomena affect the zone close to the distributor, reducing the fluidization quality and leading to bed defluidization. Measurements techniques to evaluate the fluidization quality, different methods of signal analysis and strategies to fight against these problems are also presented. In this way, the use of a rotating-distributor fluidized bed arises as a possible solution to overcome the bed defluidization.

1.1 Fluidization phenomena

Fluidization is the process by which a granular material is supported by a vertical flow of fluid, changing the solid behavior of the particles to a fluid-like state. The fluid employed to fluidize the solid particles may be a liquid or a gas. Depending on the properties of the fluid and the particles, the bed exhibits different regimes.

Initially, for low fluid velocities the fluid percolates through the void spaces between the solid particles of the bed, in what is called a fixed bed. When the upward fluid velocity is increased, the weight of the particles is counterbalanced by the drag force caused by the fluid. At this stage, the bed is supported by

the fluid, showing a fluid-like behavior, and the bed is said to be incipiently fluidized or at minimum fluidization. For gas-solid fluidized beds, gas velocities higher than the minimum fluidization velocity usually results in the appearance of large instabilities and bubbles inside the bed, which causes a vigorous motion of solids typically shown in bubbling fluidized beds. Turbulent motion of solids and pneumatic transport of particles are observed when the gas velocity is further increased.

The main advantages of gas-solid fluidized bed technology are a large contact area between solids and gas, high thermal inertia of solids, good degree of solids mixing, and high mass and heat transfer coefficients. Due to that, fluidized beds are used for a variety of applications in a wide range of scales, from small chemical reactors to large coal combustors. However, fluidized beds also present disadvantages such as complex hydrodynamics, bypass of gas through bubbles, erosion of pipes inside the bed reactor, high rates of solids entrainment, and agglomeration of particles. Even though particle aggregation is desired in some processes such as granulation or coating, the formation of large agglomerates often produces serious problems leading to channeling and defluidization of the bed. The onset of agglomeration differs for different processes, but the sticky agglomerates usually tend to segregate and settle over the distributor, changing the bed hydrodynamics and reducing the advantages of fluidized beds.

Geldart (1973) classified the behavior of solids fluidized by gases into four groups characterized by the solids size and density. Molerus (1982) explained the four groups based on the inter-particle forces that appear between particles. For fine powders, these forces are mainly van der Waals and electrostatic forces. Other sources of inter-particle forces not considered by Geldart can be caused by the presence of a liquid phase or adhesive layer on the particle surface. When this adhesive phase appears, the sticky particles grow towards larger agglomerates due to the formation of permanent bonds upon collisions. If the cohesive forces are of the same order of magnitude as the gravitational force of the particle, the gas flow pattern may be changed and fluidization can be deteriorated or even prevented.

The onset of agglomeration depends on each process, but it is often related to the presence of a liquid phase that acts as a glue between particles (Bartels *et al.*, 2008). For high temperature applications, such as coal gasification, combustion or gasification of biomass, or pyrolysis of plastic waste, the agglomeration process is caused by the generation of ash (Ergudenler & Ghaly, 1993; Lin *et al.*, 2003; Yan *et al.*, 2003; Aguado *et al.*, 2005). In these processes, ash

is deposited on the surface of the bed material and, since it is usually formed by low melting point materials, the bed particles grow in size via sinterization (Mettanant *et al.*, 2009). As a consequence, the mixing inside the bed is reduced, producing an uneven distribution of temperature in the bed. Due to that, segregation will appear, producing the defluidization of the bed.

Other applications that usually present unwanted agglomeration problems during normal operation are related to the drying of suspensions, sludges, or paste-like materials. In these processes, the paste is usually dropped into a bed formed by inert particles through a nozzle or a dropping device from the bed surface (Lee & Kim, 1993; Adamiec, 2002; Freire *et al.*, 2012). The inert particles provide an auxiliary phase that sustains the fluidization. Due to the intensive motion of these particles within the bed, the fluid is homogeneously dispersed and rapidly dried. However, the coating layer, which is gradually dried, is an adhesive phase that tends to widen the particle size distribution, resulting in the segregation to the bottom of the bed (Kudra *et al.*, 2002). At this point, liquid bridges may cause the appearance of channels in the bed, reducing the efficiency of the drying process (Tatemoto & Miyazawa, 2011).

Therefore, independently of the application, the formation of unwanted agglomerates leads to a poor mixing within the bed, modifying the normal bubble pattern. This causes bed segregation, which is reflected in the appearance of dead zones over the distributor plate that facilitates the bed defluidization. Furthermore, channels or preference paths are typically formed throughout the bed near the cohesive regions. In this way, the use of a rotating distributor appears as a solution to overcome these problems. Thus, it is mandatory to detect the onset of the agglomeration in order to be able to counteract its detrimental effects on the fluidization quality.

1.2 Measurement techniques

Some industrial applications of fluidized beds, such as granulation, coating, drying, combustion or gasification, involve the risk of agglomerates formation. The rapid recognition of this phenomenon permits the prevention of its propagation to partial or total defluidization of the bed. For a proper description of the dynamics based on experiments, time-series data should be measured and analyzed. Many measurement techniques has been developed to increase the knowledge on the dynamic phenomena occurring in the bed (Werther, 1999). A wide variety of experimental techniques have been employed by different au-

thors, such as Electrical Capacitance and X-ray Computed Tomography used for non-invasive visualization of the internal flow (Xie *et al.*, 1992; Heindel, 2011), laser based measurements (Briongos & Soler, 2003), techniques based on optic fiber probes (Amos *et al.*, 1996) and measurements of acoustic emissions created by the process itself (Herrera *et al.*, 2002; de Martin *et al.*, 2010). In spite of this wide amount of measurements that can be used to describe the fluidization state, the most commonly used technique is the pressure fluctuations measurements (van der Schaaf *et al.*, 1998; Johnsson *et al.*, 2000; van Ommen *et al.*, 2011). The main advantage of using pressure is that it is easily measured, even under harsh, industrial conditions. Furthermore, the pressure based measurement system is low-cost and the measurements are mainly related to bubble formation and motion inside the bed. For this reason, this thesis characterizes the bed state by local pressure fluctuations measurements.

A large variety of methods for the analysis of pressure time-series data is available in the literature (Johnsson *et al.*, 2000; van Ommen *et al.*, 2011). These methods can be grouped into three categories: (i) time domain methods, (ii) frequency domain methods, and (iii) state space methods. Linear methods of time and frequency domain have been used in this thesis to obtain information about the hydrodynamic state of the fluidized bed. These methods were chosen instead of state space analysis since, in the case of comparable performances, linear methods are typically preferred over non-linear methods because of their simplicity and generally lower computational demand (Bartels *et al.*, 2009).

Furthermore, in spite of the high capability shown by the monitoring methods to reflect the bed state, a certain amount of inherent or natural variability will always exist in the process. Dealing with this variability to design an on-line monitoring strategy is still a difficult task because of the complex processes that appear in a fluidized bed. In this sense, some efforts have been made through the application of different control strategies, such as PI or PID controllers, fuzzy logic, neural networks, and models based on experimental design techniques (Chong *et al.*, 1987; Croxford & Gilbertson, 2006; Barletta *et al.*, 2008; Silva *et al.*, 2011). Similarly, other works deal with the design of an on-line monitoring strategy for the description and identification of problems in fluidized bed processes analyzing pressure signals in the time domain (Johnsson *et al.*, 2000; Briens & Briens, 2002), frequency domain (Kage *et al.*, 2000) and state space domain (Schouten & van den Bleek, 1998; van Ommen *et al.*, 2000). These works are focused on the development and analysis of a specific monitoring tool, showing a high sensitivity to detect problems in the fluidization

behavior.

1.3 Fight against defluidization phenomena

Many strategies have been reviewed by Bartels *et al.* (2008) regarding the fight against defluidization phenomena, including operational actions, changes in the fuel supply rate and use of alternative bed materials (Nordin *et al.*, 1996; Lin *et al.*, 2003; Silvennoinen, 2003). Concerning the operational actions, the studies can be described as attempts to modify the conventional gas-solid fluidized bed dynamics by imposing a structure to the reactor environment.

Structuring a fluidized bed helps to overcome some of the problems and typical disadvantages of conventional fluidized beds. The advantages of structuring include the limitation of the bubble size, reduction of erosion and improvement of mass transfer. Also, structuring helps to fluidize powders that are difficult to fluidize because of a high moisture content or a reduced particle size. Thus, many investigators have proposed modifications of conventional fluidized bed devices to solve specific problems of industrial processes, such as maldistribution of solids, channeling, elutriation and defluidization. On the other hand, it should be noted that not all modified fluidized beds are necessarily better than the conventional fluidized beds (Figure 1.1-a), since they typically increase the manufacture and operational costs.

The structuring of gas-solid fluidized beds can be carried out by modifying the gas supply or by interfering in the particle phase. In both cases, either the dynamics can be changed or the geometry can be altered, yielding four different approaches (van Ommen *et al.*, 2007). The following classification describes the main characteristics of each group:

- Manipulation of the gas supply.

Typically, fluidized bed reactors operate at a constant gas supply, changing the gas velocity only after long periods of time (from minutes to hours) as a function of the process performance. However, the modification of the gas supply over short times (seconds) could influence the hydrodynamics of the bed (van Ommen *et al.*, 2007). The best choice is to impose a continuous periodic variation on the gas flow rate, which is carried out in vibrated and pulsed fluidized beds.

Vibrated fluidized beds (Figure 1.1-b) are often employed for spray drying systems to produce instant agglomerated powder or act as a powder conditioning plant for special coating operations (Daud, 2008). Vibration is typically

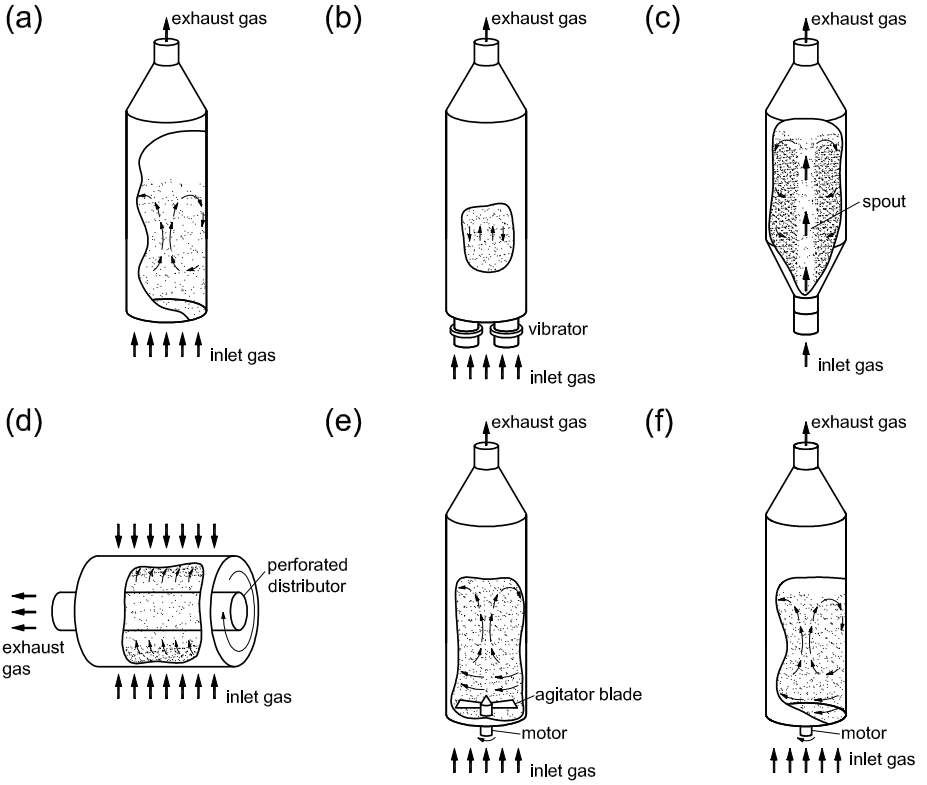

Figure 1.1: Common fluidized bed types: (a) conventional FB, (b) vibrated FB, (c) spouted FB, (d) centrifugal FB, (e) agitated FB, (f) rotating distributor FB.

accomplished by vibrating the gas-distributor plate, where all the energy is transmitted to the particles via the moving bottom plate. Vibration enables the drying particles to fluidize smoothly, improving the heat and mass transfer coefficients (Meili *et al.*, 2010). Thus, a vibrating fluidized bed is useful for drying materials that are fine, fragile, poorly fluidizable, have a broad particle distribution and require relatively low fluidization velocities to prevent attrition. Vibration is especially employed for fluidizing Geldart′s C particles. The bed is usually shallow since the effect of vibration imposed on the gas distributor decays with distance from the grid (Mujumdar, 2006).

In pulsed fluidized beds (Figure 1.1-c), the patterns imposed in the fluidizing gas are propagated upwards via the rising gas flow, obtaining different patterns from those observed in vibrated granular layers. By pulsating the gas flow, either the whole bed or part of the bed is subjected to a variable fluidizing gas velocity. This contributes to effective energy costs saving and enhanced

the drying performance without affecting the fluidization quality and process performance. In this way, this technology has been found to show improvements in the drying rate of light particles that are prone to agglomerate, such as porous pharmaceutical granules and paper sludge (Jose *et al.*, 1994; Kudra *et al.*, 2002; Akhavan *et al.*, 2009).

- Manipulation of the particle dynamics.

The particle dynamics can be manipulated by changing the forces acting on the particles. In a fluidized bed, several forces act on a particle: buoyancy (usually neglected in gas-solid fluidization), drag, interparticle forces and gravity. Gas velocity variations change the drag force, modifying the complete hydrodynamics of the bed. A different option is to act over the interparticle forces by applying electric or magnetic fields. In this way, the interparticle forces can be manipulated without changing the particle properties (Hristov, 2002; van Willigen *et al.*, 2004). A high power consumption is required for the application of the magnetic field, and therefore, it is not viable for large-scale applications. In contrast, smaller bubble sizes were obtained when an electric field is employed over the whole bed (van Ommen *et al.*, 2007).

Gravitational forces can be imposed by rotating the fluidization chamber in a centrifugal fluidized bed (Figure 1.1-d). The centrifugal fluidized bed balances the centrifugal force generated by the chamber rotation with the particle drag force caused by the radial fluidization gas (Figure 1.1-d). This force is generated by rapidly rotating the fluidization chamber to form an annular bed of particles that is radially fluidized by gas injected through the porous or sintered outer wall and removed via a central chimney (Daud, 2008). The centrifugal force improves heat and mass transfer coefficients and prevents agglomeration and entrainment of particles (Nakamura & Watano, 2008; Lim *et al.*, 2010). This design has been recently employed to fluidize nanoparticles (Quevedo *et al.*, 2006).

- Manipulation of the distributed particle properties.

As stated above, the particle properties have a strong influence on their fluidization behavior. In this way, varying the properties of the distributed particles, such as size, density and shape can modify the fluidization behavior. Recent works showed that the addition of fines (particles with a diameter smaller than 45 μm) improves the fluidization quality and leads to higher mass transfer (van Ommen *et al.*, 2007; Brouwer *et al.*, 2012). However, further research is needed for this structuring method to be implemented in large scale reactors.

- Manipulation of the geometry of the gas supply.

Other authors have tried to overcome the difficulties in mixing between phases and between solids in the bed by modifying the geometry of gas supply. Baffles or other internals can be installed to improve the solid mixing and limit the bubble size (Figure 1.1-e). By agitation, a homogeneous fluidized bed is formed, preventing the formation of channels or large bubbles. These beds are useful for drying pastes or cakes consisting of fine particles since the disintegration and dispersion of the pasty feed is improved (Watano *et al.*, 1998; Reyes *et al.*, 2001; Adamiec, 2002).

The gas supply can be also homogeneously introduced over the height of the bed, using a fractal design by introducing membrane tubes within the bed (Adris & Grace, 1997; van Willigen *et al.*, 2005). The fluidization quality can also be improved by creating a swirling pattern introducing the gas horizontally or using special distributor designs, i.e. changing the orifice inclination in the gas distributor (Zhao *et al.*, 2004; Liu *et al.*, 2014) or using a rotating distributor.

Concerning the rotating distributor employed in this thesis, previous studies of Sobrino *et al.* (2008, 2009) and Soria-Verdugo *et al.* (2011) have characterized the dynamic behavior of this system. This device consists of an electric motor coupled to the distributor plate, allowing the rotation of the distributor in the horizontal plane (Figure 1.1-f). In this way, the bottom of the bed is influenced by the swirl movement imposed with the rotation. The rotating velocity varies from 0 (static distributor) to 100 rpm. A detailed revision of the influence of the rotating distributor on the fluidization dynamics can be found in chapters 2 to 5. The main effects caused by the rotating distributor are:

- The minimum fluidization velocity decreases as the rotational speed of the distributor increases, facilitating the fluidization.
- The rotation introduces a radial component to the predominant axial component of the flow present in conventional fluidized beds.
- Similar fluidization quality (e.g. similar bubbles size and frequency) is obtained for different rotational speeds keeping the same gas velocity.
- The influence of the distributor motion on the bed dynamics reaches up to 11 cm above the distributor, permitting its use in very shallow beds.
- Smaller bubbles were found for the rotating distributor than for the static distributor for similar gas velocities.

- The rotation of the distributor breaks the layout of gas jets and stagnant zones between the holes of the distributor, improving the radial and axial mixing at the bottom of the bed.

1.4 Motivation of the thesis

As stated above, a non-homogeneous mixing in the zone close to the distributor leads to problems in the fluidization quality. Agglomeration phenomena usually cause such problems, which may produce the complete defluidization of the bed. Therefore, it is necessary to study the bed dynamics to detect these processes, and once the bed state is changing towards defluidization, modify somehow the hydrodynamic structure of the bed. In this way, due to the fluidization improvement produced by the distributor rotation, its potential use for counteracting agglomeration and defluidization phenomena is studied. Therefore, this PhD thesis develops the methods needed to study and control the behavior of a bed that is equipped with a rotating distributor as a tool to change the bed dynamics. The main objectives of the thesis are summarized below:

- Demonstration of the applicability of the rotating distributor for counteracting agglomeration and defluidization phenomena.
- Development of an analysis method of the pressure fluctuations to discriminate the fluidization quality.
- Design of a control scheme capable of monitoring continuously the fluidization state of the process.
- Application of the rotating distributor to a paste drying process.

1.5 Structure of this thesis

This PhD thesis has been organized in six chapters. Chapters 2 to 5 have been written as independent articles with their own abstract, introduction, notation and bibliography.

In Chapter 2 the results previously reported by Sobrino *et al.* (2008, 2009) and Soria-Verdugo *et al.* (2011) are employed to assess the use of the rotating distributor as a counteracting method to defluidization phenomena. Special attention is focused on the analysis methods of the pressure fluctuations signals.

In Chapter 3 an unbiased methodology is proposed for the frequency domain division, in order to systematically study the energy contained within the regions of the frequency domain (wide band energy). This chapter is based on the findings shown in Chapter 2.

In Chapter 4 a control scheme based on the Statistical Process Control theory is proposed for the continuous control of fluidized bed processes. The control scheme is developed for analysis methods of the pressure signals in both the time and frequency domains. Paste drying experiments with sand particles as inert medium were carried out in order to analyze the performance of the control scheme.

In Chapter 5 the drying characteristics of the rotating distributor are studied for paste drying tests. The performance of the rotating distributor is compared to the static distributor case by means of a classical drying analysis, and also, employing the analysis tools of the pressure signals developed in Chapters 3 and 4.

Finally, Chapter 6 summarizes the conclusions of the thesis.

References

Adamiec, J. 2002 Drying of waste sludges in a fluidized bed dryer with a mixer. *Drying Technology* 20 (4-5), 839–853.

Adris, A. E. M. & Grace, J. R. 1997 Characteristics of fluidized-bed membrane reactors: Scale-up and practical issues. *Industrial & Engineering Chemistry Research* 36 (11), 4549–4556.

Aguado, R., Prieto, R., Jose, M. J. San, Alvarez, S., Olazar, M. & Bilbao, J. 2005 Defluidization modelling of pyrolysis of plastics in a conical spouted bed reactor. *Chemical Engineering and Processing* 44 (2), 231–235.

Akhavan, A., van Ommen, J. R., Nijenhuis, J., Wang, X. S., Coppens, M.O. & Rhodes, M. J. 2009 Improved drying in a pulsation-assisted fluidized bed. *Industrial & Engineering Chemistry Research* 48 (1), 302–309.

Amos, G., Rhodes, M. J. & Benkreira, H. 1996 Calculation of optic fibres calibration curves for the measurement of solids volume fractions in multiphase flows. *Powder Technology* 88 (2), 107–121.

Barletta, M., Gisario, A., Guarino, S. & Tagliaferri, V. 2008 Fluidized bed coating of metal substrates by using high performance thermoplas-

tic powders: Statistical approach and neural network modelling. *Engineering Applications of Artificial Intelligence* 21 (8), 1130–1143.

Bartels, M., Lin, W., Nijenhuis, J., Kapteijn, F. & van Ommen, J. R. 2008 Agglomeration in fluidized beds at high temperatures: Mechanisms, detection and prevention. *Progress in Energy and Combustion Science* 34 (5), 633–666.

Bartels, M., Vermeer, B., Nijenhuis, J. & Kapteijn, F. 2009 Methodology for the screening of signal analysis methods for selective detection of hydrodynamic changes in fluidized bed systems. *Industrial & Engineering Chemistry Research* 48 (6), 3158–3166.

Briens, L. A. & Briens, C. L. 2002 Cycle detection and characterization in chemical engineering. *AIChE Journal* 48 (5), 970–980.

Briongos, J. Villa & Soler, J. G. 2003 Free top fluidized bed surface fluctuations as a source of hydrodynamic data. *Powder Technology* 134 (1-2), 133–144.

Brouwer, G. C., Wagner, E. C., van Ommen, J. R. & Mudde, R. F. 2012 Effects of pressure and fines content on bubble diameter in a fluidized bed studied using fast x-ray tomography. *Chemical Engineering Journal* 207-208 (0), 711–717.

Chong, Y.O., Odea, D.P., White, E.T., Lee, P.L. & Leung, L.S. 1987 Control of the quality of fluidization in a tall bed using the variance of pressure-fluctuations. *Powder Technology* 53 (3), 237–246.

Croxford, A. J. & Gilbertson, M. A. 2006 Control of the state of a bubbling fluidised bed. *Chemical Engineering Science* 61 (19), 6302–6315.

Daud, W. R. W. 2008 Fluidized bed dryers - recent advances. *Advanced Powder Technology* 19 (5), 403–418.

Ergudenler, A. & Ghaly, A. E. 1993 Agglomeration of silica sand in a fluidized-bed gasifier operating on wheat straw. *Biomass & Bioenergy* 4 (2), 135–147.

Freire, J. T., Ferreira, M. C., Freire, F. B. & Nascimento, B. S. 2012 A review on paste drying with inert particles as support medium. *Drying Technology* 30 (4), 330–341.

Geldart, D. 1973 Types of gas fluidization. *Powder Technology* 7 (5), 285–292.

Heindel, T. J. 2011 A review of x-ray flow visualization with applications to multiphase flows. *Journal of Fluids Engineering* 133 (7), 074001–074001.

Herrera, C. A., Levy, E. K. & Ochs, J. 2002 Characteristics of acoustic standing waves in fluidized beds. *AIChE Journal* 48 (3), 503–513.

Hristov, J. 2002 Magnetic field assisted fluidization a unified approach - part 1. fundamentals and relevant hydrodynamics of gas-fluidized beds (batch solids mode). *Reviews in Chemical Engineering* 18 (4-5), 295–509.

Johnsson, F., Zijerveld, R. C., Schouten, J. C., van den Bleek, C. M. & Leckner, B. 2000 Characterization of fluidization regimes by time-series analysis of pressure fluctuations. *International Journal of Multiphase Flow* 26 (4), 663–715.

Jose, M. J. San, Olazar, M., Alvarez, S., Izquierdo, M. A. & Bilbao, J. 1994 Segregation in conical spouted beds with binary and ternary mixtures of equidensity spherical particles. *Industrial & Engineering Chemistry Research* 33 (7), 1838–1844.

Kage, H., Agari, M., Ogura, H. & Matsuno, Y. 2000 Frequency analysis of pressure fluctuation in fluidized bed plenum and its confidence limit for detection of various modes of fluidization. *Advanced Powder Technology* 11 (4), 459–475.

Kudra, T., Gawrzynski, Z., Glaser, R., Stanislawski, J. & Poirier, M. 2002 Drying of pulp and paper sludge in a pulsed fluid bed dryer. *Drying Technology* 20 (4-5), 917–933.

Lee, D. H. & Kim, S. D. 1993 Drying characteristics of starch in an inert medium fluidized bed. *Chemical Engineering and Technology* 16 (4), 263–269.

Lim, H. O., Seo, M. J. & Kang, Y. 2010 Drying of thermally-weak organic powder in a centrifugal fluidized bed. *Advanced Powder Technology* 21 (2), 131–135.

Lin, W. G., Dam-Johansen, K. & Frandsen, F. 2003 Agglomeration in bio-fuel fired fluidized bed combustors. *Chemical Engineering Journal* 96 (1-3), 171–185.

Liu, Y., Peng, J., Kansha, Y., Ishizuka, M., Tsutsumi, A., Jia, D., Bi, X. T., Lim, C. J. & Sokhansanj, S. 2014 Novel fluidized bed dryer for biomass drying. *Fuel Processing Technology* 122, 170–175.

de Martin, L., Briongos, J. Villa, Aragon, J. M. & Palancar, M. C. 2010 Can low frequency accelerometry replace pressure measurements for monitoring gas-solid fluidized beds? *Chemical Engineering Science* 65 (13), 4055–4064.

Meili, L., Daleffe, R. V., Ferreira, M. C. & Freire, J. T. 2010 Analysis of the influence of dimensionless vibration number on the drying of pastes in vibrofluidized beds. *Drying Technology* 28 (3), 402–411.

Mettanant, V., Basu, P. & Butler, J. 2009 Agglomeration of biomass fired fluidized bed gasifier and combustor. *Canadian Journal of Chemical Engineering* 87 (5), 656–684.

Molerus, O. 1982 Interpretation of geldart type-a, type-b, type-c and type-d powders by taking into account interparticle cohesion forces. *Powder Technology* 33 (1), 81–87.

Mujumdar, A. S. 2006 *Handbook of Industrial Drying*. Taylor & Francis.

Nakamura, H. & Watano, S. 2008 Fundamental particle fluidization behavior and handling of nano-particles in a rotating fluidized bed. *Powder Technology* 183 (3), 324–332.

Nordin, A., Ohman, M., Skrifvars, B. J. & Hupa, M. 1996 Agglomeration and defluidization in fbc of biomass fuels- mechanism and measures for prevention. In *Applications of Advanced Technology to Ash-Related Problems in Boilers* (ed. L. Baxter & R. DeSollar). Springer.

van Ommen, J. R., Coppens, M. O., van den Bleek, C. M. & Schouten, J. C. 2000 Early warning of agglomeration in fluidized beds by attractor comparison. *AIChE Journal* 46 (11), 2183–2197.

van Ommen, J. R., Nijenhuis, J., van den Bleek, C. M. & Coppens, M. O. 2007 Four ways to introduce structure in fluidized bed reactors. *Industrial & Engineering Chemistry Research* 46 (12), 4236–4244.

van Ommen, J. R., Sasic, S., van der Schaaf, J., Gheorghiu, S., Johnsson, F. & Coppens, M. O. 2011 Time-series analysis of pressure

fluctuations in gas-solid fluidized beds - a review. *International Journal of Multiphase Flow* 37 (5), 403–428.

Quevedo, J., Pfeffer, R., Shen, Y., Dave, R., Nakamura, H. & Watano, S. 2006 Fluidization of nanoagglomerates in a rotating fluidized bed. *AIChE Journal* 52 (7), 2401–2412.

Reyes, A., Diaz, G. & Marquardt, F. H. 2001 Analysis of mechanically agitated fluid-particle contact dryers. *Drying Technology* 19 (9), 2235–2259.

van der Schaaf, J., Schouten, J. C. & van den Bleek, C. M. 1998 Origin, propagation and attenuation of pressure waves in gas-solid fluidized beds. *Powder Technology* 95 (3), 220–233.

Schouten, J. C. & van den Bleek, C. M. 1998 Monitoring the quality of fluidization using the short-term predictability of pressure fluctuations. *AIChE Journal* 44 (1), 48–60.

Silva, C. A. M., Parise, M. R., Silva, F. V. & Taranto, O. P. 2011 Control of fluidized bed coating particles using gaussian spectral pressure distribution. *Powder Technology* 212 (3), 445–458.

Silvennoinen, J. 2003 A new method to inhibit bed agglomeration problems in fluidized bed boilers. *ASME Conference Proceedings* 2003, 377–385.

Sobrino, C., Acosta-Iborra, A., Santana, D. & de Vega, M. 2009 Bubble characteristics in a bubbling fluidized bed with a rotating distributor. *International Journal of Multiphase Flow* 35 (10), 970–976.

Sobrino, C., Almendros-Ibanez, J. A., Santana, D. & Vega, M. De 2008 Fluidization of group b particles with a rotating distributor. *Powder Technology* 181 (3), 273–280.

Soria-Verdugo, A., Garcia-Hernando, N., Almendros-Ibanez, J. A. & Ruiz-Rivas, U. 2011 Motion of a large object in a bubbling fluidized bed with a rotating distributor. *Chemical Engineering and Processing* 50 (8), 859–868.

Tatemoto, Y. & Miyazawa, K. 2011 Drying of suspensions in a fluidized bed of inert particles under reduced pressure. *Drying Technology* 29 (10), 1204–1209.

Watano, S., Yeh, N. & Miyanami, K. 1998 Drying of granules in agitation fluidized bed. *Journal of Chemical Engineering of Japan* 31 (6), 908–913.

Werther, J. 1999 Measurement techniques in fluidized beds. *Powder Technology* 102 (1), 15–36.

van Willigen, F. K., Christensen, D., van Ommen, J. R. & Coppens, M. O. 2005 Imposing dynamic structures on fluidised beds. *Catalysis Today* 105 (3-4), 560–568.

van Willigen, F. K., van Ommen, J. R., van Turnhout, J. & van den Bleek, C. M. 2004 Bubble size reduction in electric-field-enhanced fluidized beds. In *AIChE Annual Meeting, Conference Proceedings*, pp. 2795–2799.

Xie, C. G., Huang, S. M., Hoyle, B. S., Thorn, R., Lenn, C., Snowden, D. & Beck, M. S. 1992 Electrical capacitance tomography for flow imaging - system model for development of image-reconstruction algorithms and design of primary sensors. *IEE Proceedings-G Circuits Devices and Systems* 139 (1), 89–98.

Yan, R., Liang, D. T., Laursen, K., Li, Y., Tsen, L. & Tay, J. H. 2003 Formation of bed agglomeration in a fluidized multi-waste incinerator. *Fuel* 82 (7), 843–851.

Zhao, L. J., Pan, Y. K., Li, J. G., Chen, G. H. & Mujumdar, A. S. 2004 Drying of a dilute suspension in a revolving flow fluidized bed of inert particles. *Drying Technology* 22 (1-2), 363–376.

CHAPTER
TWO

Fluidized bed with a rotating distributor operated under defluidization conditions

Contents

2.1 Abstract

The fluidization conditions of a rotating distributor applied to a 3-D bubbling fluidized bed were studied to assess its potential use for counteracting defluidization phenomena. The performance of the fluidized bed operating under nominal conditions was characterized for the rotating and the static distributor configuration. Different methods of analysis in the time and frequency domains were applied to establish the performance of the fluidized bed. The frequency

domain analysis suggests some kind of local structuring of fluidized bed dynamics imposed by the distributor rotation. The punctual injection of water over the surface of the bed leads to a high cohesive wet region that tends to settle down over the distributor, encouraging the bed defluidization. The water-induced defluidization tests reflect an improvement of the fluidization quality with the distributor rotation.

2.2 Introduction

Fluidized beds are used for a variety of applications in a wide range of scales, from small chemical reactors to large coal combustors. The injection of gas-liquid jets or liquid jets into gas-solid fluidized beds is present in many chemical processes such as fluid coking, fluid catalytic cracking, gas-phase polymerization reactions, and production of pharmaceuticals. As a result, the particles are covered by liquid layers that might lead to agglomeration phenomena. Although, particle aggregation is desired in some processes such as granulation, it often enhances serious problems leading to defluidization and channeling in many petrochemical operations. In all cases, an uncontrolled liquid phase in a fluidized bed tends to form sticky agglomerates that usually grow until defluidization occurs. If this process is not recognized, it eventually propagates to partial or total defluidization of the system (Ergudenler & Ghaly, 1993; Bartels *et al.*, 2008).

Many investigations are focused on the mechanisms of formation and distribution of agglomerates inside fluidized beds. The presence of ash might act as a homogeneous glue layer for the formation of agglomerates in the high temperature zones (Ohman *et al.*, 2000). In this way, according to Lin *et al.* (2003), the coating layer may be present as a liquid phase during combustion. Several researchers have studied the agglomeration or mixing processes after liquid injection in a fluidized bed (Book *et al.*, 2011). Bruhns & Werther (2005) suggested that the liquid jet penetrates into the fluidized bed and wets the solids in the vicinity of the nozzle exit, and then, these wet particles are transported into the bed and form agglomerates, which can lead to improper fluidization conditions. Consequently, such "incomplete" fluidization affects the heat and mass transfer rate in fluidized beds, and might lead to local defluidization problems (Silvennoinen, 2003; Visser *et al.*, 2008; Mettanant *et al.*, 2009). Namely, the larger agglomerates tend to settle down over the distributor after being affected by the bed hydrodynamics (Ariyapadi *et al.*, 2003). These particles in the grid-

zone are just slightly influenced by bubble motion and form the so-called "dead zones" between the holes of the distributor (Horio *et al.*, 1980; Agarwal *et al.*, 2011).

The fluidization problems caused by the presence of agglomerates in the zone close to the distributor might be overcomed using a rotating-distributor fluidized bed. The rotation of the distributor promotes an increase in the radial dispersion of particles, preventing temperature gradients by reducing high particle concentration zones present within fluidized beds (Sobrino *et al.*, 2008, 2009). Furthermore, there is some experimental evidence that the stagnant zones just above the distributor could be broken by the rotating distributor, improving the radial and axial mixing at the bottom of the bed (Soria-Verdugo *et al.*, 2011).

In this chapter the rotating distributor is presented as an attempt to re-fluidize water-induced defluidized systems. Consequently, the rotation of the distributor is expected to improve the breakage rate of wet agglomerates formed during the defluidization process.

2.3 Experimental setup

The experiments were carried out in a lab-scale cylindrical Bubbling Fluidized Bed, equipped with an electrical motor capable of imposing a rotation of the distributor. The cylindrical vessel has an inner diameter, D, of 0.192 m, and a height of 1 m. Two different bed heights, h_b, were employed with values of $0.75D$ and $1.5D$.

The distributor was a perforated plate with an open area of 3% and the holes were organized in a triangular mesh with a pitch of 11 mm. During the experiments, it can be discriminated between the rotational distributor case, with an angular velocity of 100 rpm, and the static distributor case, without rotation. A schematic of the mechanical device can be observed in Figure 2.1.

The bed material was silica sand particles, classified as Group B according to Geldart′s classification (Geldart, 1973). The particle density was measured to be 2645.5 kg/m^3 with a standard deviation of 2.5 kg/m^3, and a mean diameter of 683 μm. The fluidization air-flow had a range of 0-900 l/min and was measured by a rotameter. The setup is equipped with an air pre-heater of 9,000 W capable of maintaining a constant inlet temperature of 30 ^{o}C during all the experiments; this inlet temperature was controlled by a PID regulator.

All the experiments were carried out in the same facility. The measurement

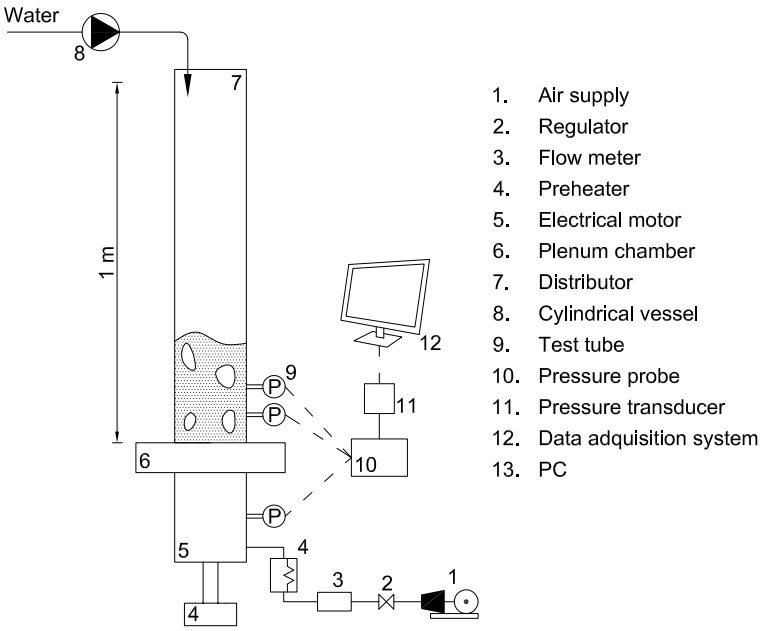

Figure 2.1: Schematic diagram of the experimental fluidized bed.

system consists on 3 pressure local probes with 4 mm of internal diameter and a length of 0.10 m; these dimensions guarantee an undisturbed transfer of the signal (van Ommen *et al.*, 1999). The pressure probes were located through the wall bed and on the opposite side of the water injection; one probe was placed in the plenum and the other two were placed above the distributor at a height of $0.75D/2$ and $0.75D$.

Piezoelectric pressure sensors, Kistler type 7261, were connected to the probes to measure the differential pressure fluctuations. The measurements from the Kistler sensors were amplified using a Kistler amplifier type 50515, which incorporates a low pass filter at 0.16 Hz, and a high pass filter at 200 Hz. The signal was stored in a PC using a National Instruments data acquisition system type 9234 with 4 analog input channels, 24-bit resolution, working at a sampling frequency of 400 Hz.

2.3.1 Methodology

The relative fluidization velocity $U_r = U/U_{mf,r}$ was set to a value of $U_r = 1.6$ during the tests, and the fluidized bed was operated at a constant inlet temperature of 30 ^{o}C. Those settings are referred as "nominal conditions" and define

the steady state operation of the lab-scale fluidized bed; at those conditions no agglomerates are present at the bed. The experiments were carried out for two different aspect ratios, $h_b/D = 0.75$ and $h_b/D = 1.5$. The minimum fluidization velocity was measured following the procedure described by (Wilkinson, 1995; Felipe & Rocha, 2007; Sobrino *et al.*, 2008), being $U_{mf,s} = 0.23$ m/s and $U_{mf,r} = 0.22$ m/s for the static and rotating distributor, respectively.

The water injection on the surface of the bed was carried out 1 m above the distributor (perpendicular to it). The volume of water was instantaneously injected using a test tube to spill the water. The same procedure was used for all the water-induced defluidization tests, starting with the bed running under nominal conditions. Then, water injection started to cause defluidization. Once the bed was defluidized, different attempts to recover the fluidization quality were carried out using the rotating distributor.

2.3.2 Water-induced defluidization mechanism

When a liquid is injected in a fluidized bed it may spread on the bed particles, increasing their cohesiveness and reducing the bed fluidization quality. Moreover, choosing water as liquid and silica sand particles as bed material ensured the occurrence of the agglomeration process (McDougall *et al.*, 2005). After the local injection of water on the surface of the fluidized bed, the liquid injection penetrates into the bed forming a column of wet particles. This column can be described as a large aggregate, with a size of the same order of magnitude as the inner diameter of the cylindrical vessel. The wet agglomerate defines a sticky region characterized by high cohesive forces which tends to settle down over the distributor due to buoyancy effects, improving the growth of dead zones over the distributor plate and facilitating the defluidization phenomena. The interparticles forces characteristic of these regions are high enough to prevent their breakage because of the bubbles motion, i.e. channels from the distributor and through the dense phase might cross these regions with no fluidization of wet solids.

2.4 Method of analysis

The performance of the fluidized bed operating under nominal conditions was characterized for both the rotating and the static distributor. The analysis includes both the time and the frequency domains.

2.4.1 Time domain analysis

The standard deviation of the pressure signal was employed to analyze the behavior of the bed in the time domain. Despite the standard deviation is strongly influenced by the superficial gas velocity (Puncochar *et al.*, 1985), it can be used to monitor the fluidized bed conditions (van Ommen *et al.*, 2004). At least 5,000 samples of pressure fluctuations are required for an accurate characterization of the standard deviation of pressure fluctuations (Wilkinson, 1995). Moreover, the standard deviation of pressure fluctuations registered during the experiment, σ_e, was normalized dividing by the standard deviation of the nominal case, where no water was injected, σ_0, Eq. (2.1). This normalized standard deviation, σ_n, was employed to determine the quality of the fluidization.

$$\sigma_n = \frac{\sigma_e}{\sigma_0} \tag{2.1}$$

2.4.2 Frequency domain analysis

Spectral analyses permit to identify the dominant frequencies characterizing the measured pressure fluctuations time-series (Parise *et al.*, 2011; van Ommen *et al.*, 2011). The power spectral density, PSD, of the input pressure signal was estimated using the averaged modified periodogram method of the spectral estimation. Welch′s method (Welch, 1967) was used for power spectra estimation with a hamming window as window function, using the procedure explained by Johnsson *et al.* (2000). The estimation of the PSD function was conducted by averaging 20 sub-spectra with a frequency resolution ranging between 0.098 Hz $\leq \Delta f \leq$ 0.195 Hz, as a function of the time series length (Johnsson *et al.*, 2000).

The transient power spectral density was also calculated. This is similar to the power spectrum analysis, but the signal is divided into a number of segments and the power spectral density is calculated for each of them. The process results in a set of spectral densities as a function of time (van Ommen *et al.*, 2011). Using this estimation, changes on the frequency of the fluidized bed could be identified and the fluidization regime was established. The parameters used for this method were the same as for the estimation of the power spectral density and the frequency range analyzed was 0-10 Hz (Johnsson *et al.*, 2000).

A method proposed by van der Schaaf *et al.* (2002) was used to decompose the PSD of pressure time-series into local and global components, corresponding to the physical phenomena underlying the pressure time series. This technique provides the measurement of the coherent-output PSD, COP, and the

incoherent-output, IOP, of the measured pressure signals, by comparing the coherence of the pressure time series collected at the plenum with the pressure signals measured at $0.75D/2$. According to van der Schaaf *et al.* (2002) the COP provides information of the global behavior of the fluidized bed, whereas local phenomena, i.e. passing bubbles, are accounted by the IOP function. In this work, this technique was used to study the rotating distributor effect in the fluidized bed.

The change in energy obtained from the power spectrum reflects a change in operational condition/regime (Johnsson *et al.*, 2000). It is expected that the water and sand mixture present in the experiments is capable of modifying the dynamic response of the fluidized bed. This energy is estimated using different regions and can be expressed as a function of the total energy of the power spectrum. The ratio between the energy in a region and the total energy is called wide band energy, defined as

$$E_{WB} = \frac{\sum_{f_{cI}}^{f_{cII}} P_{xx}(f)}{\sum_{f=\Delta f}^{f_N} P_{xx}(f)} \tag{2.2}$$

where $P_{xx}(f)$ is the energy of the PSD as a function of the frequency f, Δf is the lower spectral frequency, whereas f_{cI} and f_{cII} are the lower and upper frequency limits of each region, and f_N is the Nyquist frequency. In the system considered here, three regions are found to divide the frequency domain.

2.5 Results

The results show the effect of the distributor rotation on the lab-scale bed operated both under fluidization and defluidization conditions. First of all, the performance of the rotating distributor with the aspect ratio of $h_b/D = 0.75$ was analyzed in the frequency domain when the bed was operating at nominal conditions. Later, water-induced defluidization experiments are presented for both aspect ratios ($h_b/D = 0.75$ and $h_b/D = 1.5$) and compared with the nominal conditions. The signal used to monitor the rotating distributor effect on the fluidized bed was based on the pressure fluctuation measurements recorded by the sensor located at the plenum (Felipe & Rocha, 2007; Parise *et al.*, 2011).

2.5.1 Nominal characterization

Figure 2.2 shows the power spectra of the bed operating under nominal conditions with $h_b/D = 0.75$. A quite similar behavior in the frequency domain is shown for the static and rotating distributor. The dominant frequency of the spectrum for the static distributor is located at $f_{c,s} = 2.78$ Hz, while for the rotating distributor is $f_{c,r} = 2.63$ Hz. These dominant frequencies are very similar to the natural frequency of the fluidized bed estimated according to Baskakov *et al.* (1986), which is $f_n = 2.66$ Hz. Baskakov showed that this natural frequency is related to the gravitational oscillations of the fluidized bed material which rely on pressure waves or fluctuations generated close to the surface.

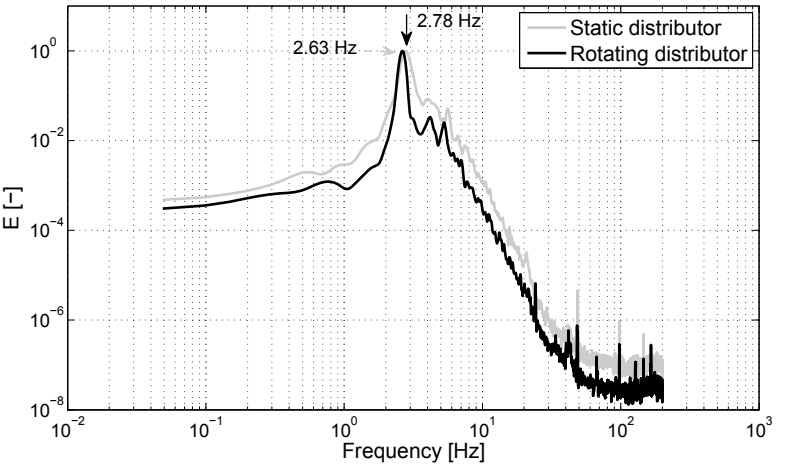

Figure 2.2: Power spectra log-log scale for fluidized bed under nominal conditions with h_b/D= 0.75.

The transient spectral density analyses are presented in Figure 2.3 for the static and the rotating distributor. The high energy frequencies are represented by hot colors (red) and represent the frequency peak observed in the power spectra, as was shown in Figure 2.2. In contrast, the low energy frequencies are represented by cold colors (blue). These transient spectral density analyses are characteristic of the multiple bubble regime (van Ommen *et al.*, 2011). As expected, the spectrograms were also very similar for both the static and the rotating distributor operating under nominal conditions.

The energy of the power spectrum estimated over the entire frequency domain is a useful parameter to characterize the fluidized bed and can be used to

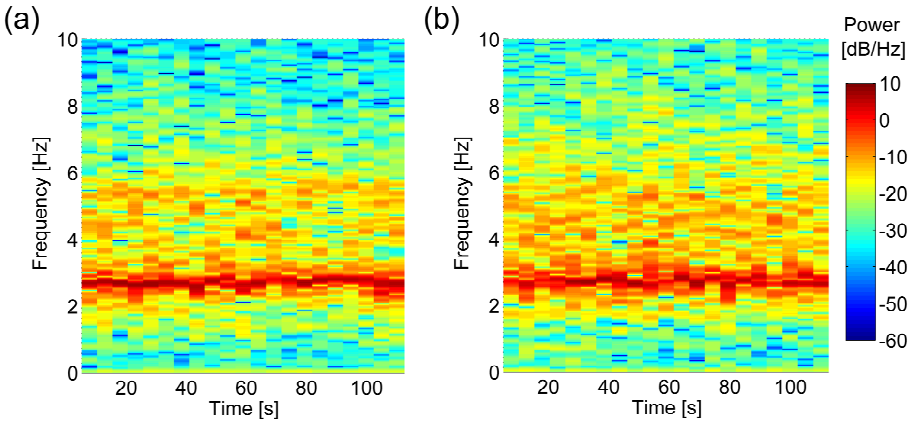

Figure 2.3: Transient spectral density for fluidized bed under nominal conditions with h_b/D= 0.75. (a) Static distributor. (b) Rotating distributor.

describe different events during fluidization. Previous studies (vander Stappen, 1996; van der Schaaf *et al.*, 1999; Johnsson *et al.*, 2000) divided the frequency domain by means of visual inspection of the PSD, analyzing the spectra fall-off with frequency. In this work, the cumulative energy distribution of the PSD was employed in order to reduce the influence of the frequency peaks, which are typically shown in the PSD (Figure 2.2), on the frequency division. Figure 2.4 presents the cumulative energy, which was estimated using Eq. (2.2) for the static and the rotating distributor, plotted in logarithmic axis. The visual inspection of Fig. 2.4 leads to the division of the frequency domain in three regions. In the first region ($\Delta f \leq f \leq 1.3$ Hz) the cumulative energy followed a linear trend and counts on less than 0.2% of the total energy. The second region contains 90% of the signal energy and was determined between 1.3 Hz and 4.5 Hz. Finally, the third region covered from 4.5 Hz to the Nyquist frequency (200 Hz), and contains almost 10% of the energy. According to this division, no meaningful differences were found between the static and the rotating distributor.

In order to show the influence of the rotating distributor on the global and the local phenomenon, COP and IOP functions were estimated. These results are presented in Figure 2.5. According to that analysis, the power spectrum of the plenum pressure signal was compared with the PSD of the pressure signal measured at $0.75D/2$. The COP analysis, which is generated by global phenomena (Figure 2.5-a), reflects the effect of the distributor rotation in the entire bed. This power spectral density shows the higher peak at 2.53 Hz for the

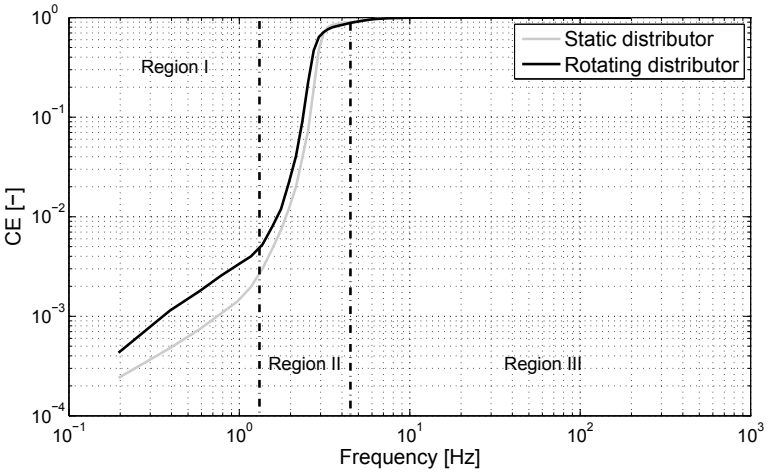

Figure 2.4: Cumulative energy of the fluidized bed under nominal conditions with h_b/D= 0.75.

rotating distributor, whereas the static distributor presents a lower COP with a peak at 2.73 Hz. Such frequencies for the rotating and static distributor are close to the corresponding central frequencies of the PSD spectrum, shown previously in Figure 2.2 ($f_{c,r}$ = 2.63 Hz and $f_{c,s}$ = 2.78 Hz). Since the frequency content characteristic of the global behavior of the fluidized bed recorded at the plenum and at $0.75D/2$ position exhibits a high level of coherence, the downwards compression waves were not affected by the distributor. Therefore, the measurements collected at the plenum can be reliably used to monitor the fluidized bed dynamics either with the static or the rotating distributor. Nevertheless, the rotating distributor COP spectrum presents a higher amplitude than the static distributor, showing some influence of the rotating distributor on the global dynamics.

The local phenomena accounted by the IOP function exhibits both qualitative and quantitative differences for the rotating and the static distributor (Figure 2.5-b). For the static distributor case, there is no peak frequency at 2.73 Hz and the corresponding PSD exhibits a uniform distribution of energy among the frequencies. The IOP analysis of the distributor rotation shows three main frequencies, the main peak centered at 1.6 Hz, which corresponds to the rotating distributor frequency (100 rpm), a secondary peak centered at 2.73 Hz, that matches the major frequency characterizing the COP function, and a third frequency around 4 Hz which also appears in the COP function (Figure 2.5-a). Therefore, there is a strong influence of the rotating distributor on the local

phenomena (e.g. passing bubbles), besides the peak appearing at 1.6 Hz might suggest some kind of local structuring of the fluidized bed dynamics imposed by the distributor rotation at 100 rpm.

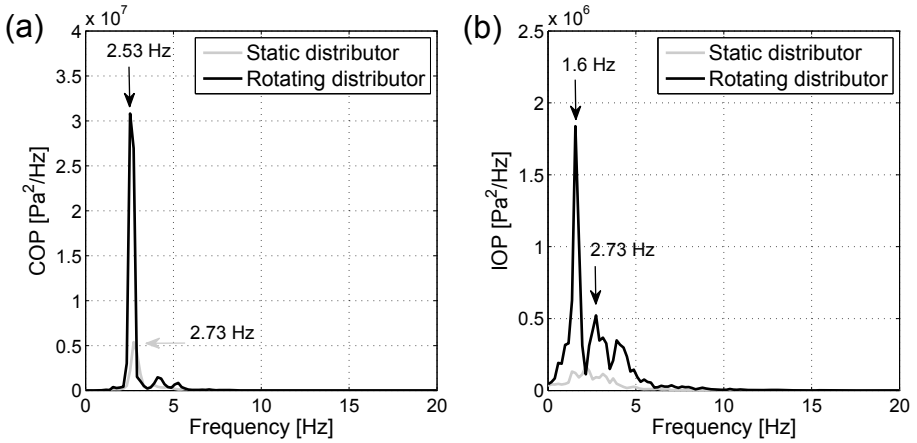

Figure 2.5: Fluidized bed working under nominal conditions with h_b/D= 0.75. (a) COP. (b) IOP.

2.5.2 Punctual injection experiments with h_b/D =0.75

A set of experiments was carried out with a punctual injection of water at the initial time of the experiment, when the fluidized bed was operating under nominal conditions and with the static distributor. Different water volumes were injected on the surface of the bed. Figure 2.6 shows the normalized standard deviation of pressure estimated with Eq. (2.1) for different runs. This graph describes the water-induced defluidization process as well as the recovery of the fluidization quality applying the rotating distributor. For all liquid injection tests, the normalized standard deviation presents similar downward trends for 20-30 s after the water injection. This time between the liquid injection and the defluidization of the bed is defined as the defluidization time. Visual observations confirmed that for the injections of 100 ml, 150 ml and 175 ml, the bed was defluidized around 30 s after the water injection, which is also showed by the normalized standard deviation in Figure 2.6. The visual observations led to establish a minimum level value for the normalized standard deviation of 30%, for which defluidization was reached. In contrast, after the water injection of 50 ml, visual observations showed that there was a deterioration of the fluidization condition with a decrease of the normalized standard deviation value

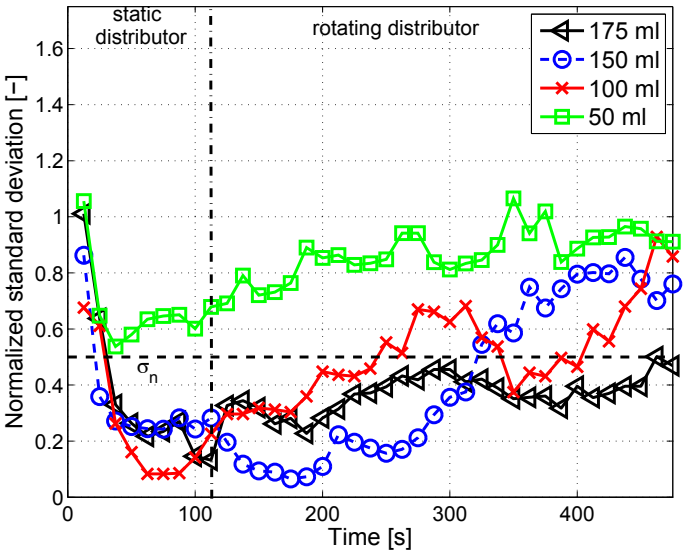

Figure 2.6: Normalized standard deviation of pressure after punctual injections of water with h_b/D= 0.75.

up to roughly 60% of that corresponding to the nominal operation condition, nevertheless the bed was not defluidized. According to that, a value of 50% was established for the normalized standard deviation as a threshold to identify the defluidization state.

According to Figure 2.6, approximately 120 s after the punctual injection of water, the distributor rotation was started in order to counteract the defluidization problem and recover the fluidization quality. In the case of 50 ml water injection, the rotating distributor recovered the fluidization quality easily. After the injection of 100 ml and 150 ml of water, channels were formed in the zone close to the distributor. The distributor rotation broke these channels and dispersed the agglomerates within the bed, improving their drying and breakage. For these tests, the recuperation time, t_r, needed by the normalized standard deviation to reach the value of $\sigma_n = 50\%$ after the water injection, is around $t_r = 150$ s for the injection of 100 ml, and $t_r = 200$ s for the injection of 150 ml. These recuperation times match up with visual observations. Thus, the rotation of the distributor was then found to be an useful tool to increase the normalized standard deviation over the threshold for the injections of 100 ml and 150 ml, which indicates an improvement of the fluidization quality. However, for the injection of 175 ml slight improvements were obtained.

The runs shown in Figure 2.6, were also analyzed in the frequency domain by means of the transient PSD. In Figure 2.7-a/b can be observed that after the water injection of 50 ml and 175 ml, the characteristic frequencies of the fluidized bed located around the central frequency value, $f_{c,s}$, were gradually losing energy during the defluidization process. Such an energy loss was dramatically increased when the agglomerates settled down over the distributor.

Focusing on the punctual injection of 50 ml, Figure 2.7-a confirmed the results shown in Figure 2.6. Thus, as a consequence of the water injection, some peak frequency dissipation occurred, however the main frequency characteristic of the nominal operation conditions was still present in the spectrogram since the bed was not defluidized. Consequently, even though the presence of the agglomerates modified the dynamic transient response of the bed, the bubble motion prevented the agglomerates to reach the distributor plate, hindering the defluidization process.

The defluidization process was assumed to start at the moment when the characteristic frequency of the fluidized bed begins to disappear. For the water injection of 175 ml, Figure 2.7-b shows that the bed was defluidized after 30 s. Thus, the beginning of defluidization estimated with the transient PSD of the pressure signal is in agreement with the previous threshold of $\sigma_n = 50\%$ established by visual inspection for the normalized standard deviation. Moreover, once the agglomerates reached the distributor plate and the fluidized bed became a more cohesive system, channels were observed in the bottom of the bed. These channels were detected in Figure 2.7-b by the appearance of high energies at frequency values around 8 Hz.

Once the bed was defluidized, the distributor rotation was switched on. The bubbles were then more homogenously distributed as a consequence of the local structuring of fluidized bed dynamics imposed by the distributor rotation at 100 rpm, an thus, the dead zones between holes over the distributor were subsequently broken improving the radial and axial mixing at the bottom of the bed (Soria-Verdugo *et al.*, 2011; Sobrino *et al.*, 2008). Therefore, with the rotating distributor the wet regions can be removed from the bottom of the bed, facilitating the drying and breakage of the agglomerates. The recuperation process presented in Figure 2.7-c shows that the re-fluidization time was around $t_r = 200$ s for the 150 ml injection, which is in agreement with the value estimated previously using the time domain analysis. Moreover, as the bed was dried up, the characteristic bed frequency $f_{c,r}$ gradually gained spectral energy. Thus, the stages followed by the system, from defluidization between 0 s and

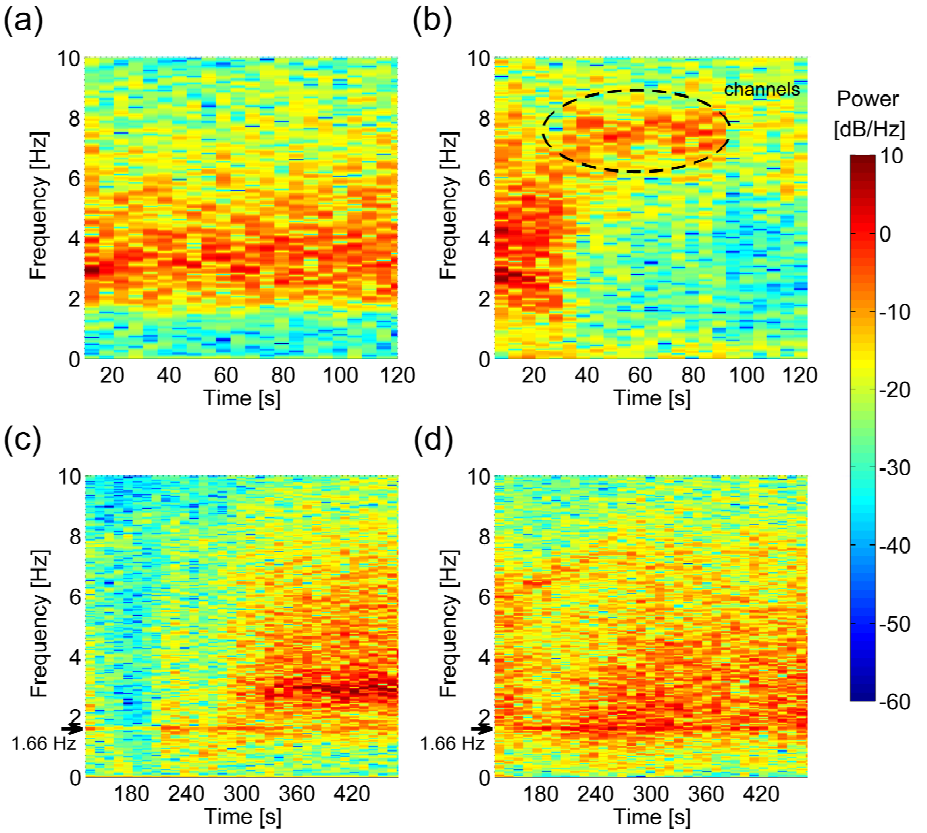

Figure 2.7: Transient PSD with h_b/D= 0.75. (a) Agglomeration after 50 ml punctual injection. (b) Agglomeration after 175 ml punctual injection. (c) Recuperation after defluidization (150 ml of water). (d) Recuperation after defluidization (175 ml of water).

150 s, to gradual fluidization from 150 s to 200 s, are shown in Figure 2.7-c. This spectrogram also detected the rotation frequency of 1.6 Hz from 0 s to 200 s, when the bed was defluidized, which corresponds to the rotation of the distributor at 100 rpm. The spectrogram analysis is also capable of detecting gradual changes in the dynamic of the fluidized bed during the re-fluidization process. In this way, Figure 2.7-b shows the bed completely defluidized, from 30 s to 120 s, with the presence of channels.

Finally for the 175 ml injection, Figure 2.7-d shows that no re-fluidization conditions were achieved and a high energy appeared at the rotation frequency of 1.6 Hz. This result was confirmed with the normalized standard deviation in Figure 2.6. Therefore, after defluidization by the water injection of 175 ml,

the rotating effect was slight and the bed was vaguely re-fluidized during the duration of the test.

Based on the results showed in the spectrograms of Figure 2.7, the changes produced in the frequency domain clearly affect the energy distribution accounted by the wide band energy method. Figure 2.8 presents the energy in each of the regions of the PSD function defined previously in Figure 2.4 as a function of the volume of water injected.

The fluidized bed operating at nominal conditions presented almost the same energy distribution with the static and the rotating distributor, as explained before in Figure 2.4. It can be observed in Figure 2.8-a that the punctual injection of 50 ml modified the energy distribution by decreasing around 10% the energy contained in Region II (E_{WB2}) and transferred it to higher frequencies, Region III (E_{WB3}). This means that the increase of the bed material cohesiveness is reflected at high frequencies (Region III). This energy distribution is similar to that presented after the injection of 100 ml, but in this case, the defluidization was reached due to the greater amount of water injected. Following this tendency, when the amount of water injected was increased, the energy was further transferred from Region II to Region III. The energy contained at low frequencies remained almost constant for the cases in which defluidization was reached. This is explained as a consequence of the appearance of channels in the region close to the distributor plate.

Based on the re-fluidization time showed in Figures 2.6-2.7, the recuperation process was divided to set clearly the energy distribution on the recuperation process, Figure 2.8-b/c. The signal was divided in two intervals in order to identify more clearly the events caused by the rotating distributor. The defluidized

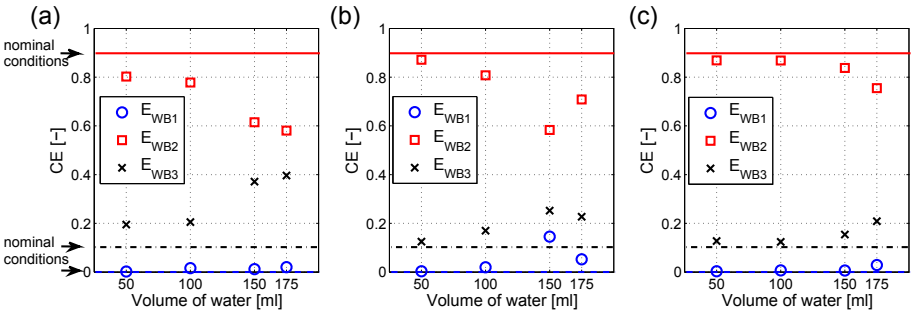

Figure 2.8: Wide band energy with $h_b/D = 0.75$. (a) Punctual injection. (b) Recuperation process with the rotating distributor (120 s - 300 s). (c) Recuperation process with the rotating distributor (300 s - 470 s).

system was considered during the first part, as can be seen in Figure 2.8-b, in which the rate of drying was lower. On the second part, which is presented in Figure 2.8-c, the bed was considered to be operated under nominal fluidization conditions, for the 100 ml and 150 ml cases, or near the fluidization, for the 175 ml case.

After the injection of 50 ml of water, the bed was not defluidized and therefore, the cumulative energy was constant during the recuperation process with the rotating distributor, Figure 2.8-b/c. Then, the energy distribution returned to the values in which there was no liquid. That is, the rotating distributor modified the energy distribution as a consequence of the change in the structure of the bed. As pointed out by Sobrino *et al.* (2008, 2009), a more vigorous fluidization can be achieved applying the distributor rotation and also, it promotes an increase of the radial dispersion of the particles, reducing the high water concentration zones present close to the injection area. These reasons justified the similar energy distributions of the nominal case and the results for 50 ml water injection.

However, in the cases in which defluidization was achieved, differences between the first and the second half of the recuperation process were found. During the first part of the re-fluidization process, Figure 2.8-b the energy of Region III decreased whereas the energy in Region I increased for the cases of 100 ml, 150 ml and 175 ml as a consequence of the distributor rotation. On the other hand, the second part of the recuperation process, Figure 2.8-c, shows that the level of energy was recovered to values approaching the nominal state, where re-fluidization occurred (100 ml and 150 ml). The effect of the rotating distributor improved the fluidization conditions by the breakage of agglomerates, even for the 175 ml case, which was still poorly fluidized.

2.5.3 Elimination of the defluidized state for deeper beds

In this section, the counteracting effect of the rotating distributor applied to deep beds is studied. Following the methodology used before, water-induced defluidization experiments for deep beds ($h_b/D = 1.5$) are presented and compared with the results obtained for shallow beds ($h_b/D = 0.75$). Moreover, in these tests for deep beds the volume of water was fixed to 150 ml since it produced a deep defluidization, allowing the recuperation process to occur in a reduced time.

First of all, the fluidization regime of the bed working with $h_b/D = 1.5$ was studied by means of the power spectral density. Figure 2.9 compares the PSD

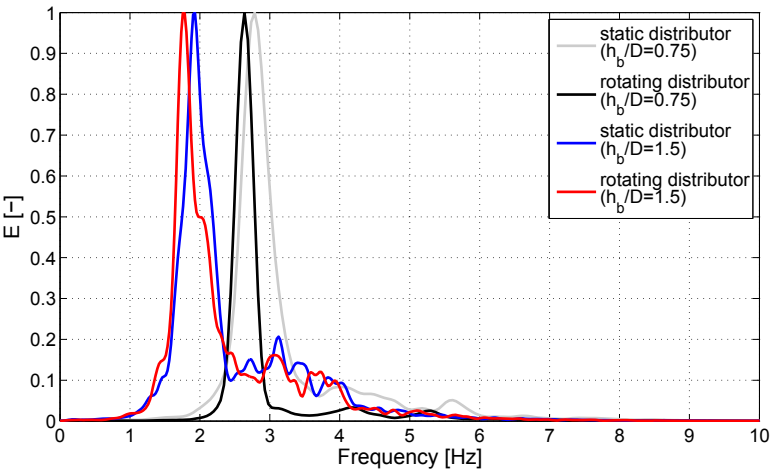

Figure 2.9: PSD for $h_b/D = 0.75$ and $h_b/D = 1.5$.

of the bed working under nominal conditions with and without the rotating distributor for both aspect ratios. In the case of $h_b/D = 1.5$, the dominant frequency of the spectrum for the static distributor was $f_{c,s} = 1.93$ Hz, while for the rotating distributor was $f_{c,r} = 1.76$ Hz. These dominant frequencies are close to the Baskakov frequency ($f_n = 1.85$ Hz), as for the case of $h_b/D = 0.75$, indicating that the increase of the aspect ratio maintained the single bubble regime for both the static and rotating distributor cases.

Figure 2.10 shows the normalized standard deviation for the water-defluidization and recuperation processes studied for $h_b/D = 0.75$ and $h_b/D = 1.5$. As can be seen in Figure 2.10, the fluidization quality was recovered for both tests by means of the rotating distributor. After the water injection, the defluidization time was almost the same for both heights, around 30 s. Once the bed was defluidized, the rotating distributor was switched on after 60 s of the water injection in order to break the dead zones and channels. According to the normalized standard deviation, the recovery time was around $t_r = 250$ s for the shallow bed, whereas for the deep bed it was around $t_r = 430$ s. This increase in the recuperation time for the deep bed indicate that, as a consequence of the increase in the aspect ratio, the presence of slugs reduced the mixing degree in the fluidized bed. Furthermore, this increase of the recuperation time, almost the double comparing both heights, suggests that the mixing degree of the deep bed is inversely proportional to the aspect ratio. In both cases, the local effect of the rotating distributor broke the channels formed close to the distributor,

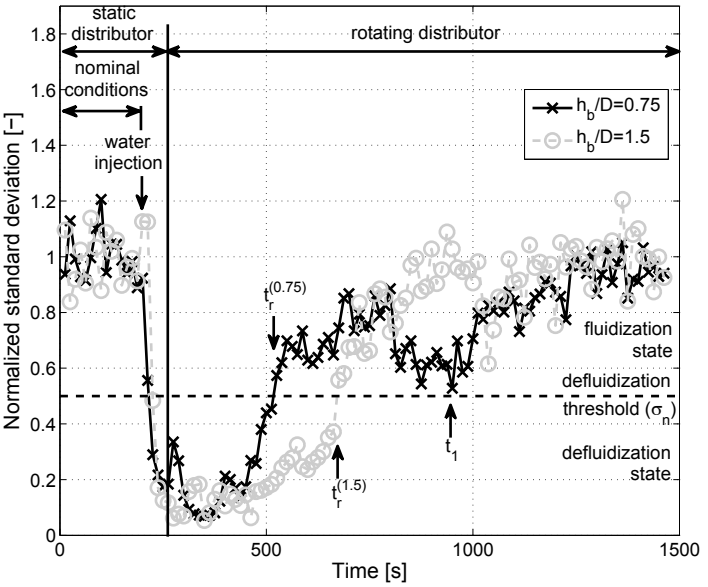

Figure 2.10: PSD for $h_b/D = 0.75$ and $h_b/D = 1.5$.

improving the fluidization quality. In the case of the shallow bed, a smooth decrease on the standard deviation occurred at $t_1 = 700$ s after the water injection, which was produced by the motion of the agglomerates. On the other hand, the recuperation process of the deep bed, $h_b/D = 1.5$, was gradual until the bed was properly fluidized. Moreover, in this case from 550 s to the end of the experiment, the significant fluctuations of the standard deviation reflect the decrease of the mixing degree due to the plug flow regime.

Analyzing the frequency domain with the transient PSD, Figure 2.11, the bed defluidization was also detected for deep beds. Due to the distributor rotation, the channels were broken and not appeared in the high frequency region for both recuperation processes. Therefore, similar recuperation times were obtained using both the transient spectrogram and the normalized standard deviation for deep beds.

The mass ratio between the water injected and the bed material was lower for the deep bed than for the $h_b/D = 0.75$ case, and thus, the agglomerates can be distributed in a different way, slightly affecting the recuperation process. Therefore, the wide band energy was estimated in Figure 2.12 as a function of time in order to analyze whether or not the energy distribution during the re-fluidization process for deep beds is similar to the $h_b/D = 0.75$ case.

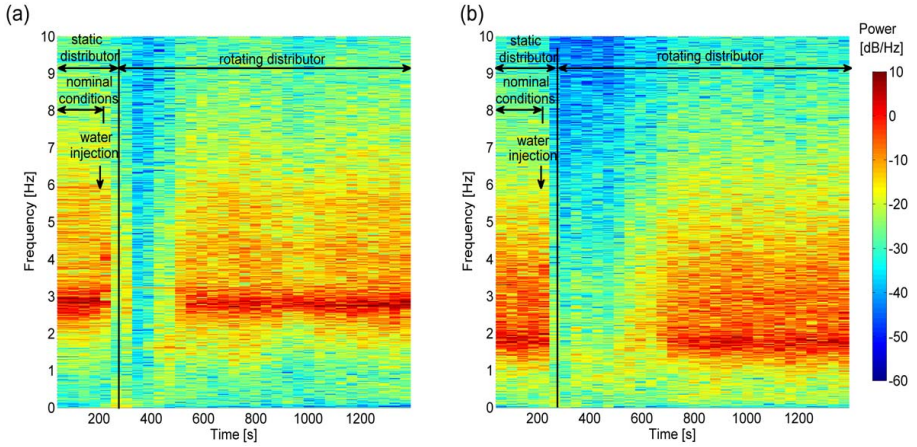

Figure 2.11: Transient PSD. (a) $h_b/D = 0.75$. (b) $h_b/D = 1.5$.

As shown in Figure 2.9, the increase of the bed aspect ratio reduced the central frequency of the bed. Thus, the frequency ranges that divide the cumulative energy distribution of the fluidized bed working with $h_b/D = 1.5$ under nominal conditions varied to new values, which were used to estimate the wide band energy. For $h_b/D = 1.5$, the first region was limited between $\Delta f \leq f \leq 0.8$ Hz, the second region was determined from 0.8 Hz to 4 Hz, and the third region covered from 4 Hz to the Nyquist frequency.

Figure 2.12 represents the wide band energy estimated each 100 s during the whole test. In this test, 150 ml were injected and the recuperation process was carried out with the static distributor. As can be observed in the figure, after the water injection a decrease on the energy contained in Region II occurred, and this energy was transferred to the Region III. This transference of energy was caused by the channels formation near the distributor as a result of the presence of agglomerates on the dead zones over the distributor. Such a behavior was also shown in the $h_b/D = 0.75$ case, Figure 2.8-a, but the energy transferred to the Region III was almost 30% in that case, whereas for the $h_b/D = 1.5$ case, the energy transferred was just around 10%, Figure 2.12.

This difference between the energy values of Region III for $h_b/D = 0.75$ and $h_b/D = 1.5$ tests was caused by the different distribution of the agglomerates after the water injection. During the recuperation process with the static distributor presented in Figure 2.12, the bed with $h_b/D = 1.5$ can be described as a system having two fluidization zones, upper and bottom bed zones. In the bottom zone, which was located close to the distributor, the channels appeared

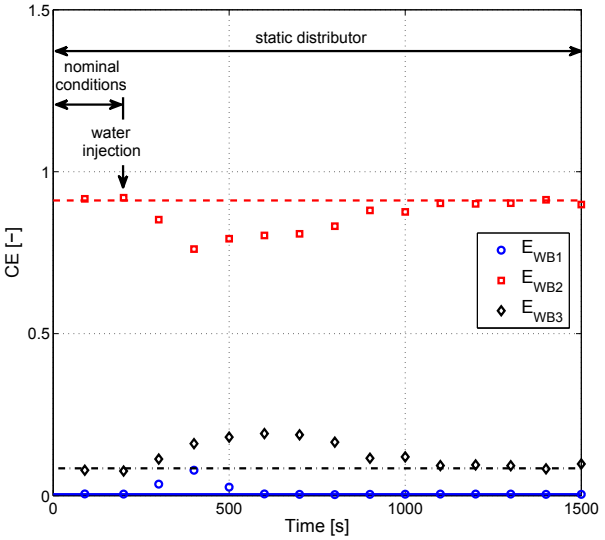

Figure 2.12: Wide band energy as a function of time after the water injection with static distributor ($h_b/D = 1.5$).

in the same way that for the $h_b/D = 0.75$ case. Accordingly, the defluidization process occurred and the gas flowed through the channels across that region. However, due to the increase of the bed height, the upper zone apparently suffered no defluidization phenomena and consequently the bed was partially fluidized in that upper region, where no channels appeared. For this reason, the pressure signal measured at the plenum were affected by the compression waves travelling downwards as a consequence of the partial fluidization of the upper region as well as by the channelling process. Therefore, the energy transferred from Region II to Region III was limited to 10% for $h_b/D = 1.5$. Finally, the fluidization quality was recovered with the static distributor around $t_r = 900$ s after the water injection (Figure 2.12).

2.6 Conclusions

The water induced defluidization tests reflect an improvement of the fluidization quality with the rotating distributor. During the fluidization with nominal conditions, the fluidized bed with the rotating distributor operates near to the Baskakov′s frequency. Therefore, the rotation of the distributor might be able to introduce a dynamic structure into a gas-solid fluidized bed.

The punctual injection of water on the surface of the bed with the static

distributor causes a gradual decrease of the bed fluidization quality. The rotating distributor was proved to be able to recover the nominal operational steady state conditions for shallow, $h_b/D = 0.75$, and deep, $h_b/D = 1.5$, beds. The rotating distributor improved the fluidization quality even when the bed was not yet defluidized, under those conditions the aggregate cohesive zones can be moved and subsequently broken during the drying process.

Finally, the proposed methodology of signal analysis used in this work was proved to detect changes in the dynamic behavior of a fluidized bed. The COP/IOP analyses proved the reliability of the plenum pressure signal. Moreover, the cumulative energy distribution showed the frequencies of interest during the fluidization, which were used for the wide band energy tool. On the other hand, the frequency domain analyses, such as transient PSD and wide band energy, clearly showed the effect of defluidization after the water injection and facilitate the determination of the quality of the fluidization. Furthermore, both techniques demonstrate that, after water-induced defluidization, the appearance of channels produce a net transfer of energy to higher frequencies within the measured pressure fluctuations signals.

Notation

D	Inner diameter of the vessel [m]
E	Energy [-]
E_{WB}	Wide band energy [-]
f	Frequency [Hz]
f_{cI}	Lower frequency limit [Hz]
f_{cII}	Upper frequency limit [Hz]
$f_{c,r}$	Characteristic frequency with rotating distributor [Hz]
$f_{c,s}$	Characteristic frequency with static distributor [Hz]
f_n	Natural frequency [Hz]
f_N	Nyquist frequency [Hz]
h_b	Fixed bed height [m]
h_b/D	Bed aspect ratio [-]
P_{xx}	Power [Pa^2/Hz]
U	Gas velocity [m/s]
U_r	Relative gas velocity [-]
$U_{mf,r}$	Minimum fluidization velocity with rotating distributor [m/s]
$U_{mf,s}$	Minimum fluidization velocity with static distributor [m/s]

t	Time [s]
t_r	Recuperation time [s]

Greek symbols

Δf	Frequency resolution [Hz]
σ_0	Standard deviation under nominal conditions [Pa]
σ_e	Standard deviation during the experiments [Pa]
σ_n	Normalized standard deviation [-]

Abbreviattions

CE	Cumulative energy [-]
COP	Coherent-output PSD
IOP	Incoherent-output PSD
PID	Proportional-integral-derivative controller
PSD	Power spectra density

References

Agarwal, G., Lattimer, B., Ekkad, S. & Vandsburger, U. 2011 Influence of multiple gas inlet jets on fluidized bed hydrodynamics using particle image velocimetry and digital image analysis. *Powder Technology* 214 (1), 122–134.

Ariyapadi, S., Holdsworth, D. W., Norley, C. J. D., Berruti, F. & Briens, C. 2003 Digital x-ray imaging technique to study the horizontal injection of gas-liquid jets into fluidized beds. *International Journal of Chemical Reactor Engineering* 1.

Bartels, M., Lin, W., Nijenhuis, J., Kapteijn, F. & van Ommen, J. R. 2008 Agglomeration in fluidized beds at high temperatures: Mechanisms, detection and prevention. *Progress in Energy and Combustion Science* 34 (5), 633–666.

Baskakov, A. P., Tuponogov, V. G. & Filippovsky, N. F. 1986 A study of pressure-fluctuations in a bubbling fluidized-bed. *Powder Technology* 45 (2), 113–117.

Book, G., Albion, K., Briens, L., Briens, C. & Berruti, F. 2011 On-line detection of bed fluidity in gas-solid fluidized beds with liquid injection by passive acoustic and vibrometric methods. *Powder Technology* 205 (1-3), 126–136.

Bruhns, S. & Werther, J. 2005 An investigation of the mechanism of liquid injection into fluidized beds. *AIChE Journal* 51 (3), 766–775.

Ergudenler, A. & Ghaly, A. E. 1993 Agglomeration of silica sand in a fluidized-bed gasifier operating on wheat straw. *Biomass & Bioenergy* 4 (2), 135–147.

Felipe, C. A. S. & Rocha, S. C. S. 2007 Prediction of minimum fluidization velocity of gas-solid fluidized beds by pressure fluctuation measurements - analysis of the standard deviation methodology. *Powder Technology* 174 (3), 104–113.

Geldart, D. 1973 Types of gas fluidization. *Powder Technology* 7 (5), 285–292.

Horio, M., Kiyota, H. & Muchi, I. 1980 Particle movement on a perforated plate distributor of fluidized-bed. *Journal of Chemical Engineering of Japan* 13 (2), 137–142.

Johnsson, F., Zijerveld, R. C., Schouten, J. C., van den Bleek, C. M. & Leckner, B. 2000 Characterization of fluidization regimes by time-series analysis of pressure fluctuations. *International Journal of Multiphase Flow* 26 (4), 663–715.

Lin, W. G., Dam-Johansen, K. & Frandsen, F. 2003 Agglomeration in bio-fuel fired fluidized bed combustors. *Chemical Engineering Journal* 96 (1-3), 171–185.

McDougall, S., Saberian, M., Briens, C., Berruti, F. & Chan, E. 2005 Effect of liquid properties on the agglomerating tendency of a wet gas-solid fluidized bed. *Powder Technology* 149 (2-3), 61–67.

Mettanant, V., Basu, P. & Butler, J. 2009 Agglomeration of biomass fired fluidized bed gasifier and combustor. *Canadian Journal of Chemical Engineering* 87 (5), 656–684.

Ohman, M., Nordin, A., Skrifvars, B. J., Backman, R. & Hupa, M. 2000 Bed agglomeration characteristics during fluidized bed combustion of biomass fuels. *Energy & Fuels* 14 (1), 169–178.

van Ommen, J. R., de Korte, R. J. & van den Bleek, C. M. 2004 Rapid detection of defluidization using the standard deviation of pressure fluctuations. *Chemical Engineering and Processing* 43 (10), 1329–1335.

van Ommen, J. R., Sasic, S., van der Schaaf, J., Gheorghiu, S., Johnsson, F. & Coppens, M. O. 2011 Time-series analysis of pressure fluctuations in gas-solid fluidized beds - a review. *International Journal of Multiphase Flow* 37 (5), 403–428.

van Ommen, J. R., Schouten, J. C., vander Stappen, M. L. M. & van den Bleek, C. M. 1999 Response characteristics of probe-transducer systems for pressure measurements in gas-solid fluidized beds: how to prevent pitfalls in dynamic pressure measurements. *Powder Technology* 106 (3), 199–218.

Parise, M. R., Silva, C. A. M., Ramazini, M. J. & Taranto, O. P. 2011 Identification of defluidization in fluidized bed coating using the gaussian spectral pressure distribution. *Powder Technology* 206 (1-2), 149–153.

Puncochar, M., Drahos, J., Cermak, J. & Selucka, K. 1985 Evaluation of minimum fluidization velocity in gas fluidized beds from pressure fluctuations. *Chemical Engineering Communications* 35 (1-6), 81–87.

van der Schaaf, J., Johnsson, F., Schouten, J. C. & van den Bleek, C. M. 1999 Fourier analysis of nonlinear pressure fluctuations in gas-solids flow in cfb risers - observing solids structures and gas/particle turbulence. *Chemical Engineering Science* 54 (22), 5541–5546.

van der Schaaf, J., Schouten, J. C., Johnsson, F. & van den Bleek, C. M. 2002 Non-intrusive determination of bubble and slug length scales in fluidized beds by decomposition of the power spectral density of pressure time series. *International Journal of Multiphase Flow* 28 (5), 865–880.

Silvennoinen, J. 2003 A new method to inhibit bed agglomeration problems in fluidized bed boilers. *ASME Conference Proceedings* 2003, 377–385.

Sobrino, C., Acosta-Iborra, A., Santana, D. & de Vega, M. 2009 Bubble characteristics in a bubbling fluidized bed with a rotating distributor. *International Journal of Multiphase Flow* 35 (10), 970–976.

Sobrino, C., Almendros-Ibanez, J. A., Santana, D. & Vega, M. De 2008 Fluidization of group b particles with a rotating distributor. *Powder Technology* 181 (3), 273–280.

Soria-Verdugo, A., Garcia-Hernando, N., Almendros-Ibanez, J. A. & Ruiz-Rivas, U. 2011 Motion of a large object in a bubbling fluidized bed with a rotating distributor. *Chemical Engineering and Processing* 50 (8), 859–868.

vander Stappen, M. L. M. 1996 Chaotic hydrodynamics of fluidized beds.

Visser, H. J. M., van Lith, S. C. & Kiel, J. H. A. 2008 Biomass ash-bed material interactions leading to agglomeration in fbc. *Journal of Energy Resources Technology* 130 (1), 011801.

Welch, P. 1967 The use of fast fourier transform for the estimation of power spectra. *Audio and Electroacoustics, IEEE Transactions on* 15 (2), 70–73.

Wilkinson, D. 1995 Determination of minimum fluidization velocity by pressure fluctuation measurement. *Canadian Journal of Chemical Engineering* 73 (4), 562–565.

CHAPTER

THREE

Wide band energy analysis of fluidized bed pressure fluctuation signals using a frequency division method

Contents

3.1 Abstract

A statistical method based on the approximation of the cumulative energy distribution by Student′s t-distribution is proposed for the unbiased frequency domain division. The methodology divided systematically the frequency domain into three regions. This new methodology was compared with the traditional approach for the frequency domain division, which estimates the different regions

using a visual inspection method. The reliability of the Student′s t-approach to divide the frequency domain was shown for different fluidization velocities, changing the bed aspect ratio and using different pressure probes. The energy of the power spectrum contained within the frequency regions obtained by the visual method is not able to detect changes in the bed aspect ratio or the beginning of the rotating distributor. No meaningful differences could be observed in the frequency regions using different quality pressure sensors because the approach using Student′s t-distribution focuses on the sharp energy increase produced by the primary frequencies of the power spectrum. Water-induced defluidization tests were conducted to illustrate the use of the wide band energy as a monitoring tool. The sensitivity exhibited by the proposed frequency division approach, for the range of fluidization conditions tested, improves the use of the energy contained in these regions as a diagnostic tool in fluidized bed processes.

3.2 Introduction

Pressure fluctuations are one of the most commonly measured parameters employed for the monitoring of fluidized beds (van der Schaaf *et al.*, 1998). There are several methods proposed in the literature to analyze such signals, which can be grouped into three categories as a function of the domain type: (i) time, (ii) frequency and (iii) state space (van Ommen *et al.*, 2011). Focusing on the frequency domain analysis, it is typically performed using power spectral density (PSD) analysis (Brown & Brue, 2001).

The frequency analysis of pressure fluctuations is used to obtain information about the fluidization dynamics and to diagnose the fluidization state (Kage *et al.*, 2000). Characteristic features of the power spectrum have been used for the description of the fluidization regime. For example, the frequency peak and the dominant frequency have been used to detect defluidization in coating and drying processes (de Martin *et al.*, 2011; Parise *et al.*, 2011). The coherent standard deviation and the average frequency of pressure fluctuations have also been used to estimate the bubble size and to detect the regime transitions in slurry bubble columns (Chilekar *et al.*, 2005; Ruthiya *et al.*, 2005). Similarly, the type of power spectrum fall-off with frequency has been used as a tool to distinguish between deterministic or noise systems (vander Stappen, 1996; van der Schaaf *et al.*, 1999; Johnsson *et al.*, 2000; van der Schaaf *et al.*, 2004; van Ommen *et al.*, 2011). Another important parameter obtained from the frequency domain is

the energy contained within the power spectrum. According to Johnsson *et al.* (2000), the wide band energy reflects the change in operational regimes and can be used to characterize the structure of a fluidized bed. In this way, Chapter 2 showed the capability of the wide band energy to detect the defluidization phenomena.

The use of the wide band energy as a monitoring tool presents some advantages in comparison to other parameters obtained from the frequency domain. The easy and fast computation of the wide band energy provides a reliable view of the dynamic behavior of the system, once the power spectrum is properly divided into a set of frequency regions (van der Schaaf *et al.*, 2002; Briongos & Soler, 2003; van der Schaaf *et al.*, 2004; Gómez-Hernández *et al.*, 2012). Traditionally, this type of frequency division has been conducted using visual selection of the cut-off frequencies between the different spectral regions. In this procedure, the observer visually identifies the frequency limits by studying the behavior of the frequency domain either in the power spectrum (vander Stappen, 1996; van der Schaaf *et al.*, 1999; Johnsson *et al.*, 2000) or as the cumulative energy distribution (Chapter 2). In the previous chapter, the frequency limits were visually fixed analyzing the changes in the slope of the cumulative energy distribution of the power spectrum. The results shown for the monitoring of water-induced defluidization tests led us to further study the frequency domain division. In spite of the capability of the wide band energy to detect the channels appearance and the bed defluidization, the visual division of the frequency domain has at least two major drawbacks: i) the cut-off frequencies obtained through the visual inspection depend on the observer; and ii) the power spectrum fall-off is unavoidably affected by the quality of the measured signal, i.e. the transducer type and the signal conditioning. Consequently, the division of the frequency domain as a function of the power spectra or the cumulative energy distribution is not always a reliable process. Therefore, to conduct a reliable wide band energy computation, it is necessary to remove the influence introduced by the observer and the signal quality.

In this study, a procedure for the systematic computation of the wide band energy is developed. The proposed methodology is based on a Student′s t-distribution fitting of the power spectrum cumulative energy (CE). The Kolmogorov-Smirnov test is used to compare the cumulative energy with the Student′s t-distribution. As a result, three frequency regions were found. The comparison between the CE and the Student′s t-distribution discriminates the cut-off frequencies that define the three frequency regions.

3.3 Experimental setup

Two cylindrical lab-scale bubbling fluidized beds were used for the experiments. The first apparatus is a cylindrical poly methyl methacrylate vessel with 0.07 m in inner diameter, d, and 1 m in height. The air distributor consists of 7 tuyeres with eight holes of 0.5 mm diameter. The plenum was filled with a metallic mesh to ensure homogeneous air distribution. The bed aspect ratio was fixed at $h_b/d = 1$ for all the experiments. The measurement system in this facility consisted of one pressure probe placed at the plenum chamber with 4 mm inner diameter and 0.10 m length. These dimensions guarantee an undisturbed transfer of the signal (van Ommen *et al.*, 1999). A Kistler sensor, type 7261, was connected to this probe to measure the differential pressure fluctuations.

The second fluidized bed facility, shown in Figure 3.1, is equipped with an electric motor to rotate the distributor, therefore, the facility can work in static or rotating conditions. The cylindrical vessel has an inner diameter, D, of 0.192 m, and a height of 1 m. The rotating distributor consists of a perforated plate with 275 orifices of 2 mm in diameter, arranged in a triangular configuration with a pitch of 11 mm. Two types of experiments were conducted in this facility, those with the distributor rotating at an angular velocity of 100 rpm and those with a static distributor. The pressure fluctuations in the rotating distributor bed were measured using 2 pressure probes, as can be observed in Figure 3.1. The pressure probes were introduced through the bed wall; one probe was placed at the plenum chamber and the other probe was located above the distributor at a height of $0.75D/2$. The probe dimensions for this facility are similar to those of the smaller facility. Two Kistler and Honeywell (SPT type) pressure sensors were connected to the plenum chamber. Also, another Kistler sensor was placed at a height of $0.75D/2$ above the distributor.

The bed material employed was silica sand particles for all the experiments, classified as Group B according to Geldart′s classification (Geldart, 1973). The particle density was measured to be 2645.5 kg/m^3 with a standard deviation of 2.5 kg/m^3, and a mean diameter of 683 μm. Both beds were fluidized with air at ambient conditions, and the airflow was measured with a rotameter. The minimum fluidization velocity was measured to be $U_{mf,s} = 0.33$ m/s and $U_{mf,r} = 0.31$ m/s for the static and rotating distributor, respectively (Sobrino *et al.*, 2008), and similar values were obtained for the smaller bed.

The measurements from the Kistler sensors were amplified using a Kistler amplifier type 50515. The signals were stored in a PC using a National Instruments data acquisition system type 9234 for the Kistler measurements and

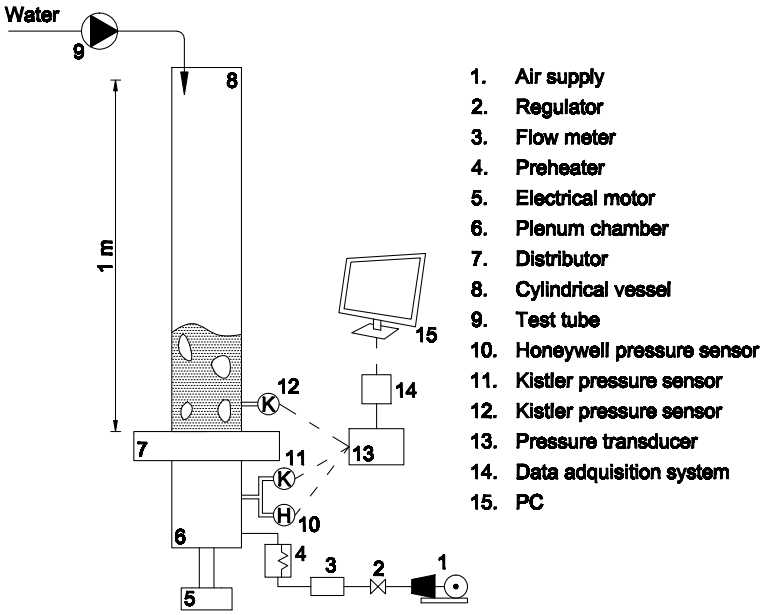

Figure 3.1: Schematic diagram of the experimental fluidized bed equipped with a rotating distributor.

type 9205 for the Honeywell pressure signals, working in both cases at a sampling frequency of 400 Hz. All signals were filtered through a low pass filter at 0.16 Hz and a high pass filter at 200 Hz.

3.4 Experimental procedure

Three types of tests were conducted to study the feasibility of the frequency division method: (i) varying the relative fluidization velocity, $U_r = U/U_{mf}$, (ii) changing the bed height, and (iii) studying the water-induced defluidization process. A summary of the different experiments carried out can be found in Table 3.1.

Experiments to analyze the effect of varying the relative fluidizaiton velocity were conducted in the small fluidized bed ($d = 0.07$ m) by changing the relative velocity, U_r, from 1.9 to 3.78 at a constant bed aspect ratio of $h_b/d = 1$. The raw pressure signal data recorded at the plenum chamber with the Kistler sensor were used to determine the improvement of the proposed method compared with the visual detection method.

The effect of the bed aspect ratio on the natural bed frequency was used

Table 3.1: Summary of the experiments.

Facility	Test	h_b/D	U_r	Distributor state
$d = 0.07$ m	1	1	1.9 2.84 3.78	-
$D = 0.19$ m	2	0.75 1.5 2	1.6	static
	3	0.75	1.6	static rotating

to test the reliability of the frequency division method (van der Schaaf *et al.*, 2004). By increasing the bed height in the fluidized bed equipped with the rotating distributor ($D = 0.19$ m), slug type fluidization was induced. The dynamic features of the fluidized bed were then modified by varying the bed aspect ratio, $h_b/D = 0.75$, 1.5 and 2. In these tests, the relative fluidization velocity was constant at $U_r = 1.6$, where the bed was shown to be well-fluidized (Chapter 2). The effect of the pressure probe location and the influence of the pressure sensor type were also analyzed.

Water-induced defluidization experiments were carried out using the rotating distributor facility ($D = 0.19$ m) to illustrate the use of the wide band energy as a monitoring tool. Applying the proposed frequency division methodology, the frequency domain was divided into three regions, in which the energy of the power spectrum was calculated. In these tests, the aspect ratio was fixed at $h_b/D = 0.75$, and the fluidization velocity was $U_r = 1.6$. According to Chapter 2, the tests started with the bed working without the presence of agglomerates, i.e. under nominal conditions. Then, 150 ml of water was injected on the surface of the bed, at a distance of 1 m perpendicular to the distributor, causing the defluidization of the bed. The rotating distributor was then used to counteract the defluidization phenomenon.

3.5 Frequency division method

As stated above, the estimation of the wide band energy requires the identification of different frequency regions in the frequency domain. In this section, an unbiased and systematic method is proposed to identify the frequencies that

divide the power spectrum.

The method assumes that the high energy region of the cumulative energy distribution can be approximated with a statistical distribution. The distribution fits the high energy region of the CE with high accuracy; this region is usually centered on the dominant frequency region of the spectrum. However, the CE distribution tails are not well-approximated by the statistical distribution. This result was used in the proposed method to identify the spectral boundary regions. The region of coincidence between the statistical and experimental CE distributions was identified using the Kolmogorov-Smirnov test. In this way, the CE frequency distribution can be divided into three regions: two poorly matched regions (Regions t-I and t-III), which correspond to the tails of the CE distribution, and a well-matched region (Region t-II), which corresponds to the highest energy content of the distribution. Several statistic distributions were analyzed to fit the cumulative energy distribution. The experimental conditions in this study favored the use of the Student′s t-distribution as the most suitable statistical distribution to fit the experimental data. The methodology can be applied using any statistical distribution that appropriately fits the data.

The Student′s t-distribution is well-known in statistics and, in its non-standardized form, is expressed as follows

$$p(x|\mu,\lambda,\nu) = \frac{\Gamma(\nu+1/2)}{\Gamma(\nu/2)}\left(\frac{\lambda}{\pi\nu}\right)^{1/2}\left(1+\frac{\lambda(x-\mu)^2}{\nu}\right)^{-(\nu+1)/2} \tag{3.1}$$

where $p(x)$ denotes the Student′s probability density function (PDF) of the variable x with location parameter μ, scale parameter $\lambda \geq 0$, and shape parameter $\nu \geq 0$. These parameters are estimated according to the maximum-likelihood estimation (MLE) method (Dempster, 1977).

The Kolmogorov-Smirnov test is a simple method to test whether an empirical sample follows a specific distribution, which is the null hypothesis (H_0), against the alternative hypothesis (H_1) that it follows a different distribution. The test compares the empirical cumulative distribution function of the sample, $S_n(x)$ (i.e. the cumulative energy distribution), with the cumulative distribution function (CDF), which is the fitted statistic distribution

$$D_n = \max|S_n - CDF(x)| \tag{3.2}$$

where D_n is the distance between the cumulative distributions. The distance, D_n, is used to obtain the modified statistic, D^*, as shown in Eq. (3.3), which is compared with the critical values of the test for a certain level of significance,

α (Stephens, 1970). The modified statistic, D^*, is a function of the sample size (n), computed as a function of the size of both cumulative distributions (n_1 and n_2) by Eq. (3.4)

$$D^* = D_n(\sqrt{n} + 0.11 + 0.12/\sqrt{n}) \tag{3.3}$$

$$n = \frac{n_1 n_2}{n_1 + n_2} \tag{3.4}$$

The Kolmogorov-Smirnov test is constructed using the critical values of the Kolmogorov distribution (Stephens, 1970). The null hypothesis is rejected at level of significance α if $D^* \geq K_\alpha$, where K_α is found from the Kolmogorov distribution as follows

$$Pr(K \leq K_\alpha) = 1 - \alpha \tag{3.5}$$

The procedure for processing the pressure signal is outlined in Figure 3.2 and can be summarized as follows:

- Determination of the power spectrum of the pressure signal using Welch′s method, as shown in Figure 3.2-a for an example of a pressure signal (Welch, 1967).

- Computation of the cumulative energy in the frequency domain. The result for the example analyzed can be observed in Figure 3.2-b.

- Fitting of the cumulative energy function to the Student′s t-distribution. The fitting was performed using the maximum-likelihood estimation method (MLE), assuming that the cumulative energy distribution is distributed as a Student′s t-distribution with unknown characteristic parameters μ, λ, ν (Fisher, 1925; Dempster, 1977).

- Determination of the goodness of fit between the cumulative energy and the cumulative density function (CDF) of the Student′s t-distribution′s using the standard error of the estimated parameters. The standard errors of the location, scale and shape parameters were analyzed. When the standard error values of the shape parameter were below $\hat{\sigma_\nu} = 0.07$, the cumulative energy distribution was found to be well-approximated by the Student′s t-distribution.

- Division of the frequency regions at the points where the cumulative density function of the Student′s t-distribution ceased to satisfy the Kolmogorov-Smirnov test. The test distinguished between the tails of the energy

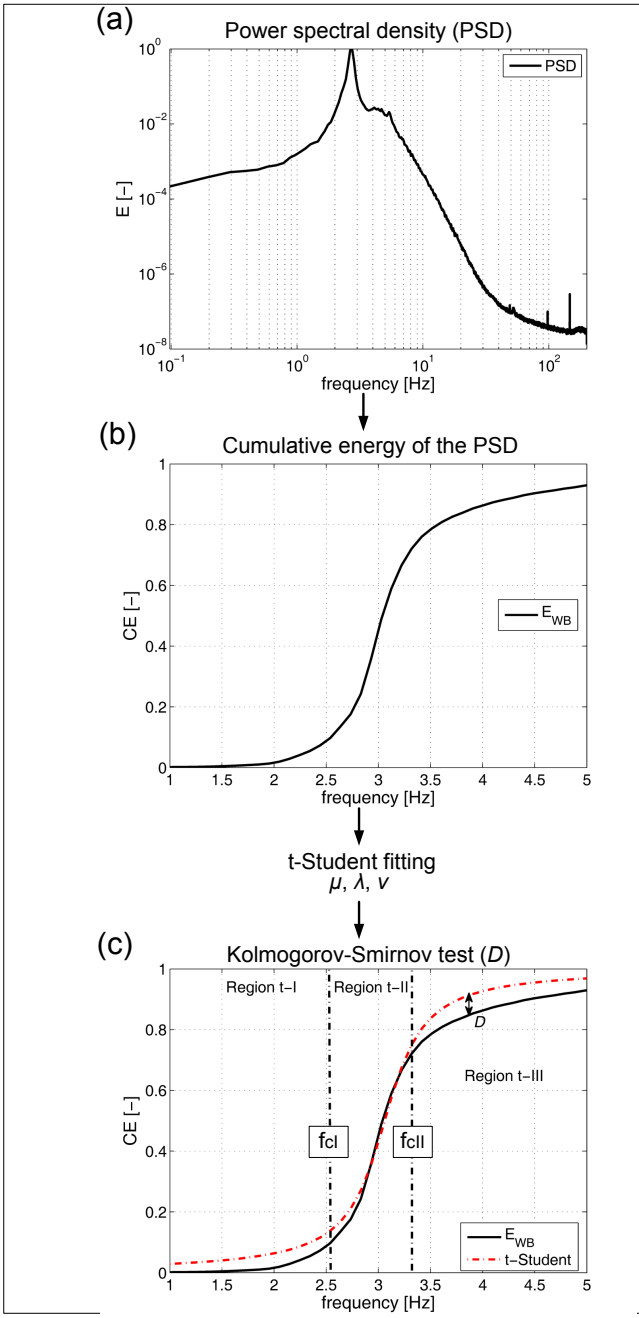

Figure 3.2: Scheme of the frequency division method.

distribution, which are not well-described by the Student′s t-distribution, and the central frequency region which is well-approximated by the statistical distribution, as shown in Figure 3.2-c for the example analyzed. The cut-off frequencies, f_{cI} and f_{cII}, divided the frequency domain into three frequency regions (Regions t-I, t-II and t-III). The significance level presented a low influence on the cut-off frequencies, and for that reason, a typical value of $\alpha = 5\%$ was used in the Kolmogorov-Smirnov tests (Stephens, 1970).

To follow the procedure stated above, it is necessary to set some criteria for the number of samples (N_s) needed for the computation of each sub-spectrum using the Welch′s method. The procedure consists of the initial estimation of the PSD using $N_s = 1024$ samples for the computation of each sub-spectrum. Then, the CE is approximated by the Student′s t-distribution CDF. The goodness of fit determines whether the frequency resolution is high enough to describe the characteristic frequencies of the system. If it is not achieved, the number of points considered is increased, and the procedure is restarted.

The effect of the number of samples on the standard error was investigated through examination of the data. The standard error of the power spectrum using $N_s = 4096$ was $\hat{\sigma_\nu} = 0.07$. If the number of samples was increased to $N_s = 8192$, the standard error decreased to $\hat{\sigma_\nu} = 0.049$. However, the decrease of the standard error caused a reduction of the frequency range where the Student′s t-distribution matched the cumulative energy distribution; consequently, the central region of coincidence between both distributions decreased drastically. This decrease changed the energy distribution, leading to a possible failure of the Kolmogorov-Smirnov test when identifying the corresponding cut-off frequencies.

3.6 Results

The statistical frequency division method based on the Student′s t-distribution approximation was applied to different measured pressure fluctuation signals collected either by Kistler or Honeywell pressure transducers. Several tests performed in the small bed facility ($d = 0.07$ m) varying the relative gas velocity ($1.8 < U_r < 3.78$) were analyzed to understand the operational limits of this method. The influence of the bed height on the Student′s t-distribution fit and the measurement conditions was studied for the fluidized bed equipped with a

rotating distributor ($D = 0.19$ m). Finally, water-induced defluidization tests are presented to illustrate the performance of the method as a monitoring tool.

3.6.1 Dynamic aspects of the frequency division method: the gas velocity effect

Tests were conducted in the small bed facility to study the influence of the gas velocity on the frequency domain division. The proposed statistical method and the visual approach were applied and compared for different fluidization velocities, ranging from $U_r = 1.9$ to 3.78 with a constant bed aspect ratio of $h_b/d = 1$.

The results of applying the statistical method to the pressure fluctuation signals are plotted in Figure 3.3. In this figure, the degree of matching between the experimental results and the Student′s t-distribution approach applied to both the power spectral density and the cumulative energy distribution are shown. Comparing these graphs, it can be appreciated that the determination of the goodness of fit between both distributions is easier using the cumulative energy distributions. The change in the fluidization regime was detected by both the power spectrum and the cumulative energy distribution. The results show that when the gas velocity was increased, a wider distribution of high energy frequencies was achieved, identifying the single bubble, multiple bubble and slug-like regimes (Figure 3.2-a1/b1/c1, respectively). The Student′s t-distribution CDF is close to the energy distribution in the range of frequencies where the sharp increase of energy appeared. This well-fitted Student′s t-distribution region defines Region t-II, between the cut-off frequencies of the low (f_{cI}) and high (f_{cII}) frequency regions. According to these frequency limits, the increase of the fluidization velocity produced a wider frequency range for Region t-II, covering most of the main characteristic frequencies shown in the spectrum, and therefore, showing a high sensitivity to bubbling dynamics. This result is a consequence of the wider range of frequencies with high energies, which can also be seen by comparing the $U_r = 1.9$ test (Figure 3.3-a2) and the $U_r = 2.84 - 3.78$ tests (Figure 3.3-b2/c2). Since the frequency boundaries of Region t-II are wider, the energy is mostly concentrated in Region t-II and the energies of Regions t-I and t-III are relatively small. The values of the energy contained in each frequency region can be found in Table 3.2.

The power spectra of the energy data for the three velocities are shown in logarithmic form in Figure 3.4. According to this figure, the increase in gas velocity influenced the total power of the PSD function but minimally influenced

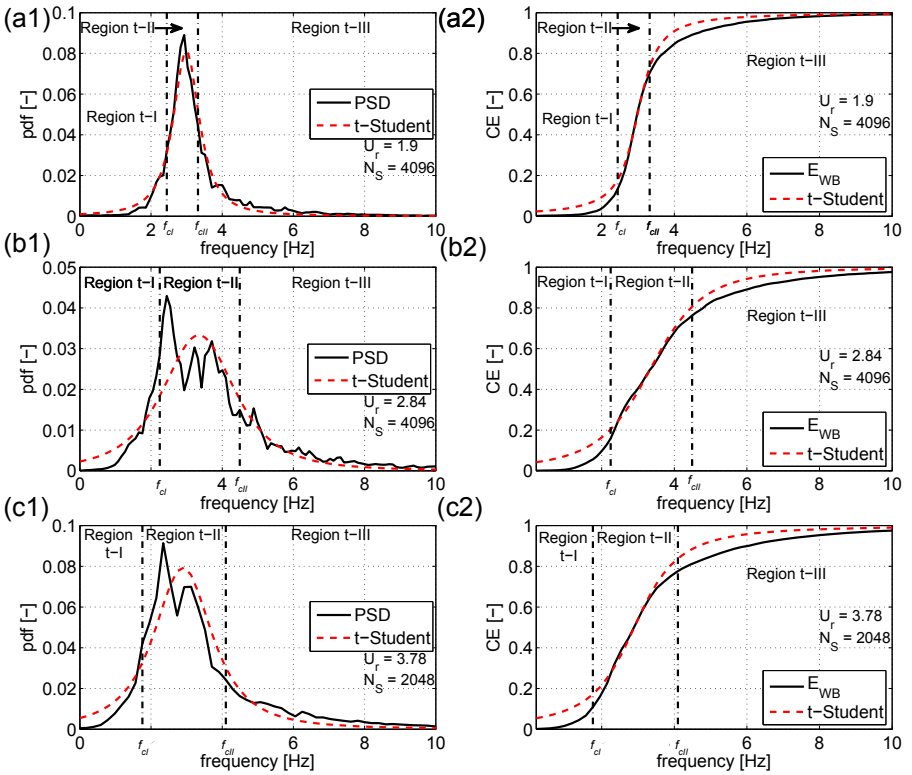

Figure 3.3: Probability mass function and cumulative mass function for different fluidization velocities ($d = 0.07$ m and $h_b/d = 1$): (a_1) PSD and (a_2) CE for $U_r = 1.9$, (b_1) PSD and (b_2) CE for $U_r = 2.84$, (c_1) PSD and (c_2) CE for $U_r = 3.78$.

its shape (van der Schaaf *et al.*, 2004). The logarithmic representation allowed the visual identification of the frequency limits. Thus, applying the visual division approach, Region 1 presents the cut-off frequency at $f_{cI} = 4$ Hz for $U_r = 1.9$ and $f_{cI} = 6$ Hz for $U_r = 2.84 - 3.78$ tests. However, as these frequency limits were visually chosen, other boundary values could be selected in the 3.7 - 7 Hz frequency range with similar accuracy because it is not clear where the power (or exponential) fall-off with frequency begins (Johnsson *et al.*, 2000). Similarly, it was difficult to find the upper frequency limit of Region 2 (f_{cII}). This frequency limit was fixed to $f_{cII} = 23$ Hz for the $U_r = 1.9$ and $f_{cII} = 30$ Hz for the $U_r = 2.84 - 3.78$ tests. The wide band energy values of the visual frequency regions were primarily found in Region 1. Those energy values were only slightly influenced by the lower frequency limit decrease, i.e. they merely increased because of the total power increase. In contrast, the energy of

Table 3.2: Effect of the velocity on the energy contained within the frequency regions of both methodologies.

	statistical approach			visual method		
U_r	Region t-I ($\Delta f < f < f_{cI}$)	Region t-II ($f_{cI} < f < f_{cII}$)	Region t-III ($f_{cII} < f < f_N$)	Region 1 ($\Delta f < f < f_{cI}$)	Region 2 ($f_{cI} < f < f_{cII}$)	Region 3 ($f_{cII} < f < f_N$)
1.90	10.10	60.33	29.57	83.22	16.68	0.10
2.84	13.04	63.23	23.73	88.80	11.12	0.08
3.78	6.65	70.97	22.38	89.45	10.22	0.33

Region 3 was almost negligible and independent of changes in the fluidization velocity.

The comparison of these results obtained with the Student′s t-distribution fitting and the visual inspection showed that both methods detected changes in the fluidization velocity. However, in addition to the difficulties in selecting the cut-off frequencies, Region 3 can be neglected because it is nearly independent of changes in the fluidization velocity. In contrast, the three Student′s t-distribution regions showed the effect of the gas velocity change.

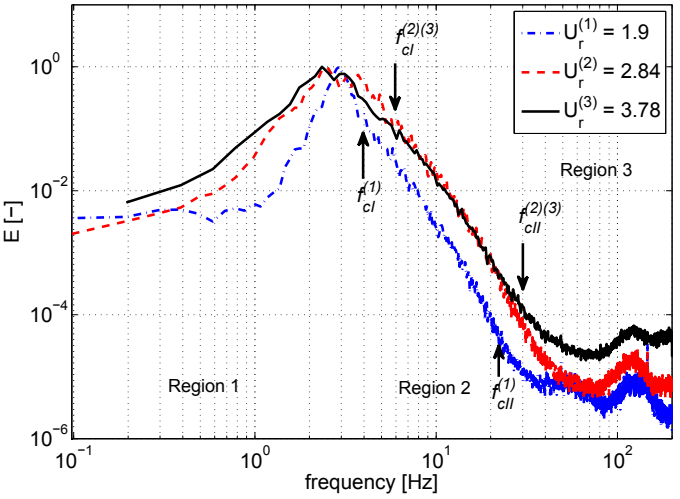

Figure 3.4: Power spectrum for different fluidization velocities (d = 0.07 m and h_b/d= 1).

3.6.2 Dynamic aspects of the frequency division method: the bed aspect ratio effect

It has been previously reported in the literature (Kage *et al.*, 2000; van der Schaaf *et al.*, 2004) that increasing the fixed bed height at a constant gas velocity produces a decrease of the dominant frequency, while the power fall-off with frequency remains unaffected. This behavior was used to analyze both the sensitivity and reliability of the Student′s t-distribution frequency division approach. The reliability was assessed by studying whether the proposed methodology can be applied using the plenum and bed Kistler pressure signals to: (i) divide the frequency domain, and (ii) detect changes in the bed aspect ratio. Then, the results obtained with the Student′s t-distribution methodology were compared with the visual frequency division approach. To that end, tests were performed by changing the fixed bed height, using values of $h_b/D = 0.75$, 1.5 and 2 at a constant air velocity ratio, $U_r = 1.6$, in the larger fluidized bed with a static distributor.

The power spectra density functions and the cumulative energy distributions are shown in Figure 3.5 for both pressure sensors. The results of the statistical methodology, i.e. the Student′s t-distribution fitting and cut-off frequencies, are also plotted with the cumulative energy distributions (Figure 3.5-a2/b2). Similar power spectra and cumulative energy distributions were found for both pressure probes, as stated in Chaper 2. Focusing on the pressure measurements in the plenum chamber presented in Figure 3.5-a1/a2, the transition from shallow to deeper beds was shown by a decrease of the dominant frequencies and by the appearance of secondary frequency peaks.

The power spectra of Figure 3.5-a1 show that the dominant frequencies decrease from $f_c = 2.7$ Hz for the shallow bed to $f_c = 1.85$ and 1.41 Hz for $h_b/D = 1.5$ and 2, respectively. These characteristic frequencies are in accordance with those calculated with the equations proposed by Baskakov *et al.* (1986). The bed aspect ratio increase produced the appearance of some secondary peaks at approximately 2-4 Hz in the cases of $h_b/D = 1.5$ and 2, illustrating the slug regime for the deepest bed. The bed height variations can also be detected using the cumulative energy distributions by the displacement of the abrupt energy increase to lower frequencies, as can be observed in Figure 3.5-a2. The secondary peaks shown in the PSD shown in Figure 3.5-a1 were also detected by the cumulative energy distribution (Figure 3.5-a2) as a change in the slope at approximately 2-4 Hz. These secondary peaks shown in both the PSD and CE suggest the use of a bimodal distribution to describe the two

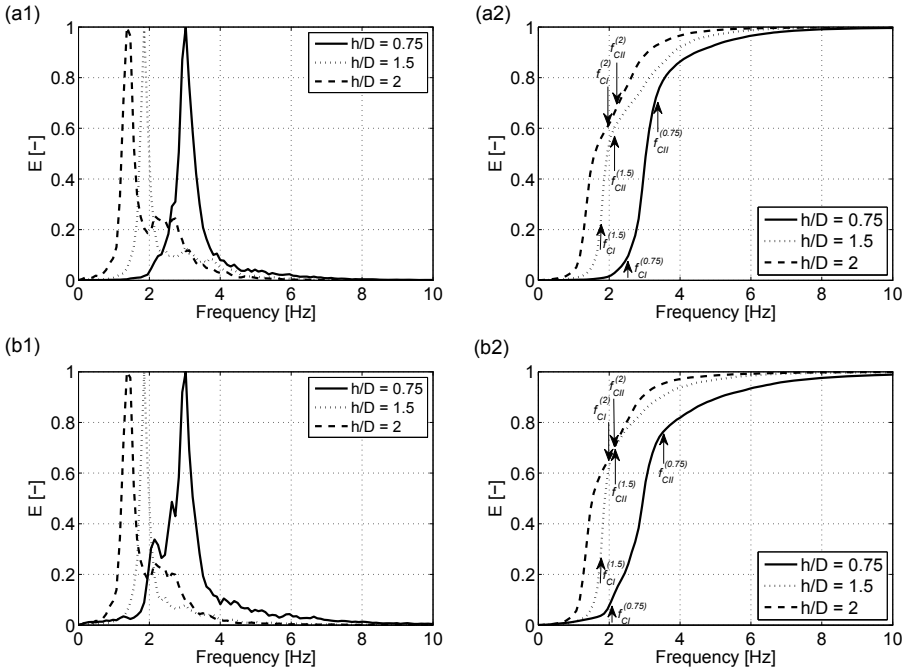

Figure 3.5: The PSD and CE functions of a time series pressure signal varying bed heights ($D = 0.19$ m and $U_r = 1.6$). (a1) PSD of the plenum sensor, (a2) CE of the plenum sensor, (b1) PSD of the bed sensor, (b2) CE of the bed sensor.

modes shown in Figure 3.5-a1 for the $h_b/D = 2$ test. This result indicates that the statistical distribution that fits the frequency domain depends on the experimental conditions. Nevertheless, the Student′s t-distribution fitting of the $h_b/D = 2$ test also offered valuable results, and for this reason, only the approximation of that statistic distribution to the experimental results will be considered in this work. Similar results were obtained for the cut-off frequencies and energy content of the frequency regions using the pressure probe inside the bed, considering each aspect ratio separately. The results are shown in Table 3.3. Only slight differences between the frequency limits of the plenum and bed pressure probe for the $h_b/D = 0.75$ case were shown. Thus, as these differences are negligible, the discussion will be focused on the analysis of the pressure signals recorded at the plenum chamber.

Comparing the energy values of the beds with different bed aspect ratios, the results show that the energy contained in each region varies with the bed height change, as shown in Table 3.3. The frequency peaks obtained at higher

Table 3.3: Frequency division results from the Student′s t-distribution approach for the bed equipped with a rotating distributor for different bed heights, Kistler sensors ($D = 0.19$ m and $U_r = 1.6$).

h_b/D	pressure location	cut-off frequencies [Hz]		mean energy content [%]		
		f_{cI}	f_{cII}	Region t-I ($\Delta f < f < f_{cI}$)	Region t-II ($f_{cI} < f < f_{cII}$)	Region t-III ($f_{cII} < f < f_N$)
0.75	plenum	2.54	3.32	7.35	58.32	34.33
	h=7 cm	2.05	3.51	9.00	65.66	25.34
1.5	plenum	1.76	2.15	30.33	22.87	48.80
	h=7 cm	1.76	2.15	35.78	26.01	38.20
2	plenum	1.95	2.25	56.58	8.91	34.51
	h=7 cm	1.95	2.15	58.71	5.64	35.65

frequencies than the dominant frequency of deep beds changed the slope of the cumulative energy distribution; thus, the region of approximation between the Student′s t-distribution and the cumulative energy distribution was different. Therefore, as the frequency limits change, the dynamic features and the physical meanings attributed to the different frequency regions also change with the bed aspect ratio. Similar to the results obtained from Figure 3.4, for $h_b/D = 0.75$ and Figure 3.5 for $h_b/D = 1.5$, Region t-II is related to the bulk dynamics because it contains the dominant frequency of the bed, whereas Regions t-I and t-III represent the slow and the fast fluidization phenomena, respectively. However, the energy increase of the secondary frequency peaks shown in Figure 3.5-a2 for the deepest bed ($h_b/D = 2$) caused the Student′s t-distribution proper fit (which is not included in the figure for clarity reasons) to the cumulative energy distribution at higher frequencies, focusing Region t-II on the secondary peaks shown in the PSD (Figure 3.5-a1). Therefore, Region t-I includes in this case the main frequency of the bed, whereas Region t-II identifies the slug-like regime and Region t-III the fast fluidization phenomena. Hence, as the bed height is increased, the energy of Region t-II diminishes, transferring a large portion of its energy to Region t-I, whereas the energy contained in the high frequency region (Region t-III) remains nearly constant.

Once the capability of the Student′s t-distribution methodology to detect changes in the bed aspect ratio was verified, its performance was studied by comparing the results with the visual frequency division method. As stated by vander Stappen (1996); van der Schaaf *et al.* (1999); Johnsson *et al.* (2000), the cut-off frequencies were visually fixed according to the changes in the power fall-off with frequency. The frequency limits and the energy contained in each

Table 3.4: Frequency division results from the visual inspection method for the bed equipped with a rotating distributor for different bed heights, Kistler sensor placed at the plenum ($D = 0.19$ m and $U_r = 1.6$).

	cut-off frequencies [Hz]		mean energy content [%]		
h_b/D	f_{cI}	f_{cII}	Region 1 ($\Delta f < f < f_{cI}$)	Region 2 ($f_{cI} < f < f_{cII}$)	Region 3 ($f_{cII} < f < f_N$)
0.75	5	25	89.3	10.67	0.03
1.5	4	20	91.11	8.88	0.01
2	3	20	85.91	14.08	0.01

region is shown in Table 3.4. These results show that the frequency limits of Regions 1 and 2 (f_{cI}) decreased as the bed height was increased, because the major frequency content of the pressure fluctuations moved to lower frequencies (Kage *et al.*, 2000). This frequency decrease was not found for the cut-off frequencies in Regions 2 and 3 (f_{cII}). The energy computation within these frequency regions confirms that Region 3 is influenced neither by the fluidization nor by the bed height increase. The energy of all frequency regions remains nearly constant with the bed height increase, because Region 1 always contains nearly 90% of the spectral energy. Therefore, regardless of the successful previous application of the visual inspection method for the characterization of the power spectrum (vander Stappen, 1996; van der Schaaf *et al.*, 1999; Johnsson *et al.*, 2000), the corresponding wide band energy distribution detected a negligible effect of the bed aspect ratio. Consequently, the subsequent monitoring performance would be less sensitive than that obtained by the wide band energy measured using the Student′s t-distribution approach. As shown in Table 3.3, the proposed Student′s t-distribution approach is capable of detecting the bed height variations.

3.6.3 Pressure sensors rating effect

One of the primary drawbacks of the visual frequency division method is the bias caused by the observer when selecting the frequency limits. The measured pressure signal can be affected by noise, which hinders the detailed description of the high frequency spectral region. Moreover, pressure sensor rating and signal conditioning can affect the signal quality and therefore, the frequency limit identification. For instance, the power spectrum fall-off, which is critical for using the visual inspection method, can be significantly different if an industrial or laboratory pressure sensor is used.

Therefore, the possible effect of the pressure sensor rating for both the visual and unbiased Student′s t-distribution approaches was investigated. Pressure fluctuations recorded at the plenum chamber with both the Kistler and the Honeywell transducers were analyzed using both methods. The experimental runs were conducted in the 19 cm inner diameter fluidized bed facility operating with the static distributor at $U_r = 1.6$ for 4 min. The Honeywell transducers, similar to those used in industrial applications, are characterized by a high level of noise in the raw pressure fluctuation signal; thus, the signal must be filtered. The spurious crossings in the raw Honeywell data produced aliasing problems leading to incorrect power spectrum estimation at high frequencies. Honeywell pressure-time signals were filtered using a moving average filter. A finite impulse filter (FIR) attenuates the high frequencies while retaining a sharp step response. The averaging window length of the filter was set according to the average cycle time of the unfiltered pressure signal (vander Stappen, 1996). In contrast to the Honeywell measurements, the high quality of the Kistler pressure signals ensured correct power spectrum estimation from the raw pressure data.

Figure 3.6 shows the frequency regions obtained from the Kistler and Honeywell pressure signals using both methods. The corresponding power spectra (Figure 3.6-a1/b1) and cumulative energy distributions (Figure 3.6-a2/b2) were estimated for the measured Kistler signals (raw data) and for the filtered Honeywell data. The results from the visual inspection method (Region 1, 2 and 3) are presented in Figure 3.6-a1/a2, and the Student′s t-distribution frequency regions (Region t-I, t-II and t-III) are shown in Figure 3.6-b1/b2.

The visual frequency division starts with the power spectrum estimation and the evaluation of the power decay with frequency. The results for the Kistler PSD (Figure 3.6-a1) show a sharp frequency peak at $f_c = 2.734$ Hz in the power spectrum, which is followed by two different power fall-off regions with frequency that can be fitted with similar accuracy either to exponential, $P_{xx} \sim \exp(-f/\mu)$, or power functions, $P_{xx} \sim f^{-\alpha}$ (van der Schaaf *et al.*, 1999; Johnsson *et al.*, 2000). The visual inspection of Figure 3.6-a1 suggests that the frequency domain can be divided into three regions because the power fall-off with frequency changes at approximately 3 to 6 Hz and 20 to 30 Hz. The cut-off frequency between Regions 1 and 2 was located at $f_{cI} = 5$ Hz, and the frequency limit between Regions 2 and 3 is visually selected to be $f_{cII} = 25$ Hz. Similar results are shown for the Honeywell pressure signal up to $f_{cII} = 25$ Hz. At 25 Hz, the Honeywell power spectrum shows a high level of noise, which prevents the development of the power-law fitting of Region 3 and the rigorous

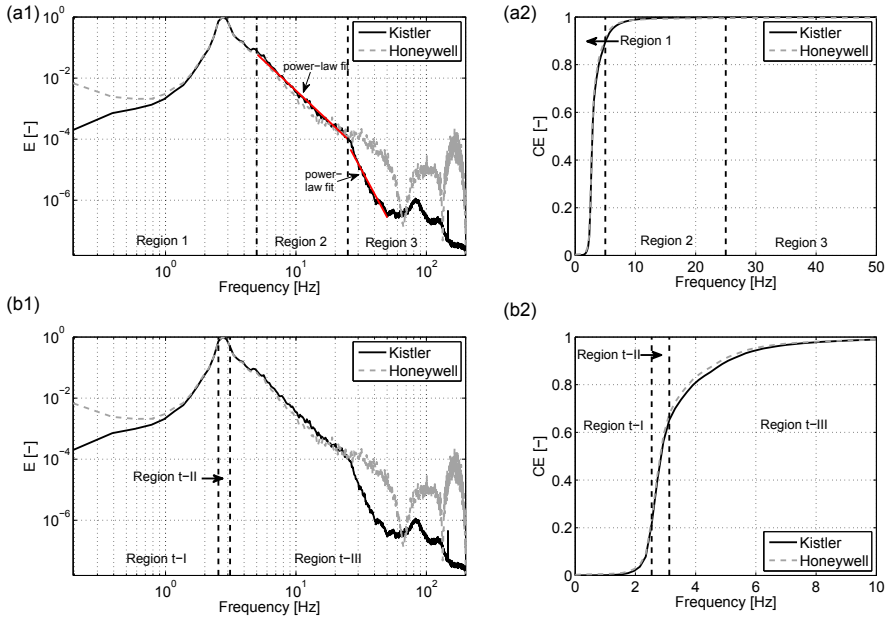

Figure 3.6: Frequency regions from the PSD of the Kistler and Honeywell pressure sensors located at the plenum ($N_s = 2048$, $D = 0.19$ m, $h_b/D = 0.75$ and $U_r = 1.6$): (a1) power spectra and (a2) cumulative energy distributions of the visual inspection approach, (b1) power spectra and (b2) cumulative energy distributions of the Student′s t-distribution approach.

application of the visual inspection method.

In spite of the differences at the higher frequencies of the spectra (Region 3), both the Kistler and Honeywell spectral domains can be visually divided with the same frequency limits; consequently, the frequency regions represent identical fluidization processes. These frequency regions are also plotted in energy terms with the cumulative energy distributions for both pressure sensors in Figure 3.6-a2. The results in this figure show no significant differences between the two cumulative energy distributions because most of the characteristic frequencies of the bed are contained in Region 1 and Region 2, where the signal noise is negligible. Regarding the spectral regions resulting from the Student′s t-distribution approach, no meaningful differences can be observed either in the PSD (Figure 3.6-b1) or in the cumulative energy distribution (Figure 3.6-b2) between the Kistler and Honeywell data. Therefore, from the point of view of the pressure sensor rating, both the visual inspection method and the Student′s t-distribution approach are unaffected since the influence of the

noise is restricted to Region t-III.

However, the sizes of the resulting regions were different depending on the method used to find the boundaries of the three regions. Therefore, the characteristic frequencies were likely to produce a different sensitivity in the wide-band energy calculated from the visual inspection and the Student′s t-distribution methods. Their dynamic responses were compared, to understand the response of the wide band energy to dynamic changes in the fluidized bed.

Concerning the visual inspection method, Region 1 represents the macro-structure of the flow because it contains most of the characteristic frequencies of the bed dynamics (van der Schaaf *et al.*, 1999; Johnsson *et al.*, 2000). However, only limited information about the nature of the macro-structure dynamics in the fluidized bed has been reported in the literature. Therefore, it is difficult to assign relative weights to the different bed dynamic scales in Region 1 for the fluidization conditions caused by the multiscale features of the bed dynamics. Nevertheless, the description serves to explain the wide band energy behavior from a monitoring point of view. As a result of the presence of high power frequency peaks within Region 1 (Figure 3.6-a1), 89% of the spectral energy is concentrated in that region. Region 2 represents nearly 10% of the spectral energy and includes the inflection points that appeared in the cumulative energy distributions as a result of the abrupt energy change following the dominant frequency. Typically, Region 2 has been related to the finer structures of the bed (fast dynamic processes) (van der Schaaf *et al.*, 1999; Johnsson *et al.*, 2000). Finally, the high frequency region involves less than 1% of the energy, proving that Region 3 has no clear dependence on the fluidization regime (Johnsson *et al.*, 2000; Briongos & Soler, 2003).

Different frequency regions were obtained applying the Student′s t-distribution approach, illustrated by comparing Figure 3.6-a1/a2 and Figure 3.6-b1/b2. The proposed statistical method disregards the previous physical interpretation of the spectrum and centers the division of the frequency domain on the mean frequency value. According to this approach, the region of coincidence between the Student′s t-distribution and the cumulative energy distribution defines Region t-II. Figure 3.6-b2 shows the results of applying this method to the cumulative energy distributions obtained with the Kistler and Honeywell sensors. The frequency limits were found to be at $f_{cI} = 2.5$ Hz and $f_{cII} = 3.1$ Hz dividing the frequency domain into the lower (Region t-I) and upper (Region t-III) tails of the cumulative energy distribution that were a worse approximation of the data by the Student′s t-distribution function. As shown in Figure 3.6-b1, for this

case, the frequency limits divided the frequency spectra around the dominant frequency of the bed. The energy is primarily focused in Region t-II (around 59%), whereas 7% and 34% of the energy are distributed in Regions t-I and t-III, respectively. Because of the difference in the cut-off frequencies and in the region size, the energy values and the dynamic processes related to each region are also different. Nevertheless, similar to the visual inspection method, the physical phenomena that characterize the spectra of Figure 3.6-b1/b2, which correspond to the Student′s t-distribution approach, can be identified in terms of the time scale dynamics as follows:

- Region t-I ($\Delta f < f < 2.5$ Hz) represents the larger structures of the bed which govern the low frequency dynamics and consequently drive the long-term dynamics of the bed.

- Region t-II (2.5 Hz $< f <$ 3.1 Hz) contains the dominant/mean frequency of the bed, suggesting that it is related to the bulk dynamics of the bed.

- Region t-III (3.1 Hz $< f < f_N$) includes the high frequency region of the spectrum and is related to the fast fluidization phenomena.

The results showed in Figure 3.6 prove that the different energy contents resulting from the visual inspection and Student′s t-distribution method are caused by different distributions of the characteristic frequencies. In the case of the visual frequency division, there is a region that contains almost all the characteristic frequencies (Region 1) and high frequency regions that represent the fast fluidization phenomena (Region 2 and 3). However, for the Student′s t-distribution approach, the location of the cut-off frequencies around the dominant frequency allowed the division of the macro-structure of the flow, and consequently, the division of the previous Region 1 into several sections. This division can be illustrated by comparing the frequency limits of Region 1 ($\Delta f < f <$ 5 Hz), Region 2 (5 Hz $< f <$ 25 Hz) and Region 3 (25 Hz $< f < f_N$), with the cut-off frequencies of Regions t-I ($\Delta f < f <$ 2.5 Hz), t-II (2.5 Hz $< f <$ 3.1 Hz) and Region t-III (3.1 Hz $< f < f_N$). Due to that, the Student′s t-distribution approach of the bed frequencies provides a higher sensitivity of the wide band energy parameter for describing bubbling dynamics.

3.6.4 Application to detection of the defluidization phenomena

Water-induced agglomeration tests were performed to illustrate the use of the wide band energy as a monitoring tool. These tests were conducted to reduce the fluidization quality through the defluidization of the bed and the subsequent recuperation processes, as shown in Chapter 2. Thus, the wide band energy was estimated using the frequency regions obtained with the Student′s t-distribution and visual inspection methods. The cut-off frequencies were previously detailed in Figure 3.6-b1/b2, for the Student′s t-distribution, and in Figure 3.6-a1/a2, for the visual method. The wide band energy for the pressure signals was estimated every 50 s throughout the entire test.

The agglomeration tests were conducted in the fluidized bed equipped with a rotating distributor (D = 0.19 m) analyzing the Kistler signals recorded at the plenum chamber. The runs started with the bed working at $U_r = 1.6$ and $h_b/D = 0.75$ using the static distributor; these conditions are referred to as nominal conditions. After 6 min, 150 ml of water was injected onto the bed surface, causing the defluidization of the bed. Then, two different attempts to recover the fluidization quality were performed: (i) with the static distributor and (ii) with the rotating distributor.

The wide band energy values obtained using the Student′s t-distribution frequency regions are shown in Figure 3.7. The water injection and the start of the distributor rotation are pointed by an arrow in this figure. The three control charts shown in this figure correspond to the three frequency regions into which the frequency domain was divided. On each chart, the wide band energy values are shown with a black curve for the rotating distributor, and with a gray curve for the static distributor recuperation. The mean value of the wide band energy at nominal conditions is shown as a reference value.

The water injection formed sticky agglomerates on the bed surface that tended to settle over the distributor. This growth of dead zones over the distributor caused the defluidization of the bed and the appearance of channels near the injection zone, which modified the air distribution in the bed. This bed defluidization was detected by the wide band energy of Regions t-II and t-III, which can be observed in Figure 3.7-a/b. As shown in Figure 3.7, the punctual injection of water produced a substantial energy transfer of 20% from Region t-II (Figure 3.7-b) to the higher frequencies in Region t-III (Figure 3.7-a), caused by the appearance of channels around the injection zone. This energy transfer to the higher frequencies confirms that Region t-III is related to the fast flu-

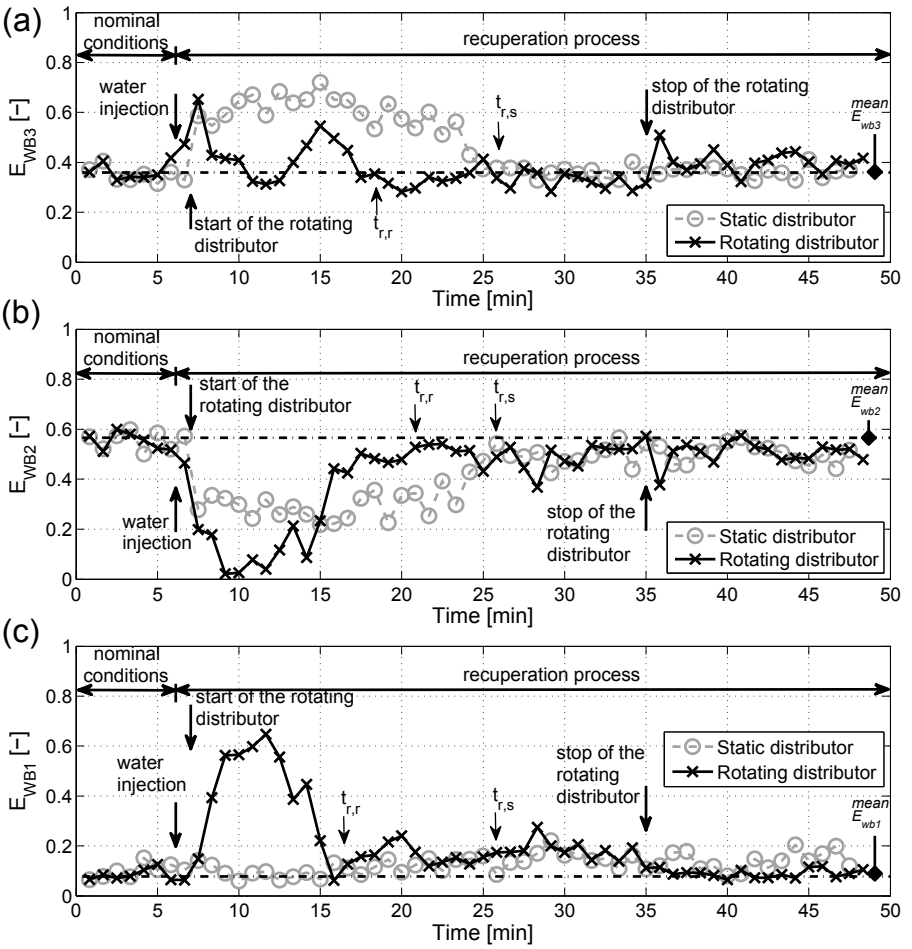

Figure 3.7: Wide band energy measured in the Student′s t-distribution regions for the Kistler sensor. (a) Region t-III (3.12 Hz $< f <$ f_N). (b) Region t-II (2.54 Hz $< f <$ 3.12 Hz). (c) Region t-I ($\Delta f < f <$ 2.54 Hz).

idization phenomena. Furthermore, the energy loss in Region t-II indicates that the bulk motion of the bed was hindered by the agglomerates formation, suggesting the defluidization of the bed. On the other hand, the energy of Region t-I is not affected by the water injection, as shown during the static distributor recuperation process in Figure 3.7-c, suggesting that the larger structures of the flow field, such as the bubble pattern, remain unaffected during the agglomerates formation. Visual observation of the tests showed that the agglomerates were not homogeneously distributed within the bed, allowing the presence of a bubbling zone opposite to the injection zone. This phenomenon explains why

the wide-band energy of Region t-I was not affected by the water injection: a bubbling zone was maintained within the bed and preserved the long term behavior of the pressure measurements.

The recuperation process with the static distributor was only affected by the air flow; consequently, the agglomerates breakage was a slow phenomenon, requiring $t_{r,s} = 19$ min to return to the nominal conditions, as shown for Regions t-II and t-III in Figure 3.7-a/b. Because of the slow rate of agglomerates destruction, there were channels during most of the recuperation process with the static distributor. Nevertheless, the rotating distributor reached nominal conditions for the mean wide band energy values $t_{r,r} = 10$ min after the water injection. The beginning of the distributor rotation produced an effect on the entire frequency domain, according to the Student′s t-distribution frequency regions (Figure 3.7). The homogeneous bubble distribution caused by the distributor rotation at 100 rpm imposed a local structure on the bed dynamics, as proved in Chapter 2. Moreover, the rotating effect broke the dead zones between holes of the distributor, where the agglomerates were settled, and thus improved the channel destruction. The data for Region t-III in Figure 3.7-a show that 1 min after the beginning of the distributor rotation, almost all the channels had disappeared. This effect was detected immediately after switching on the distribution rotation, when the three energy regions suddenly changed their energy values, transferring almost 30% of the energy from Region t-III to Region t-I, as shown in Figure 3.7-a/c. However, the agglomerates detached from the water injection zone were distributed throughout the fluidized bed as a consequence of the distributor rotation, reducing the fluidization quality for a short time. That process was reflected by the energy transfer from Region t-II to Region t-I showed in Figure 3.7-b/c, pointing out that there was a change in the bed structure after the start of the distributor rotation.

Figure 3.8 shows the wide band energy results using the visual frequency regions. As stated above, the frequency regions obtained with the visual approach are related to different phenomena than the Student′s t-distribution regions. In the case of the visual inspection method, Region 1 contains all the high frequency peaks and it is related to the macro-structure of the flow, whereas Regions 2 and 3 represent the finer structures. Therefore, the wide band energy of these frequency regions shown in Figure 3.8 proves that the energy is primarily focused in Regions 1 ($E_{WB1} = 90\%$) and 2 ($E_{WB2} = 10\%$), whereas the energy value of Region 3 is negligible in comparison to the Student′s t-distribution results shown in Figure 3.7. The data shown in Figure 3.8-b/c

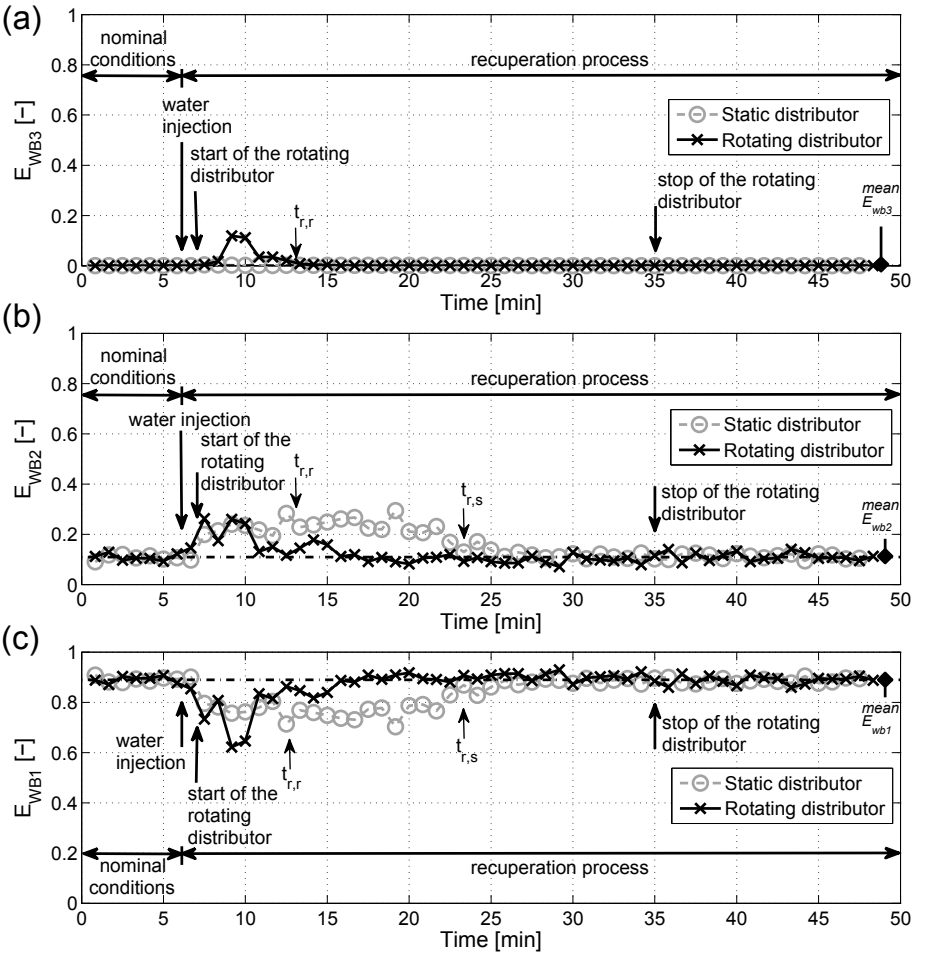

Figure 3.8: Wide band energy measured in the visual frequency regions for the Kistler sensor. (a) Region 3 (25 Hz $< f < f_N$). (b) Region 2 (5 Hz $< f <$ 25 Hz). (c) Region 1 ($\Delta f < f <$ 5 Hz).

show that the water injection is detected by a 10% energy transference from Region 1 to Region 2. The energy increase of the high frequencies (Region 2) highlights the channel formation. However, Region 3 is barely affected by the water injection, as can be observed in Figure 3.8-a. In spite of that, according to Regions 1 and 2 (Figure 3.8-b/c), $t_{r,s} = 19$ min were needed to recover the fluidization quality with the static distributor test, which is close to the time obtained by the Student′s t-distribution frequency regions (Figure 3.8).

The effect of starting the distributor rotation was shown by the energy transferred from the higher (Region 2) to the lower (Region 1) frequencies due

to the destruction of the channels (Figure 3.8-b/c). Figure 3.8 shows that the rotation of the distributor needed just $t_{r,r} = 5$ min to recover the fluidization state and return the bed to the nominal conditions. Nevertheless, the visual inspection during the test and the previous results shown in Figure 3.7 stated that the recuperation process required at least $t_{r,r} = 10$ min to recover the initial fluidization quality. The false alarm can be explained by the wide frequency limits of Region 1, since Region 1 contains all the frequencies up to $f_{cI} = 4$ Hz. Thus, the energy increase produced by the beginning of the rotating distributor shown in Region t-I ($\Delta f < f < 2.54$ Hz) directly supports the wide band energy of Region 1 ($\Delta f < f < 4$ Hz). The appearance of a false alarm proves that the frequency limits of Region 1 are too wide to discriminate between the larger structures and the macro-structure of the flow field. Therefore, in spite of the detection of the channel destruction from the start of the distributor rotation shown in Region 2 (Figure 3.8-b), the frequency regions obtained through the visual approach were not able to detect the defluidization problems associated to the agglomerates formation in the bed.

3.7 Conclusions

A methodology for the unbiased and systematical frequency domain division using the Student′s t-distribution approximation of the cumulative energy distribution is proposed. The method improves the sensitivity of the traditional wide band energy analysis by visual inspection. The reliability of the method to divide the frequency domain was shown for different fluidization velocities, changing the bed aspect ratio and using different pressure probes.

The comparison between the visual frequency division approach and the proposed methodology showed significant differences in the cut-off frequencies. The estimated wide band energy in the frequency regions obtained using the visual method was not able to detect changes in the bed aspect ratio or the beginning of the rotating distributor. Nevertheless, the sensitivity shown by the statistical frequency division approach would enable wide band energy to be used as a diagnostic tool in fluidized bed processes.

The application of the proposed methodology showed that the frequency limits vary as a function of the fluidization conditions. The fluidization conditions can also change the physical meaning of the frequency regions. The description of the physical meaning can be related to the time scales, and thus the different fluidization phenomena can be related to the wide band energy

regions. This feature showed the capability of unbiased frequency regions to be used as a monitoring tool for water-induced defluidization tests, allowing the detection of some dynamic phenomena, such as channel formation, defluidization of the bed, or the beginning of the distributor rotation.

Notation

d	Inner diameter of small fluidized bed vessel [m]
D	Inner diameter of big fluidized bed vessel [m]
D_n	Distance between cumulative distributions [-]
D^*	Modified statistic of the Kolmogorov-Smirnov test
E	Normalized energy [-]
E_{WB}	Wide band energy [-]
f	Frequency [Hz]
f_c	Central frequency [Hz]
f_{cI}	Lower cut-off frequency [Hz]
f_{cII}	Upper cut-off frequency [Hz]
f_N	Nyquist frequency [Hz]
h_b	Fixed bed height [m]
H_0	Null hypothesis
H_1	Alternative hypothesis
K_α	Kolmogorov threshold value
n	Sample size [-]
N_s	Number of samples [-]
$P(x)$	Probability of x [-]
P_{xx}	Power of the spectrum [Pa^2/Hz]
$S_n(x)$	Empirical cumulative distribution of x [-]
t_r	Recuperation time [s]
U	Gas velocity [m/s]
U_r	Relative gas velocity [-]
$U_{mf,r}$	Minimum fluidization velocity with rotating distributor [m/s]
$U_{mf,s}$	Minimum fluidization velocity with static distributor [m/s]

Greek symbols

α	Significance level [-]
Δf	Frequency resolution [Hz]

λ	Scale parameter
μ	Location parameter
ν	Shape parameter
$\hat{\sigma}$	Standard error

Abbreviattions

CDF	Cumulative density function
CE	Cumulative energy
MLE	Maximum-Likelihood estimation method
pdf	Probability density function
PSD	Power spectra density

References

Baskakov, A. P., Tuponogov, V. G. & Filippovsky, N. F. 1986 A study of pressure-fluctuations in a bubbling fluidized-bed. *Powder Technology* 45 (2), 113–117.

Briongos, J. Villa & Soler, J. G. 2003 Free top fluidized bed surface fluctuations as a source of hydrodynamic data. *Powder Technology* 134 (1-2), 133–144.

Brown, R. C. & Brue, E. 2001 Resolving dynamical features of fluidized beds from pressure fluctuations. *Powder Technology* 119 (2-3), 68–80.

Chilekar, V. P., Warnier, M. J. F., van der Schaaf, J., Kuster, B. F. M., Schouten, J. C. & van Ommen, J. R. 2005 Bubble size estimation in slurry bubble columns from pressure fluctuations. *AIChE Journal* 51 (7), 1924–1937.

Dempster, A.P. 1977 Maximum likelihood from incomplete data via em algorithm. *Journal of the Royal Statistical Society.Series B, Methodological* 39 (1), 1–38.

Fisher, R. A. 1925 Theory of statistical estimation. *Mathematical Proceedings of the Cambridge Philosophical Society* 22 (05), 700.

Geldart, D. 1973 Types of gas fluidization. *Powder Technology* 7 (5), 285–292.

Gómez-Hernández, J., Soria-Verdugo, A., Briongos, J. Villa & Santana, D. 2012 Fluidized bed with a rotating distributor operated under defluidization conditions. *Chemical Engineering Journal* 195-196 (0), 198–207.

Johnsson, F., Zijerveld, R. C., Schouten, J. C., van den Bleek, C. M. & Leckner, B. 2000 Characterization of fluidization regimes by time-series analysis of pressure fluctuations. *International Journal of Multiphase Flow* 26 (4), 663–715.

Kage, H., Agari, M., Ogura, H. & Matsuno, Y. 2000 Frequency analysis of pressure fluctuation in fluidized bed plenum and its confidence limit for detection of various modes of fluidization. *Advanced Powder Technology* 11 (4), 459–475.

de Martin, L., van den Dries, K. & van Ommen, J. R. 2011 Comparison of three different methodologies of pressure signal processing to monitor fluidized-bed dryers/granulators. *Chemical Engineering Journal* 172 (1).

van Ommen, J. R., Sasic, S., van der Schaaf, J., Gheorghiu, S., Johnsson, F. & Coppens, M. O. 2011 Time-series analysis of pressure fluctuations in gas-solid fluidized beds - a review. *International Journal of Multiphase Flow* 37 (5), 403–428.

van Ommen, J. R., Schouten, J. C., vander Stappen, M. L. M. & van den Bleek, C. M. 1999 Response characteristics of probe-transducer systems for pressure measurements in gas-solid fluidized beds: how to prevent pitfalls in dynamic pressure measurements. *Powder Technology* 106 (3), 199–218.

Parise, M. R., Silva, C. A. M., Ramazini, M. J. & Taranto, O. P. 2011 Identification of defluidization in fluidized bed coating using the gaussian spectral pressure distribution. *Powder Technology* 206 (1-2), 149–153.

Ruthiya, K. C., Chilekar, V. P., Warnier, M. J. F., van der Schaaf, J., Kuster, B. F. M., Schouten, J. C. & van Ommen, J. R. 2005 Detecting regime transitions in slurry bubble columns using pressure time series. *AIChE Journal* 51 (7), 1951–1965.

van der Schaaf, J., Johnsson, F., Schouten, J. C. & van den Bleek, C. M. 1999 Fourier analysis of nonlinear pressure fluctuations in gas-solids flow in cfb risers - observing solids structures and gas/particle turbulence. *Chemical Engineering Science* 54 (22), 5541–5546.

van der Schaaf, J., van Ommen, J. R., Takens, F., Schouten, J. C. & van den Bleek, C. M. 2004 Similarity between chaos analysis and frequency analysis of pressure fluctuations in fluidized beds. *Chemical Engineering Science* 59 (8-9), 1829–1840.

van der Schaaf, J., Schouten, J. C. & van den Bleek, C. M. 1998 Origin, propagation and attenuation of pressure waves in gas-solid fluidized beds. *Powder Technology* 95 (3), 220–233.

van der Schaaf, J., Schouten, J. C., Johnsson, F. & van den Bleek, C. M. 2002 Non-intrusive determination of bubble and slug length scales in fluidized beds by decomposition of the power spectral density of pressure time series. *International Journal of Multiphase Flow* 28 (5), 865–880.

Sobrino, C., Almendros-Ibanez, J. A., Santana, D. & Vega, M. De 2008 Fluidization of group b particles with a rotating distributor. *Powder Technology* 181 (3), 273–280.

vander Stappen, M. L. M. 1996 Chaotic hydrodynamics of fluidized beds.

Stephens, M. A. 1970 Use of komogorov-smirnov,cramer-von mises and related statistics without extensive tables. *Journal of the Royal Statistical Society Series B-Statistical Methodology* 32 (1), 115–&.

Welch, P. 1967 The use of fast fourier transform for the estimation of power spectra: a method based on time averaging over short, modified periodograms. *IEEE Transactions on Audio and Electroacoustics* 15 (2), 70.

CHAPTER
FOUR

Statistical Process Control of fluidized beds: Application to paste drying process

Contents

4.1 Abstract

A novel approach based on the Statistical Process Control theory is proposed to design a continuous control scheme for fluidized bed processes. The proposed method provides the properties of the moving mean control charts, such as the window size and the samples distribution, to study the processes. The optimal conditions found for the control chart development are the window sizes of 25 s,

35 s and 50 s, for the standard deviation, average cycle time and frequency domain respectively, and the use of the normal distribution to determine the control limits. In order to illustrate the use of the methodology, paste drying tests with sand particles as inert medium were carried out. The control scheme applied to the time and frequency domains analyses of the pressure fluctuations series, which were recorded during the drying runs, facilitated the detection of small deviations from the control state. The results showed by the different control variables encouraged the use of the proposed control scheme to any monitoring variable. Humidity and temperature measurements confirmed the reliability of the developed control scheme. The rotating distributor employed during the drying tests increased the drying rate of the process compared to a static distributor configuration.

4.2 Introduction

The main objective of any monitoring system is the elimination of variability in the process to obtain a high reproducibility. However, regardless of the quality of the design or maintenance of the industrial process, a certain amount of inherent or natural variability will always exist. Dealing with this variability is still a difficult task for coating, granulation and drying fluidized bed processes (Faure *et al.*, 2001). Furthermore, as the mechanisms involved in processes such as layer coating, agglomerate formation, drying and attrition, are quite complex and appear simultaneously, the development of on-line monitoring strategies is still a difficult task (Silva *et al.*, 2011; Freire *et al.*, 2012). Therefore, the monitoring system should quickly detect the process deviations, and their analysis may identify the causes of variation. In spite of the wide amount of measurements and signal analysis techniques available for the description of a fluidized bed process, it is still difficult to find a general procedure to set up an on-line monitoring system capable of defining a control state for a fluidized bed (van Ommen *et al.*, 2011). Some efforts have been made through the application of different control strategies, such as the PI or PID controllers, fuzzy logic, neural networks, and models based on experimental design techniques (Mcfarlane *et al.*, 1983; Chong *et al.*, 1987; Atthajariyakul & Leephakpreeda, 2006; Croxford & Gilbertson, 2006; Barletta *et al.*, 2008; Silva *et al.*, 2011). Similarly, other works dealt with the design of an on-line monitoring strategy for the description and identification of problems in fluidized bed processes analyzing pressure signals in the time (Johnsson *et al.*, 2000; Briens & Briens, 2002), frequency

(Kage *et al.*, 2000) and state space domain (Schouten & van den Bleek, 1998; van Ommen *et al.*, 2000; Bartels *et al.*, 2009). These works are focused on the development and performance analysis of a specific monitoring tool, showing its high sensitivity to detect problems in the fluidization behavior. Nevertheless, in this work a straightforward control scheme that could be applied to any monitoring tool is presented. To do that, the present study proposes the use of the Statistical Process Control (SPC) method for the detection of process deviations in fluidized beds (Shewhart, 1930).

The Statistical Process Control theory has been widely applied to improve the quality of many industrial processes. This theory is based on the central limit theorem. This theory allows the definition of the control state limits, facilitating to find the causes of variation and to bring the process back to the control state (Montgomery, 1997). Nowadays, this method has been applied to the control of fluidized beds together with multivariate analysis and external control loop (Kano *et al.*, 2004; Burggraeve *et al.*, 2011). The definition of a control zone based on the analysis techniques of the pressure signals is not straightforward due to the chaotic and complex nature of the pressure fluctuations. In order to ensure the validity of the proposed control scheme, several analysis techniques in the time and the frequency domains were considered.

In this chapter, a procedure for the design of a continuous control scheme for fluidized bed processes based on the SPC theory is developed. The statistical treatment of the variables allowed the definition of the control state through the study of the sample size and their underlying distribution. To analyze the performance of the control scheme, paste drying experiments with sand particles as inert medium were carried out (Nakagawa *et al.*, 1992; Freire *et al.*, 2012). This drying process was analyzed measuring humidity and temperature of the air flow to assess the reliability of the control scheme (Kannan *et al.*, 1995; Akhavan *et al.*, 2009; Wormsbecker *et al.*, 2009; Briens & Bojarra, 2010). The results show the capability of the control scheme to detect deviations from the control state.

4.3 Experimental setup

The tests were conducted in a lab-scale cylindrical bubbling fluidized bed equipped with an electrical motor in order to produce the rotation of the distributor. The cylindrical vessel has an inner diameter, D, of 0.192 m, and a height of 1 m. The fixed bed height, h_b, was $0.75D$ for all the experiments.

The rotating distributor was a perforated plate with an open area of 3%, with the holes distributed in a triangular mesh with a pitch of 11 mm. The distributor could rotate in the horizontal plane since it was coupled to the shaft of an electric motor by a conical gear. Two types of experiments were carried out in this facility, those with the rotating distributor using an angular velocity of 100 rpm, and those with a static distributor. A scheme of the mechanical device is shown in Figure 4.1.

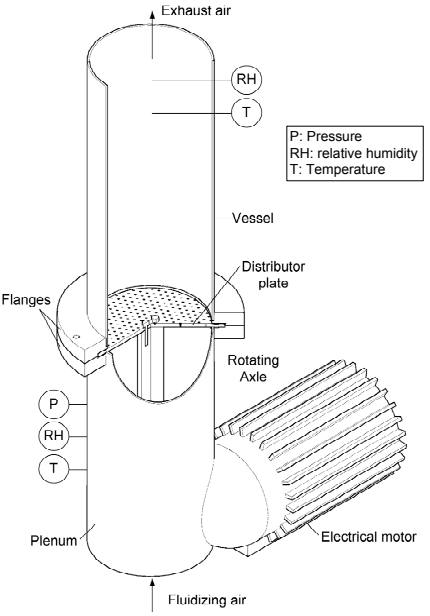

Figure 4.1: 3D sectional diagram of the experimental fluidized bed with a rotating distributor.

The bed material was silica sand particles, classified as Group B according to Geldart′s classification (Geldart, 1973). The particle density was measured to be 2645 kg/m^3 with a standard deviation of 2.5 kg/m^3, and the mean particle diameter was 683 μm. The bed was fluidized with air at ambient conditions, measuring the flow rate with a rotameter. The minimum fluidization velocity was measured to be $U_{mf,s} = 0.33$ m/s and $U_{mf,r} = 0.31$ m/s for the static and rotating distributor respectively.

The measurement system consists of a local pressure probe with 4 mm of internal diameter and a length of 0.10 m, which guaranteed an undisturbed transfer of the signal (van Ommen *et al.*, 1999), connected to a Kistler sensor. The pressure probe was placed through the bed wall at the plenum chamber.

The measurements from the Kistler 5015 sensor were amplified using a Kistler amplifier type 50515, which incorporates a low pass filter at 0.16 Hz, and a high pass filter at 200 Hz. The signal was stored in a PC using a National Instruments data acquisition system type 9234 with 4 analog input channels, 24-bit resolution, working at a sampling frequency of $f_s = 400$ Hz.

Temperature and humidity data were obtained using two transmitters E+E Electronik Model 33PFT-JX. The humidity/temperature transmitters were placed at the plenum chamber and at the freeboard (1 m above the distributor). The accuracy of the temperature transmitter was $\epsilon = \pm 0.1\ ^o$C, while the humidity sensor presents a value of $\epsilon = \pm 1.3\%$. The inlet temperature and humidity were just monitored, but not controlled. The temperature and humidity of the air at the plenum chamber were measured to be $T_{in} = 15^o$C and $RH_{in} = 6.5\%$, respectively, for all the experiments.

4.4 Experimental procedure

Two type of experiments were conducted: (i) maintaining a controlled operation state at the relative fluidization velocity of $U_r = U/U_{mf,r} = 1.6$, and (ii) studying paste drying tests by means of the proposed moving average control charts. In the former case, the control state was defined for the bed working with the static distributor at $U_r = 1.6$. The pressure fluctuations were measured during 30 min to characterize the control state. This pressure signal was used to determine the properties of the control charts, such as the window size and the underlying distribution used to compute the control limits.

Once the monitoring system was designed, the reliability of this strategy was studied for paste drying tests with sand particles as inert medium. Drying of sludge or paste-like materials in fluidized beds is an appealing process to produce granules or reduce the moisture content that is typically controlled by temperature and humidity sensors (Freire *et al.*, 2012). As the moisture was removed, these agglomerates became fragile and were disintegrated due to the attrition of the bed particles. However, the main drawback for ensuring a good process performance is maintaining the adequate fluid dynamic conditions (Lee & Kim, 1993; Shin *et al.*, 2000; Kudra *et al.*, 2002). To deal with this difficulty, the measured pressure signals were studied employing the proposed control scheme. Furthermore, to check the performance of the control system, both temperature and humidity measurements were analyzed. The tests started with the bed working with the static distributor in the control state. Then,

a substantial change in the fluidization conditions was produced by adding 150 ml of water at the bed surface. The subsequent agglomerates formation reduced the fluidization quality due to the channels appearance (Freire *et al.*, 2012; Gómez-Hernández *et al.*, 2012). Once the dynamic behaviour of the bed was deteriorated, different attempts to improve the performance of the drying process were carried out using the static and the rotating distributor.

4.5 Methods of analysis

The pressure fluctuation signals were studied in the time domain with the standard deviation and the average cycle time of the pressure fluctuations, and in the frequency domain using the wide band energy analysis. Furthermore, as the control state of the fluidized bed dynamics was disturbed by the agglomerates formation, the recovery of the fluidization quality can be analyzed as a batch-drying process (Kannan *et al.*, 1995). Thus, the humidity and temperature measurements were used to check the reliability of the control scheme.

4.5.1 Time domain analysis: standard deviation and average cycle time

The standard deviation of the pressure fluctuations, σ, has been widely applied to analyze the fluidization quality. It has been employed for the on-line monitoring of fluidized-bed hydrodynamics as well as for the analysis of the recuperation process of a defluidized bed (Chong *et al.*, 1987; van Ommen *et al.*, 2004; Davies *et al.*, 2008; Gómez-Hernández *et al.*, 2012).

The average cycle time, t_{av}, was also calculated for the characterization of the fluidized bed behavior in the time domain. The average cycle time can be defined as twice the total measurement time divided by the number of crossings with the average value (vander Stappen, 1996). Previous works showed that this variable is virtually independent of the gas velocity but strongly affected by the particle agglomeration in the bed (vander Stappen, 1996; Briens & Briens, 2002; Bartels *et al.*, 2009).

4.5.2 Frequency domain analysis: wide band energy

The variables used for the design of the control scheme were obtained directly from the raw pressure signal recorded at the plenum chamber. The wide band energy, E_{WB}, was obtained computing the energy contained within the power

spectral density (PSD). This variable is defined as the ratio between the energy in a frequency region and the energy of the whole frequency domain and can be used to detect changes in the fluidization behavior (Johnsson *et al.*, 2000). In Chapter 3, both the visual and the Student′s t-distribution methods for the frequency division were analyzed. The visual frequency division approach showed that the frequency regions obtained were able to detect neither the change in the bed aspect ratio nor the beginning of the rotating distributor, preventing its use to compute the wide band energy. Therefore, in this chapter the Student′s t-approximation of the cumulative energy distribution (CE) of the PSD was employed to divide the frequency spectra. As a result, the CE frequency distribution can be divided in three regions: two regions of poor matching that correspond to the tails of the CE distribution, and a region of good matching corresponding to the highest energy content of the distribution. According to this approach, the frequency limits that defined the three frequency regions were found to be $f_{cI} = 2.54$ Hz and $f_{cII} = 2.93$ Hz for the fluidization conditions used in this work. Regarding the physical meaning of the frequency regions in which the wide band energy was calculated, the low frequencies codified within E_{WB1} identify the long-term behavior of the bed, detecting changes in the macro-structure of the flow. E_{WB2} contains the dominant frequencies influenced by the bulk dynamics of the bed, while E_{WB3} is usually related to the fast fluidization phenomena, informing about the channels appearance since it computes the energy codified at the higher frequencies of the power spectrum.

4.5.3 Drying analysis

The amount of water dried during the experiments was estimated continuously to assess the control scheme results. The percentage of water removed after the water addition, Δm, was calculated using the relative humidity and temperature measurements at the inlet and outlet of the fluidized bed facility. Thus, Δm is defined as a ratio between the amount of water removed and the total mass of water introduced in the bed, and it can be obtained from a mass balance in the bed

$$\frac{dm}{dt} = \frac{A_t U M_v}{R} \left(\frac{p_{v,s}(T_{out}) RH_{out}}{T_{out}} - \frac{p_{v,s}(T_{in}) RH_{in}}{T_{in}} \right) \tag{4.1}$$

where A_t is the cross sectional area of the bed, U the air velocity, M_v is the molecular weight of water vapor, R is the universal gas constant, T the measured temperature, RH the measured relative humidity and $p_{v,s}$ the saturated vapor pressure of water, which was estimated by Clasius-Clapeyron relation.

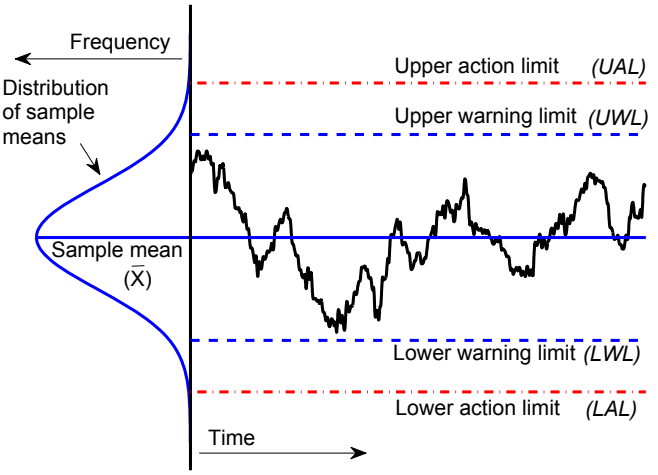

Figure 4.2: Control chart scheme.

Integrating Eq. (4.1) between the beginning and the end of the experiment, the percentage of water dried Δm was obtained.

4.6 SPC scheme design

A process whose fluctuations are produced only by random or common causes is said to be under statistical control. However, other processes may present sources of variability that are not part of the chance cause pattern, such as agglomeration or defluidization of fluidized beds, and might produce the deviation from the control state (Shewhart, 1925; Montgomery, 1997). The SPC method uses control charts to statistically describe the control state of the process. A typical control chart, Figure 4.2, contains a center line representing the average value in the control state of the monitored variable (Montgomery, 1997). There are also two external horizontal lines, called Upper Action Limit (UAL) and Lower Action Limit (LAL), which define a range of controlled operation of the process. Another two horizontal inner lines, named Upper Warning Limit (UWL) and Lower Warning Limit (LWL), are often employed to establish a warning zone in order to promote the sensitivity of the chart. This tool checks if the current sample mean is between the control limits, which is the null hypothesis H_0; or if it exceeds any of the control limits, which is the alternative hypothesis H_1.

The control limits are computed as a multiple of the standard deviation

when the samples present a normal distribution. These limits, usually known as $3-\sigma$ limits, establish a probability of $P(x) = 0.00135$ for exceeding the action limits in one direction (Montgomery, 1997)

$$LAL = \bar{X} - 3\sigma \tag{4.2}$$

$$UAL = \bar{X} + 3\sigma \tag{4.3}$$

where $\bar{X}$ is the mean value and σ is the standard deviation of the variable in the control state. These $3-\sigma$ limits are widely used in industry even when the variable follows a non-normal distribution (Montgomery, 1997). This assumption of normality implies that the control limits will be symmetrical about the center line of the chart. The validity of this assumption is based on the skewness and kurtosis values of the sample distribution as well as the sample size in which the average is based. Figure 4.3 illustrates the effect of estimating the action limits at $\pm 3\sigma$ when the underlying distribution of the variable is non-normal, for instance a $\Gamma(2,2)$ distribution. The action limits of the gamma distribution were computed at a probability of 0.001 of a point exceeding the control limits

$$P(x < LAL) = 0.001 \tag{4.4}$$

$$P(x > UAL) = 0.001 \tag{4.5}$$

According to Figure 4.3, the action limits of the gamma distribution would fall far from the $3-\sigma$ limits of the normal distribution. In these cases, the use of the $3-\sigma$ limits means that the risk of detecting false alarms would be increased for positive variations, while the risk of detecting a deviation from the control state would be significantly reduced for negative variations. The result would be an increase in the risk of a chance variation beyond the control limits. Some authors have studied the effect of the non-normality of the sample distribution (Yourstone & Zimmer, 1992; Polansky, 2005). Different procedures have been employed, such as the use of a control chart based on the median rather than the mean or a nonparametric approach (Janacek & Meikle, 1997; Vermaat *et al.*, 2003). In this work, when the sample distribution is non-normal, a generalized distribution, such as the Generalized Extreme Value (GEV) or the Burr distributions, is proposed to fit the measured data (Yourstone & Zimmer, 1992; Haynes *et al.*, 2008). The parameters of this family of statistical distributions are estimated as a function of the kurtosis and skewness values of the sample distribution, facilitating the fitting, and thus, reducing the risk of false alarms.

The Kolmogorov-Smirnov test is proposed as a tool to determine the underlying distribution for a sample distribution once the normality assumption is rejected.

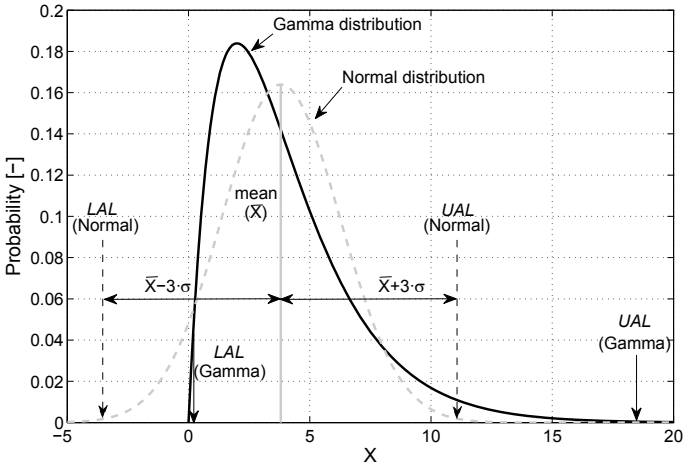

Figure 4.3: Differences between the control limits estimated using the Normal and Gamma distributions.

The Kolmogorov-Smirnov test is a simple method to test if an empirical sample follows a specific distribution, which is the null hypothesis H_0, against the alternative hypothesis H_1 that it follows a different distribution. The test compares the cumulative distribution function of the sample $S_n(x)$ (i.e. the cumulative energy distribution), with the statistic cumulative distribution function CDF, which is the fitted statistic distribution. The comparison is based on the distance between the cumulative distributions, D_n, defined as the maximum difference between the two distributions

$$D_n = \max|S_n(x) - CDF(x)| \tag{4.6}$$

The distance between the cumulative distributions is used to obtain the modified statistic D^*, which is compared with the critical values of this test for a certain level of significance α, Eq. (4.7) (Shewhart, 1925). This value varies as a function of the sample size n, which is computed as a function of the size of both cumulative distributions n_1 and n_2, Eq. (4.8).

$$D^* = D_n \left(\sqrt{n} + 0.11 + 0.12/\sqrt{n}\right) \tag{4.7}$$

$$n = \frac{n_1 n_2}{n_1 + n_2} \tag{4.8}$$

The Kolmogorov-Smirnov test is constructed by using the critical values of the Kolmogorov distribution (Stephens, 1970). The null hypothesis is rejected at level of significance α if $D^* \geq K_\alpha$, where K_α is found from the Kolmogorov distribution as follows

$$P(K \leq K_\alpha) = 1 - \alpha \tag{4.9}$$

The control charts employed in this work were obtained using a moving mean approach. In this scheme, the experimental data is continuously computed in sample sizes of length W_t. The procedure for establishing the SPC scheme can be summarized as follows:

1. Determination of the moving window size (W_t).
    - Measurement of the control state with a long time signal (30 min).
    - Definition and computation of the control state for the variables.
    - Determination of the number of measurements needed to obtain a similar value to the control state. In the frequency domain, the Kolmogorov-Smirnov test with a significance level $\alpha = 5\%$ was used to compare between the cumulative energy distribution of W_t and the cumulative energy distribution of the reference state (Stephens, 1970).
    - Selection of the median value of the W_t distribution as the sample size.
2. Study of the underlying distribution.
    - Analysis of the control signal using the W_t in a moving mean scheme.
    - Checking the normality of the sample distribution using the normality plots, the kurtosis and skewness values and the maximum likelihood estimation method, MLE (Dempster, 1977). The MLE provides the characteristic parameters of the statistic distribution with 95% confidence intervals. Thus, when the characteristic parameters of the normal distribution (mean and standard deviation), which are calculated using the theoretical statistic equations, are inside the MLE′s confidence intervals, the normal distribution could describe the sample distribution.
    - Otherwise, when the sample distribution shows a non-normal behavior, the underlying distribution can be determined by the minimization of the test statistic D_n, which is computed using Eq. (4.6).

The fitted statistic distribution that shows the minimum distance between the cumulative form of the sample distribution and its cumulative distribution function is used to describe the data.

3. Estimate the control limits using the $3-\sigma$ limits when the variable can be described by a normal, or for a probability of 0.001 when the variable is described by a different distribution.

4.7 Results

The implementation of the moving mean control chart methodology was performed through the analysis of: (i) a 30 min signal with the bed operating under control state in order to determine the moving window size, (ii) the underlying distribution that described each monitored variable in the control state, and, once the control charts were designed, (iii) several drying tests.

4.7.1 Moving window size

For a basic design of a moving mean control chart, the sample size or window length, W_t, of the moving window used to estimate the monitored variables must be specified. W_t should be large enough to obtain representative results of the pressure fluctuation signals. In order to determine this number of measurements, Wilkinson (1995) compared the standard deviation values of pressure signals characteristic of the control state, which were estimated using a long signal length, with the pressure standard deviation values calculated for different W_t. Following the approach of Wilkinson (1995), these results were computed from the beginning of the signal to successive increments of the number of measurements considered until these values were inside an acceptable range. This acceptable range is defined as a variation of $\pm 5\%$ over the standard deviation value of the control state, which is estimated using the whole pressure signal. Nevertheless, this approach might be influenced by the initial point of the signal at which the variable values are estimated, and thus, the W_t obtained could not be representative of the entire signal. Thus, it is mandatory to avoid the influence of the initial point used on the estimation of W_t. To do that, the approach developed by Wilkinson (1995) was repeated using different initial points of the pressure signal to calculate the value of the standard deviation for each W_t. In this way, a distribution of the W_t values that are inside the

acceptable range is obtained. This approach was also used to calculate W_t for the average cycle time.

For the time domain variables, a variation of $\pm 5\%$ was accounted as the acceptable limit (Wilkinson, 1995), whereas the reference values were obtained considering a 30 min signal length. The distribution of W_t that are inside the acceptable range for the time domain variables are represented in the relative histograms of Figure 4.4, showing an asymmetric distribution of the sample sizes. This encouraged the use of the median to estimate W_t as the most representative value of the distribution. Therefore, the window length was fixed to $W_t = 25$ s and $W_t = 35$ s for the standard deviation and the average cycle time, respectively.

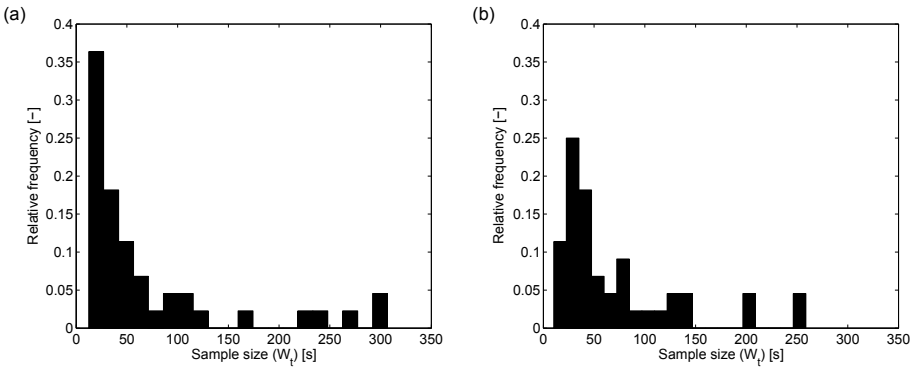

Figure 4.4: Histogram of the window sizes, W_t, for: (a) standard deviation and (b) average cycle time.

Furthermore, as the wide band energy was computed through the power spectrum of the pressure fluctuations, some spectral features must be taken into account. As stated by Brown & Brue (2001), an accurate PSD estimation requires the average of several periodograms. This averaged nature of the frequency results complicates the selection of the parameters used to compare between the reference state and the W_t results. Therefore, the degree of approximation between the reference and the W_t results was studied comparing the shape of both cumulative energy distributions of the PSD. Such a comparison was conducted by means of the Kolmogorov-Smirnov test (Stephens, 1970). The null hypothesis, H_0, assumed that the cumulative energy distribution of the entire signal and the cumulative energy distribution obtained for each W_t are similar, against the alternative hypothesis, H_1, that they are different. A significance level of $\alpha = 5\%$ was used to compute the Kolmogov-Smirnov test.

Following the considerations about the starting point and considering the characteristics of E_{WB}, W_t was estimated as follows: (i) from the initial point of the reference signal, the window size was increased until its cumulative energy distribution was similar to the cumulative energy distribution of the reference state, and (ii) once the Kolmogorov-Smirnov test did not reject the null hypothesis, the previous step was repeated changing the initial point of W_t. Following this procedure, a wide distribution of W_t values was obtained. The procedure was applied to the control state signal through the moving mean scheme. Similarly to the time domain results shown in Figure 4.4, the window length of the frequency domain showed an asymmetric distribution, as can be observed in Figure 4.5. A window length of $W_t = 50$ s was employed for the computation of the wide band energy.

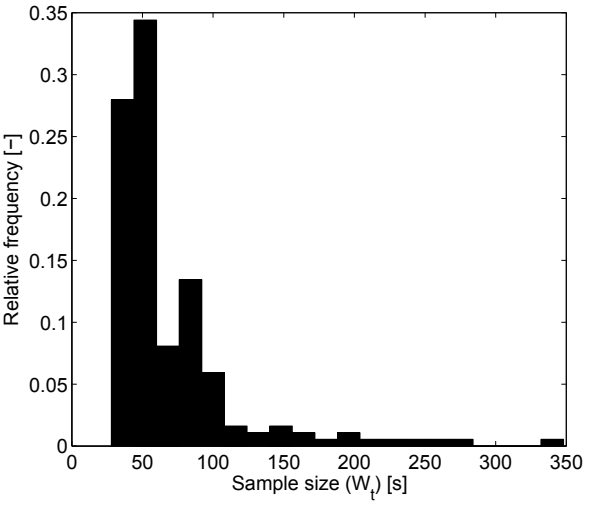

Figure 4.5: Histogram of the window sizes, W_t, for the wide band energy.

4.7.2 Underlying distribution

The determination of the statistical distribution that better describes the sample distribution of each variable is necessary in order to estimate the control limits. The 30 min control signal was analyzed using the time and frequency variables with the window sizes determined previously.

First of all, the capability of the normal distribution to describe the sample distribution was checked. Figure 4.6 checks the normality assumption while Table 4.1 presents the values of the parameters of the sample distributions. Figure

Table 4.1: Parameters of the sample distributions.

	classical estimation				MLE estimation	
	kurtosis	skewness	mean	standard	mean	standard deviation
	(k)	(s)	(μ)	(σ)	$\bar{X} \pm interval$	$\bar{\sigma} \pm interval$
σ	2.95	-0.15	261.71	11.31	261.71 ± 0.02	11.31 ± 0.02
t_{av}	3.17	-0.15	0.2683	0.013	0.2683 ± 0.0001	0.0130 ± 0.0001
E_{WB3}	2.93	-0.02	0.3775	0.0386	0.3775 ± 0.0001	0.0386 ± 0.0001
E_{WB2}	3.13	-0.38	0.4827	0.0423	0.4827 ± 0.0001	0.0423 ± 0.0001
E_{WB1}	2.70	0.03	0.1398	0.0227	0.1398 ± 0.0001	0.0227 ± 0.0001

4.6 shows the normal probability plots used to test the normality of the variables. In these figures, the data are plotted together with a theoretical normal distribution (dash-dot line). As can be seen for the standard deviation, average cycle time, E_{WB1} and E_{WB3} in Figure 4.6-a/b/c/e, the data showed a nearly linear trend with only small discrepancies at the tails of the distributions. Only E_{WB2}, showed in Figure 4.6-d, presents a higher deviation from the straight line typical of the normal distribution, which can be explained due to its greater skewness value, Table 4.1.

The maximum likelihood estimation method was used to test the use of the normal distribution to describe the three variables. This method estimates the unknown parameters of the normal distribution, which are the mean, $\bar{X}$, and the standard deviation, $\bar{\sigma}$, by the maximization of the sample likelihood with a certain confidence interval. Such an estimation can be compared to the mean and standard values, μ and σ, calculated using the theoretical expressions reported by Johnson & Kotz (1970). Therefore, it can be employed to determine whether the theoretical distribution fits properly the sample distribution or not. When the parameters μ and σ are inside the confidence intervals obtained for $\bar{X}$ and $\bar{\sigma}$, the theoretical approximation can describe the sample distribution. However, when the parameters estimated with the classical approach are out of the MLE results, the statistical distribution cannot fit properly the data. As can be seen in Table 4.1, the mean, μ, and standard deviation, σ, of all the variables were inside the confidence limits obtained by the MLE. Therefore, the normal distribution was used to describe all the variables and estimate the control limits.

It is worth to point out that, when the sample distribution cannot be described by a normal distribution, GEV or the Burr distributions can be used as an alternative (Yourstone & Zimmer, 1992; Haynes *et al.*, 2008). Thus, the

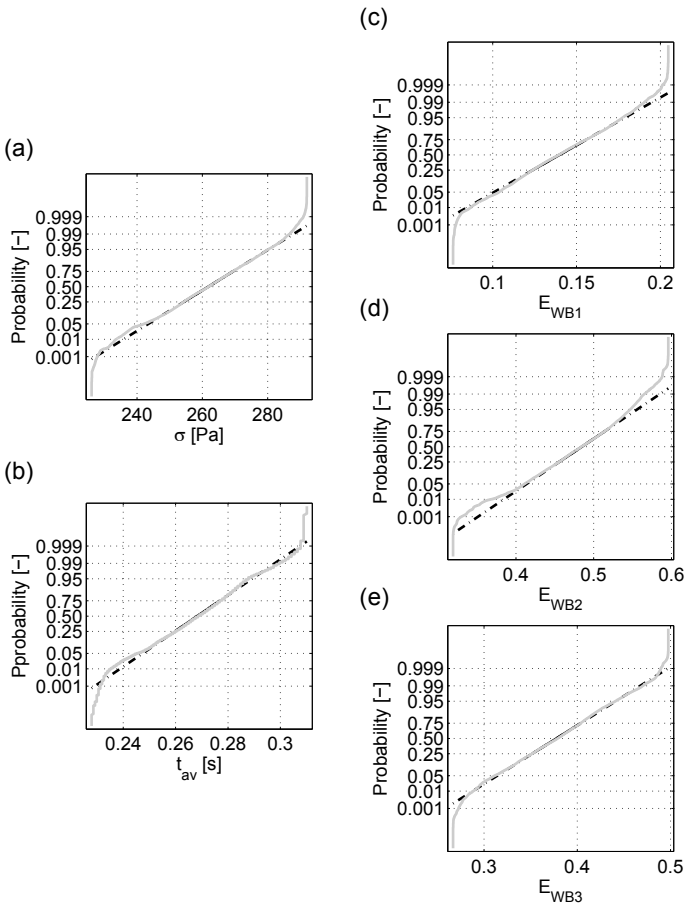

Figure 4.6: Normality plots for the experimental data of (a) standard deviation, (b) average cycle time, (c) E_{WB1}, (d) E_{WB2} and (e) E_{WB3}; dash-dot line represents the values of the Normal distribution.

sample distribution should be fitted to the proposed statistical distribution. Then, the maximum distance between the theoretical distribution and the experimental result, D_n, which is obtained from Eq. (4.6), would be used as a comparison parameter. The theoretical distribution that minimizes Eq. (4.6) should be the underlying distribution used to compute the control limits.

4.7.3 SPC applied to agglomeration phenomena

The SPC scheme was applied to monitor paste drying tests in order to illustrate the use of the control charts. The sticky zone formed after the water addition

prevented the homogeneous distribution and formation of bubbles. Due to the cohesive behavior of these agglomerates, channels appeared throughout the defluidized bed. Two different attempts for this drying process were carried out: (i) with the static distributor, and (ii) with the rotating distributor.

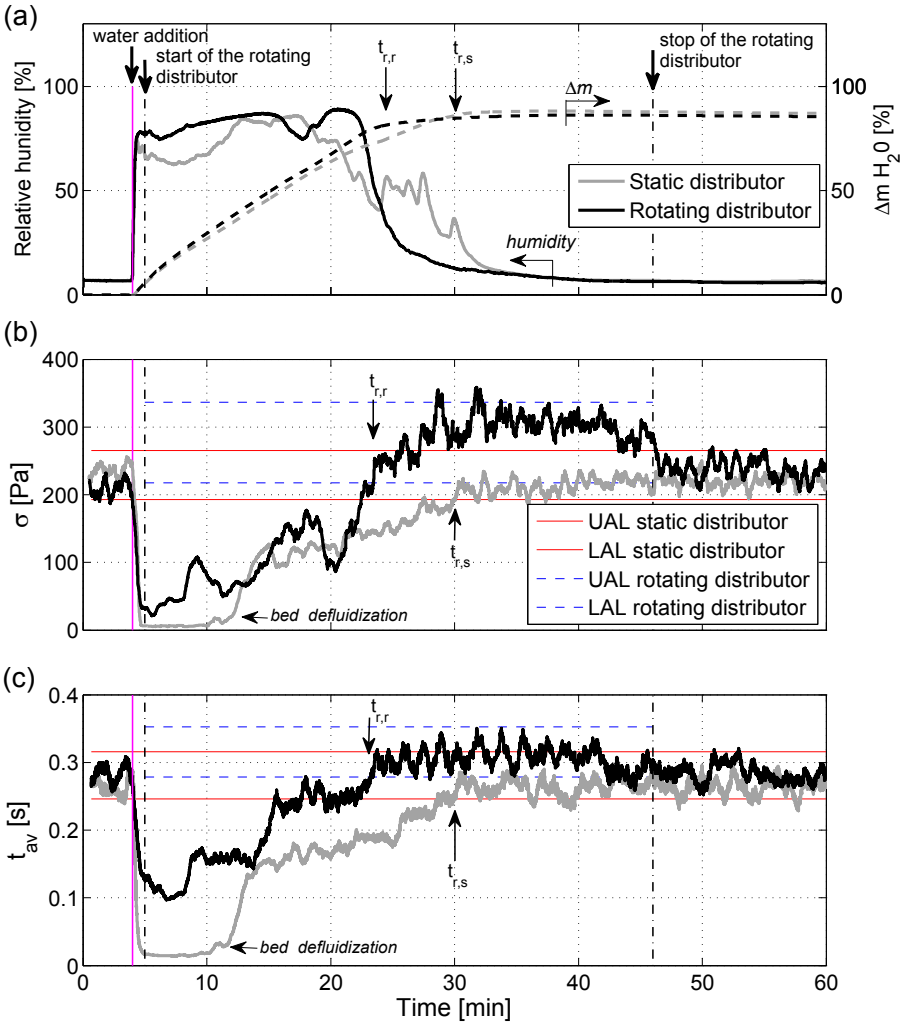

Figure 4.7: Monitoring of the agglomeration tests for the static distributor (gray line) and the rotating distributor (black line): (a) relative humidity of the outlet air, control charts: (b) standard deviation and (c) average cycle time.

The results for the static and the rotating distributor tests are presented in Figure 4.7 in gray and black color lines respectively. In Figure 4.7-a, the left axis describes the evolution of the relative humidity of the exhaust air, whereas

Table 4.2: Time needed to recover the control state.

variable	Recuperation time [min]	
	Static distributor [$t_{r,s}$]	Rotating distributor [$t_{r,r}$]
Δm	26	21
σ	26	21
t_{av}	26	21
E_{WB3}	25	21
E_{WB2}	25	21
E_{WB1}	-	26

the right axis shows the percentage of water dried, estimated integrating Eq. (4.1). The control charts of the time domain variables are also included in Figure 4.7. These charts were plotted with the same horizontal axis, the time of the test. A vertical line points out the water addition (solid line) and the start and end of the distributor rotation (dash-dot line) for all the plots. As stated previously, the control charts were obtained with $W_t = 25$ s and $W_t = 35$ s for the standard deviation and average cycle time, respectively, and using the normal distribution to estimate the control limits for all the variables. In the moving average control charts, presented in Figure 4.7-b/c, the upper and lower action limits are plotted in red-solid line for the static distributor test, and in blue-dash line for the rotating distributor test. In all the plots, the arrows inform about the instant when the variable returns to the control state. These values are summarized in Table 4.2.

Focusing on the drying process showed in Figure 4.7-a, the water addition was instantaneously detected by the humidity sensor located at the freeboard. This sensor measured higher humidity values using the rotating distributor, suggesting a faster drying process than for the static distributor test. This drying improvement was also shown by a higher percentage of water dried, Δm. However, only 90% of the 150 ml of water added was dried in both tests. This result could be caused by the water absorption of the silica sand particles or the pneumatic transport of some water droplets at the beginning of the test. In any case, when Δm is near to the stationary value of 90%, the relative humidity started to decrease, diminishing the drying rate (Kannan *et al.*, 1995; Akhavan *et al.*, 2009). Significant differences can be observed in Figure 4.7-a at $t = 22$ min for the static and rotating tests. While the humidity of the rotating distributor test decreased drastically to the control state, the

static distributor test showed a smoother humidity falling rate with some peaks. A non homogeneous drying explains the humidity peaks shown in the static distributor test. In this test, some agglomerates might be located at the dead zones between the holes of the distributor and attached to the bed wall. Due to the high cohesiveness of these agglomerates, they were barely affected by the air flow. Thus, when the sticky defluidized zone is partially dried, some of these agglomerates were broken and moved into the bubbling zone, starting then to dry, and thus, causing the humidity peaks.

Concerning the control charts, the control limits were estimated using the 30 min signal as reference state. No false alarms were detected during the first 4 min, while the bed was working with the static distributor and with no agglomerates. The paste formation produced the deviation from the control state for all the variables, as shown in Figures 4.7-4.8. The low values of the standard deviation presented in Figure 4.7-b, and the average cycle time shown in Figure 4.7-c identified the bed defluidization. During this period, some channels were visually observed near the distributor. As the sticky agglomerates started to dry, the standard deviation and the average cycle time increased towards the control state. A similar trend was observed for both variables in Figure 4.7-b/c for the static and the rotating distributor tests. However, due to the rotating distributor, the attrition and disintegration of the agglomerates was improved, obtaining a lower time to recover the control state, as can be observed in Table 4.2. Also, when the distributor rotation was stopped, both variables returned to the static control limits. This effect showed the sensitivity of the control scheme to detect small fluidization changes such as the rotation of the distributor.

The wide band energy results shown in Figure 4.8 can be explained in terms of the energy contained on each frequency region. Thus, the paste formation caused a high energy transfer from E_{WB2} (Figure 4.8-b) to E_{WB3} and E_{WB1} (Figure 4.8-a/c) in both tests. The energy transfer from E_{WB2} to the other frequency regions informed about the defluidization of the bed since the bulk motion was prevented. Thus, channels were formed increasing the energy content of the higher frequencies, E_{WB3}, and the larger structures of the flow were changed, E_{WB1}.

Focusing on the static distributor test presented in Figure 4.8-a, the channels were maintained during most of the recuperation process due to the non homogeneous distribution of the airflow through the bed. Thus, only the agglomerates that were located next to the channels were dried fast. This relation between the drying mechanism and the channels explains the similar trend

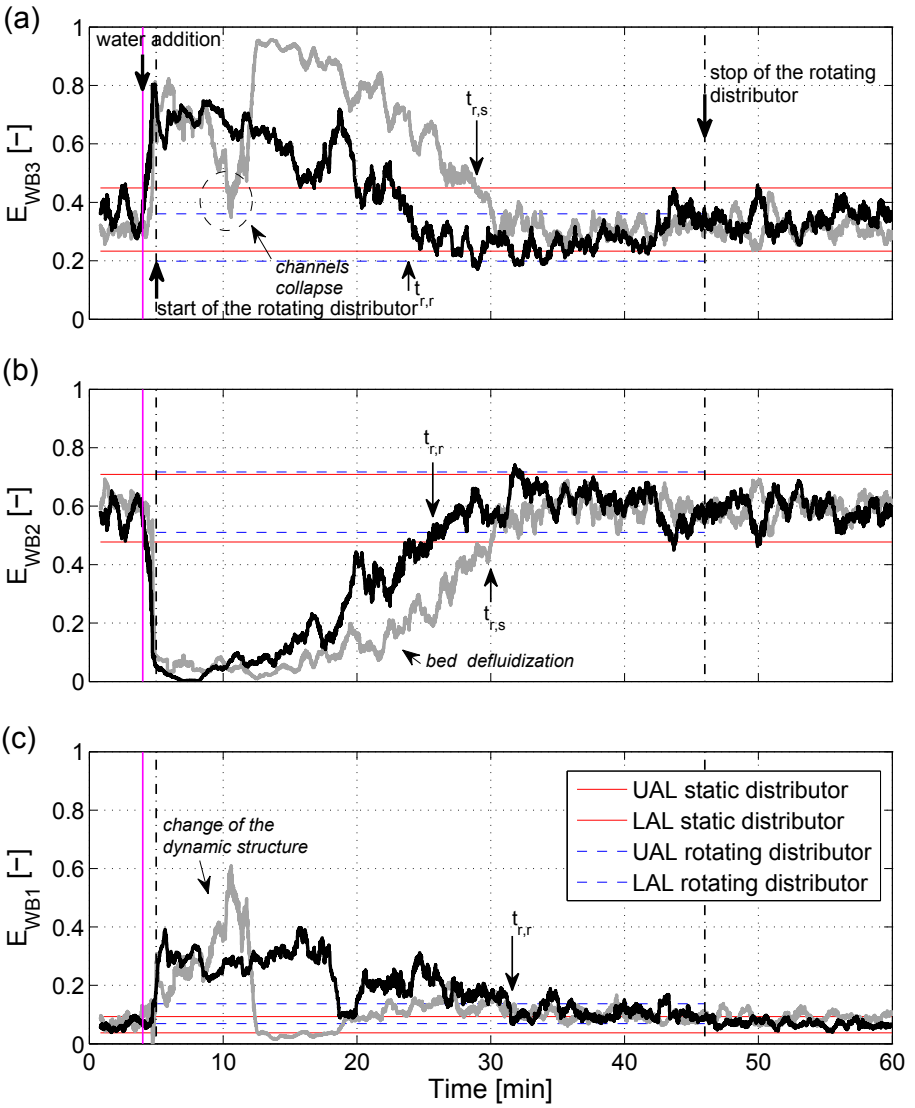

Figure 4.8: Monitoring of the agglomeration tests for the static distributor (gray line) and rotating distributor (black line), control charts: (a) E_{WB3}, (b) E_{WB2} and (c) E_{WB1}.

shown by the decrease of the humidity measurements, which is presented in Figure 4.7-a, and E_{WB3}, shown in Figure 4.8-a.

The energy lost in E_{WB3} and E_{WB1} was transferred to E_{WB2} until the control state was reached. During this recuperation process, at $t = 10$ min it was visually observed that the main channels were suddenly blocked due to

the motion of the agglomerates that formed those channels. This phenomenon produced the energy decrease of E_{WB3} to the control state, as shown in Figure 4.8-a. However, in spite of these control values, the bed was deviated from the control state since the values of E_{WB2} and E_{WB1} were still out of the control limits, as can be seen in Figure 4.8-b/c. Similar recuperation times were obtained for E_{WB3} and E_{WB2}, while the values obtained for E_{WB1} fluctuated around the UAL during the entire experiment in the static distributor test. These values out of the control zone for E_{WB1} might be produced by the presence of agglomerates between the holes of the distribution, capable of changing the larger structures of the fluid flow.

The beginning of the distributor rotation promoted the radial dispersion of particles and the reduction of the dead zones over the distributor (Sobrino *et al.*, 2008). Therefore, the agglomerates settled over the distributor were broken by the distributor rotation. These effects enhanced the channels breakage, producing the energy transfer from E_{WB3} to E_{WB2}. The agglomerates located close to the water addition zone were distributed within the fluidized bed, leading to a faster recuperation of the control state for the rotating distributor test, obtaining lower recuperation times in this case (Table 4.2).

4.8 Conclusions

The statistical approach proposed to define the properties of the moving mean control charts facilitates the development of the control scheme for the continuous monitoring of fluidized bed processes. A new procedure was proposed to compute the minimum number of measurements, W_t, guarantying reliable results for variables in both the time and frequency domains. The analysis of the normality assumption for the sample distribution reveals the influence of the underlying distribution on the value of the control limits. A different statistic distribution should be used when the variables cannot be described by a normal distribution in order to avoid the appearance of false alarms during the fluidization tests.

The results shown by the different control variables encouraged the use of the proposed control scheme to any monitoring variable. The definition of the control state also improved the sensitivity of the variables, detecting small deviations from the reference state. Humidity and temperature measurements of the drying tests confirmed the reliability of the control scheme.

Moreover, the analysis of the control charts demonstrated the improvement

of the rotating distributor to recover the control state. The distributor rotation broke the channels and agglomerates, which enhanced the attrition and subsequent reduction in size of the agglomerates, and thus, improved the drying rate of the process. A different fluidized behavior was shown with the static distributor because of the presence of agglomerates at the dead zones over the distributor.

Notation

A_t	Cross sectional area of the bed [m^2]
D	Inner diameter of big fluidized bed vessel [m]
D_n	Distance between cumulative distributions [-]
D^*	Modified statistic of the Kolmogorov-Smirnov test [-]
E_{WB}	Wide band energy [-]
f	Frequency [Hz]
f_c	Central frequency [Hz]
f_{cI}	Lower cut-off frequency [Hz]
f_{cII}	Upper cut-off frequency [Hz]
f_N	Nyquist frequency [Hz]
f_s	Sampling frequency [Hz]
h_b	Fixed bed height [m]
H_0	Null hypothesis
H_1	Alternative hypothesis
k	Kurtosis
M_v	Molecular weight of water vapour [g/mol]
m	Mass of water [kg]
n	Sample size of the distribution [-]
$p_{v,s}$	Saturated vapour pressure of water [Pa]
$P(x)$	Probability of x [-]
R	Universal gas constant [J/(molK)]
RH	Relative humidity [%]
s	Skewness
$S_n(x)$	Empirical cumulative distribution of x [-]
t	Time [s]
t_{av}	Average cycle time [s]
$t_{r,r}$	Recuperation time with the rotating distributor [s]
$t_{r,s}$	Recuperation time with the static distributor [s]

T	Temperature [K]
U	Gas velocity [m/s]
U_r	Relative gas velocity [-]
$U_{mf,r}$	Minimum fluidization velocity with rotating distributor [m/s]
$U_{mf,s}$	Minimum fluidization velocity with static distributor [m/s]
$\bar{X}$	Process mean value
W_t	Window length [s]

Greek symbols

α	Significance level [-]
K_α	Kolmogorov threshold value [-]
Δm	Percentage of dried water [%]
ϵ	Accuracy
Γ	Gamma distribution
μ	Mean
σ	Standard deviation
$\bar{\sigma}$	Standard deviation of the MLE result
$3-\sigma$	Probability limits

Abbreviattions

CDF	Cumulative density function
CE	Cumulative energy
GEV	Generalized Extreme Value distribution
LAL	Lower action limit
LWL	Lower warning limit
MLE	Maximum-likelihood estimation method
PI	Proportional-integral controller
PID	Proportional-integral-derivative controller
PSD	Power spectra density
UAL	Upper action limit
UWL	Upper warning limit

References

Akhavan, A., van Ommen, J. R., Nijenhuis, J., Wang, X. S., Coppens, M.O. & Rhodes, M. J. 2009 Improved drying in a pulsation-assisted fluidized bed. *Industrial & Engineering Chemistry Research* 48 (1), 302–309.

Atthajariyakul, S. & Leephakpreeda, T. 2006 Fluidized bed paddy drying in optimal conditions via adaptive fuzzy logic control. *Journal of Food Engineering* 75 (1), 104–114.

Barletta, M., Gisario, A., Guarino, S. & Tagliaferri, V. 2008 Fluidized bed coating of metal substrates by using high performance thermoplastic powders: Statistical approach and neural network modelling. *Engineering Applications of Artificial Intelligence* 21 (8), 1130–1143.

Bartels, M., Vermeer, B., Nijenhuis, J. & Kapteijn, F. 2009 Methodology for the screening of signal analysis methods for selective detection of hydrodynamic changes in fluidized bed systems. *Industrial & Engineering Chemistry Research* 48 (6), 3158–3166.

Briens, L. & Bojarra, M. 2010 Monitoring fluidized bed drying of pharmaceutical granules. *AAPS PharmSciTech* 11 (4), 1612–1618.

Briens, L. A. & Briens, C. L. 2002 Cycle detection and characterization in chemical engineering. *AIChE Journal* 48 (5), 970–980.

Brown, R. C. & Brue, E. 2001 Resolving dynamical features of fluidized beds from pressure fluctuations. *Powder Technology* 119 (2-3), 68–80.

Burggraeve, A., van den Kerkhof, T., Hellings, M., Remon, J. P., Vervaet, C. & Beer, T. De 2011 Batch statistical process control of a fluid bed granulation process using in-line spatial filter velocimetry and product temperature measurements. *European Journal of Pharmaceutical Sciences* 42 (5), 584–592.

Chong, Y. O., Odea, D. P., White, E. T., Lee, P. L. & Leung, L. S. 1987 Control of the quality of fluidization in a tall bed using the variance of pressure-fluctuations. *Powder Technology* 53 (3), 237–246.

Croxford, A. J. & Gilbertson, M. A. 2006 Control of the state of a bubbling fluidised bed. *Chemical Engineering Science* 61 (19), 6302–6315.

Davies, C. E., Carroll, A. & Flemmer, R. 2008 Particle size monitoring in a fluidized bed using pressure fluctuations. *Powder Technology* 180 (3), 307–311.

Dempster, A.P. 1977 Maximum likelihood from incomplete data via em algorithm. *Journal of the Royal Statistical Society.Series B, Methodological* 39 (1), 1–38.

Faure, A., York, P. & Rowe, R. C. 2001 Process control and scale-up of pharmaceutical wet granulation processes: a review. *European Journal of Pharmaceutics and Biopharmaceutics* 52 (3), 269–277.

Freire, J. T., Ferreira, M. C., Freire, F. B. & Nascimento, B. S. 2012 A review on paste drying with inert particles as support medium. *Drying Technology* 30 (4), 330–341.

Geldart, D. 1973 Types of gas fluidization. *Powder Technology* 7 (5), 285–292.

Gómez-Hernández, J., Soria-Verdugo, A., Briongos, J. Villa & Santana, D. 2012 Fluidized bed with a rotating distributor operated under defluidization conditions. *Chemical Engineering Journal* 195-196 (0), 198–207.

Haynes, M., Mengersen, K. & Rippon, P. 2008 Generalized control charts for non-normal data using g-and-k distributions. *Communications in Statistics-Simulation and Computation* 37 (9), 1881–1903.

Janacek, G. J. & Meikle, S. E. 1997 Control charts based on medians. *Journal of the Royal Statistical Society: Series D (The Statistician)* 46 (1), 19–31.

Johnson, N. L. & Kotz, S. 1970 *Continuous Univariate Distributions, Volume 1*. John Wiley & Sons.

Johnsson, F., Zijerveld, R. C., Schouten, J. C., van den Bleek, C. M. & Leckner, B. 2000 Characterization of fluidization regimes by time-series analysis of pressure fluctuations. *International Journal of Multiphase Flow* 26 (4), 663–715.

Kage, H., Agari, M., Ogura, H. & Matsuno, Y. 2000 Frequency analysis of pressure fluctuation in fluidized bed plenum and its confidence limit for detection of various modes of fluidization. *Advanced Powder Technology* 11 (4), 459–475.

Kannan, C. Srinivasa, Thomas, P. P. & Varma, Y. B. G. 1995 Drying of solids in fluidized beds.

Kano, M., Hasebe, S., Hashimoto, I. & Ohno, H. 2004 Evolution of multivariate statistical process control: application of independent component analysis and external analysis. *Computers & Chemical Engineering* 28 (6âĂŞ7), 1157–1166.

Kudra, T., Gawrzynski, Z., Glaser, R., Stanislawski, J. & Poirier, M. 2002 Drying of pulp and paper sludge in a pulsed fluid bed dryer. *Drying Technology* 20 (4-5), 917–933.

Lee, D. H. & Kim, S. D. 1993 Drying characteristics of starch in an inert medium fluidized bed. *Chemical Engineering and Technology* 16 (4), 263–269.

Mcfarlane, R. C., Hoffman, T. W., Taylor, P. A. & Macgregor, J. F. 1983 Control of fluidized-bed reactors.1. modeling, simulation, and single-loop control studies. *Industrial & Engineering Chemistry Process Design and Development* 22 (1).

Montgomery, D. C. 1997 *Introduction to statistical quality control*, 3rd edn. New York: John Wiley & Sons, Inc.

Nakagawa, N., Ohsawa, K., Takarada, T. & Kato, K. 1992 Continuous drying of a fine particles-water slurry in a powder-particle fluidized-bed. *Journal of Chemical Engineering of Japan* 25 (5), 495–501.

van Ommen, J. R., Coppens, M. O., van den Bleek, C. M. & Schouten, J. C. 2000 Early warning of agglomeration in fluidized beds by attractor comparison. *AIChE Journal* 46 (11), 2183–2197.

van Ommen, J. R., de Korte, R. J. & van den Bleek, C. M. 2004 Rapid detection of defluidization using the standard deviation of pressure fluctuations. *Chemical Engineering and Processing* 43 (10), 1329–1335.

van Ommen, J. R., Sasic, S., van der Schaaf, J., Gheorghiu, S., Johnsson, F. & Coppens, M. O. 2011 Time-series analysis of pressure fluctuations in gas-solid fluidized beds - a review. *International Journal of Multiphase Flow* 37 (5), 403–428.

van Ommen, J. R., Schouten, J. C., vander Stappen, M. L. M. & van den Bleek, C. M. 1999 Response characteristics of probe-transducer

systems for pressure measurements in gas-solid fluidized beds: how to prevent pitfalls in dynamic pressure measurements. *Powder Technology* 106 (3), 199–218.

Polansky, A. M. 2005 A general framework for constructing control charts. *Quality and Reliability Engineering International* 21 (6), 633–653.

Schouten, J. C. & van den Bleek, C. M. 1998 Monitoring the quality of fluidization using the short-term predictability of pressure fluctuations. *AIChE Journal* 44 (1), 48–60.

Shewhart, W. A. 1925 The application of statistics as an aid in maintaining quality of a manufactured product. *Journal of the American Statistical Association* 20, 546–548.

Shewhart, W. A. 1930 Economic quality control of manufactured product. *Bell System Technical Journal* 9 (2).

Shin, Y. S., Kim, H. C. & Chun, H. S. 2000 Drying of water treatment process sludge in a fluidized bed dryer. *Korean Journal of Chemical Engineering* 17 (1), 22–26.

Silva, C. A. M., Parise, M. R., Silva, F. V. & Taranto, O. P. 2011 Control of fluidized bed coating particles using gaussian spectral pressure distribution. *Powder Technology* 212 (3), 445–458.

Sobrino, C., Almendros-Ibanez, J. A., Santana, D. & Vega, M. De 2008 Fluidization of group b particles with a rotating distributor. *Powder Technology* 181 (3), 273–280.

vander Stappen, M. L. M. 1996 Chaotic hydrodynamics of fluidized beds.

Stephens, M. A. 1970 Use of komogorov-smirnov,cramer-von mises and related statistics without extensive tables. *Journal of the Royal Statistical Society Series B-Statistical Methodology* 32 (1), 115–&.

Vermaat, M. B., Ion, R. A., Does, R. J. M. M. & Klaassen, C. A. J. 2003 A comparison of shewhart individuals control charts based on normal, non-parametric, and extreme-value theory. *Quality and Reliability Engineering International* 19 (4), 337–353.

Wilkinson, D. 1995 Determination of minimum fluidization velocity by pressure fluctuation measurement. *Canadian Journal of Chemical Engineering* 73 (4), 562–565.

Wormsbecker, M., T.Pugsley & Tanfara, H. 2009 Interpretation of the hydrodynamic behaviour in a conical fluidized bed dryer. *Chemical Engineering Science* 64 (8), 1739–1746.

Yourstone, S. A. & Zimmer, W. J. 1992 Nonnormality and the design of control charts for averages. *Decision Sciences* 23 (5), 1099–1113.

CHAPTER
FIVE

Multi-resolution analysis of paste drying in a rotating-distributor fluidized bed

Contents

5.1 Abstract

Humidity and temperature measurements together with pressure fluctuation signals were employed to analyze the paste drying process in a fluidized bed equipped with a rotating distributor using inert particles as support medium. The measurement of humidity and temperature of the airflow allowed the identification of four drying periods as a function of the drying operational conditions. The multi-resolution approach of the pressure fluctuation signals showed the effect of the paste drop over the bed surface on the fluidization conditions, relating the drying periods with the bed dynamics. The drying process can affect the low and high frequency details of the pressure signal when the bed state changes towards defluidization, or just the high frequency detail if the bed was

at the maldistributed state. To compare between drying and pressure analyses, a statistical monitoring approach was applied to define the recuperation time when the fluidization quality is recovered. For the static distributor, both the drying and the recuperation times showed similar values for shallow beds, while for deeper beds larger times were needed to complete the drying process than for recovering the fluidization quality. For the rotating distributor, lower drying and dynamic times were needed due to its improvement effect for shallow and deep beds.

5.2 Introduction

Many industrial applications employ fluidized beds for drying granular solids such as grains, fertilizers, chemicals, and minerals to facilitate their further processing or handling. The main advantages of fluidized bed technology for drying applications are large contact surface between solids and gas, high thermal inertia of solids, high degree of solids mixing, and rapid heat and moisture transfer between solids and gas, reducing the drying time considerably without damaging heat sensitive materials. As a result, drying rates are normally higher in fluidized bed dryers than in other types of dryers. However, any change in the fluidization state, such as agglomeration, channeling or maldistribution of the drying material inside the bed can affect the heat and mass transfer coefficients and the drying performance.

Liquid bridge forces between particles cause changes in the fluidization behavior. As moisture evaporates, the liquid bridge forces diminish and the fluidization condition changes from a cohesive to a non-cohesive state. This process can be characterized by measuring the drying rate, which is defined as the moisture loss per unit of time. When the solid is wet enough, the surface contains free moisture and the drying rate is constant. At this stage, the particle surface is saturated with water and in equilibrium with the surrounding air (Mujumdar, 2006). Hence, the drying rate is controlled by the vaporization rate of moisture at the particle surface. Once the free moisture of the surface is evaporated, moisture needs to be transported from the interior of the solid to the surface by capillary forces (Kannan *et al.*, 1994). The process at this stage is called falling rate period, and changes from a heat-transfer-limited phenomenon to a mass-transfer-limited one (Akhavan *et al.*, 2009). This drying description is characteristic for drying of granular solids (Watano *et al.*, 1998; Wang & Chen, 2000; Daud, 2008). The constant-rate period in a fluidized bed

might be too short to be observable, except under very mild drying conditions (Reay & Baker, 1985; Shin *et al.*, 2000). Other applications, such as drying of fine powders, pastes, slurries, suspensions and pulp, show just the falling rate period.

Many studies have analyzed the hydrodynamics of fluidized beds during drying of granular particles, trying to relate the process performance with the bed dynamics. These works found that the amount of water contained within the granules is related to the transition from channeling to uniform fluidization regimes. Bed-pressure drop, pressure standard deviation and dominant frequency of pressure signals have shown their potential use to evaluate the fluidization quality (Zhao *et al.*, 2004; Wormsbecker *et al.*, 2009*a*,*b*; Akhavan *et al.*, 2009; Briens & Bojarra, 2010; Dong *et al.*, 2013). In this line, Chaplin *et al.* (2004) performed a detailed comparison between the drying process of pharmaceutical placebo granules and the response of pressure fluctuations in time, frequency and state-space domains. Similarly, de Martin *et al.* (2011) showed the capability of the narrow-band standard deviation of pressure fluctuations to provide a relation between the granule moisture content and the pressure fluctuation signal for drying of granules.

Regarding the paste drying processes, a few studies explore the bed hydrodynamics. Measurements of bed pressure drop have been employed to study the effect of bed height and gas velocity on this drying process (Reyes *et al.*, 2001; Kudra *et al.*, 2002; Pan *et al.*, 2001). However, the available literature is mainly focused on analyzing the influence of paste composition, liquid loading, bed type and operating conditions on the process performance (Watano *et al.*, 1998; Adamiec, 2002; Tatemoto & Miyazawa, 2011; Freire *et al.*, 2012). In spite of the valuable information provided by these works, a detailed analysis of the hydrodynamics of the paste drying process in a fluidized bed is still required. In order to get some insights into the bed dynamics during drying, a multi-resolution analysis of the pressure signals is carried out in this work.

In this chapter, the effect of the paste drying process on the bed dynamics is studied by means of humidity and temperature measurements (RH-T), as well as through time and frequency analyses of pressure fluctuation signals. Wavelet transform is used to further analyze the different scales present in the pressure signals. Silica sand particles were used both for the paste and as the inert medium due to their non-hygroscopic nature and their common use in fluidization, which will lead to more general results (D'Amore *et al.*, 1979). The batch drying curves obtained from the RH-T analysis identify four

different drying periods as a function of the drying operational conditions. The subsequent multi-resolution analysis of the corresponding pressure fluctuation signals reveals a strong relationship between dynamics and drying kinetics. The effects of the fixed bed height and the possible improvement in the process due to the rotation of the distributor are also investigated.

5.3 Materials and methods

Silica sand particles mixed with water were dried in a fluidized bed, varying the bed aspect ratio, h_b/D, the weight of the paste and its water content. The experimental conditions are given in Table 5.1. The paste was fed to the fluidized bed as a batch over the bed surface. Due to the intensive motion of inert particles, the fluid is rapidly dispersed within the bed. Both the paste and the inert bed particles employed were silica sand particles classified as Group B according to Geldart′s classification (Geldart, 1973). The particle density was measured to be 2645.5 kg/m^3 and its mean diameter was 683 μm.

Table 5.1: Ranges of experimental variables.

variable	operating range
$U_r = U/Umf, r$ [-]	1.6
h_b/D [-]	0.5, 1, 1.5
Paste-sand weight [kg]	0.1, 0.2, 0.35, 0.67
R_{ws} = mass of water/paste-sand weight [-]	0.1, 0.15, 0.20, 0.25
Distributor state	static, rotating

The outline of the experimental apparatus is shown in Figure 5.1. The drying chamber was a cylindrical tube, made of poly methyl methacrylate, with an inner diameter of 192 mm. The air distributor consisted of a perforated plate with 275 orifices of 2 mm in diameter, arranged in a triangular configuration with a pitch of 11 mm. The distributor plate was equipped with an electric motor that allowed its rotation on the horizontal plane. Two types of experiments were carried out: (i) using the rotating distributor with an angular velocity of 100 rpm, and (ii) with static, or conventional, distributor case without rotation.

The fluidization gas was air at ambient conditions and the airflow was measured by a rotameter. The minimum fluidization velocity was measured to be $U_{mf,s} = 0.33$ m/s and $U_{mf,r} = 0.31$ m/s for the static and rotating distributor, respectively. Humidity and temperature of the inlet and exhaust gas flow were

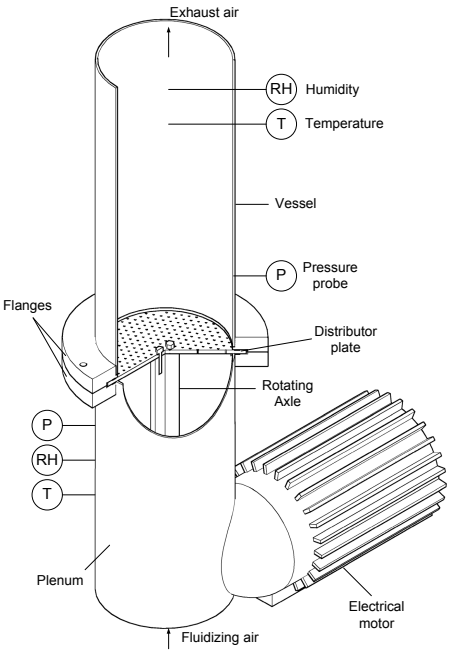

Figure 5.1: Scheme of the experimental setup.

measured but not controlled.

Pressure fluctuations were also measured in the bed. Piezoelectric transducers manufactured by Kistler were placed at the plenum and at $h_b/2$ above the distributor. The dimensions of the pressure probes were 4 mm for the internal diameter and 0.10 m for the length (van Ommen *et al.*, 1999), guarantying an undisturbed transfer of the signal. Multifunctional humidity and temperature transmitters E+E Electronik (model 33PFT-J) were used to characterize the airflow. These transducers were mounted at the plenum chamber and 0.75 m above the distributor. A sampling frequency of $f_s = 400$ Hz was employed to collect the data with a data acquisition system.

5.3.1 Drying mechanism

When paste material is dropped to the inert medium of a fluidized bed, the liquid is dispersed to the neighbouring inert particles due to the mixing promoted by the bubbles. The non-hygroscopic nature of the bed particles enhances the evaporation of the liquid film placed at the surface of the particles (D'Amore *et al.*, 1979). Typically this process, which is dominated by the evaporation mechanism, is defined as the constant-rate period. During the constant-rate

period, the particle surface is saturated with water and in equilibrium with the air adjacent to the particle surface. However, as Reay & Baker (1985) suggested, the constant drying rate period could be rapid enough not to be observed. The interparticle forces that appear on the surface of the wet particles tend to form a coating layer of dry particles around the sticky particles, hindering the vaporization of water from the particle surface (Lee & Kim, 1993). Thus, the rapid mixing of the liquid and the non-hygroscopic nature of the bed particles prevent the appearance of the constant-rate period (Shin *et al.*, 2000). For these reasons, when the constant-rate period is not shown, it is characterized by the maximum drying rate (R_d), which is equal to the drying rate of the constant drying rate period.

The constant-rate period is followed by the falling-rate period. Diffusion of water from the interior to the surface of the agglomerates determines the drying rate at this stage. Thus, the drying rate is determined by the size and the diffusion coefficient of the agglomerates. As the coating layer is gradually dried, the agglomerate becomes fragile and friable, reducing the agglomerate size and improving the fluid dynamic conditions of the bed. For the overall drying process, temperature and humidity data can be used for an on-line estimation of the amount of water removed during the tests (Δm). This variable is related to the total mass of water dried. The moisture balance for the solids can be written as

$$\frac{dm}{dt} = \frac{A_t U M_v}{R}\left(\frac{p_{v,s}(T_{out})RH_{out}}{T_{out}} - \frac{p_{v,s}(T_{in})RH_{in}}{T_{in}}\right) \tag{5.1}$$

where A_t is the cross sectional area of the bed, U the air velocity, M_v the molecular weight of water, R the universal gas constant, T the measured temperature, RH the measured relative humidity and $p_{v,s}$ the saturated vapor pressure of water, which was estimated by the Clasius-Clapeyron relation. By using this variable, the drying time ($t_{95\%}$) can be defined as the time needed to remove 95% of moisture from the paste.

5.3.2 Pressure analysis

Wavelet analysis allows to transform a signal in the time domain to the time-frequency domain (Kulkarni *et al.*, 2001; Yang & Leu, 2008). Thus, wavelet analysis is similar to the windowed Fourier transform (Zhao & Yang, 2003; Sasic *et al.*, 2006). The main difference with the Fourier analysis is the narrow band at higher frequencies and broad band at low frequencies of the wavelet

basis function. Wavelets are generated by the dilation and the translation of the orthogonal father wavelet function ϕ and the mother wavelet function ψ as follows:

$$\phi_{j,k}(t) = 2^{-j/2}\phi\left(\frac{t-2^j k}{2^j}\right), j, k\epsilon I \tag{5.2}$$

$$\psi_{j,k}(t) = 2^{-j/2}\psi\left(\frac{t-2^j k}{2^j}\right), j, k\epsilon I \tag{5.3}$$

with time shift $k = 1, 2,..., N/2^j$ and level $j = 1, 2,..., J$. The transform in a discrete signal can be carried out by the discrete wavelet transform. Basically, the procedure consists of decomposing the discrete signal, $x(t)$, into an ordered set of orthogonal approximation and detail functions, $S_{j,k}(t)$ and $D_{j,k}(t)$ respectively. Thus, the wavelet transform of $x(t)$ can be obtained by:

$$s_{j,k}(t) = \int x(t)\phi_{j,k}(t)dt \tag{5.4}$$

$$d_{j,k}(t) = \int x(t)\psi_{j,k}(t)dt \tag{5.5}$$

where $s_{j,k}$ and $d_{j,k}$ are called the approximation and detail coefficients respectively. Roughly speaking, $s_{j,k}$ mainly represents the smooth behaviour at the coarser scale and $d_{j,k}$ represents the details at the finer scales. Consequently, the original signal can be expressed as the summation of the approximations and the details in a multi-step manner as follows:

$$x(t) \approx S_J(t) + D_J(t) + D_{J-1}(t) + ... + D_1(t) \tag{5.6}$$

The energy of signals $S_J(t)$ and $D_J(t)$ are defined as:

$$E_J^S = \sum_{t=1}^{N} |S_J(t)|^2 \tag{5.7}$$

$$E_J^D = \sum_{t=1}^{N} |D_J(t)|^2 \tag{5.8}$$

Based on the orthogonality and the energy conservation of wavelet transform, the total energy of $x(t)$ can be calculated using Eq. (5.9). In this study, second-order Daubechies′ wavelet (Daublet2) was used as wavelet function to

perform a multi-resolution analysis on the pressure fluctuation signals. The normalized energy of the individual approximation, e_J^S, and detail sub-signals, e_J^D, can be calculated dividing by the energy of $x(t)$

$$E = \sum_t |x(t)|^2 = E_J^S + \sum_{j=1}^{J} E_j^D \tag{5.9}$$

$$e_J^S = \frac{E_J^S}{E} \tag{5.10}$$

$$e_J^D = \frac{E_J^D}{E} \tag{5.11}$$

In order to compare the drying time obtained using both the humidity and the pressure signal analyses, it is necessary to (i) set the monitoring tools that describe the fluidization quality, and (ii) define a control state for these variables. For the former, pressure fluctuation signals were analyzed in both the time and frequency domains. Time domain measurements are commonly employed in many applications due to their easy computation. In this way, the standard deviation, σ, and the average cycle time, t_{av}, of the pressure signals were computed. These variables have shown their capability of detecting phenomena that can affect the fluidization quality, i.e. segregation, channelling or bed defluidization (Briens & Briens, 2002; Gómez-Hernández *et al.*, 2012; van Ommen *et al.*, 2004; Stappen, 1996).

The energy contained within the power spectra of the pressure signals was employed to describe the frequency domain (Johnsson *et al.*, 2000). The cumulative energy function of the power spectrum density (PSD) was approached to the Student′s t-distribution function to obtain the three frequency regions in which the frequency domain was divided. The region of coincidence between the theoretical and the experimental cumulative energy distributions fixed the cut-off frequencies between the regions. The procedure to compute the energy of the frequency regions is described in detail in Chapter 3, and the results obtained employing this approach are summarized in Table 5.2. The energy contained in each region is related to different phenomena. E_{WB1} represents the larger structures of the bed, E_{WB2} is related to the bulk dynamics of the bed, and E_{WB3} includes the high frequency phenomena such as the formation of channels .

Depending on the experimental conditions, the paste drying process may change the fluidization dynamics. The definition of a control zone for the monitoring tools employed is needed to establish whether the drying process influenced the fluidization behaviour or not. The Statistical Process Control

Table 5.2: Computational settings for the frequency division method.

PSD	Fitting	Standard error $\hat{\sigma}_e$ [-]	Bed aspect ratio [-]	Cut-off frequencies [Hz]	
				f_{cI}	f_{cII}
Welch method $N_s = 4096$	Student′s t-distribution	0.07	0.5	2.94	3.42
			1	2.35	2.73
			1.5	1.76	2.15

Table 5.3: Settings for the SPC implementation.

Reference time series length [s]	Variable	Moving window sizes [s]	Statistic distribution	UAL	LAL
240	σ	25	Normal	$\bar{X} + 3\sigma$	$\bar{X} - 3\sigma$
	t_{av}	35			
	E_{WB1}				
	E_{WB2}	50			
	E_{WB3}				

(SPC) theory was applied to all the monitoring tools considered in this chapter. The followed procedure was described in Chapter 4. A control zone was established between the upper and lower action limits, UAL and LAL, for the standard deviation, average cycle time and wide band energy of the frequency regions t-I, t-II and t-III. The time length of the reference signal, the window size to compute each variable and the statistic distribution used to estimate the control charts are described in Table 5.3.

5.4 Results and discussion

The drying tests started with the bed working with the static distributor or with the rotating distributor. The operating conditions were previously described in Table 5.1. During the tests, the paste was dropped over the bed surface and temperature, humidity and pressure fluctuation signals were measured until the drying process finished. Different methodologies were employed to analyze the paste drying tests. First of all, the visual observation of the experiments led to establish three fluidization states: fluidized, maldistributed and defluidized. These states determined the effect of the paste drop-off in the fluidization quality during a short time after the beginning of the drying process. The visual classification of the tests was related to the humidity and temperature measure-

ments. Thus, these measurements were analyzed using Eq. (5.1) to estimate the drying rate and the amount of moisture removed during the drying.

Furthermore, the results obtained with the drying analysis were studied performing a multi-resolution approach of the pressure signals. In this way, the effect of the drying process on the bed dynamics is studied. The wavelet results were employed to implement a SPC monitoring system to determine whether or not it is possible to describe the drying process using the pressure fluctuation signals.

5.4.1 Drying process analysis

The influence of the paste drop-off on the bed dynamics was studied by the visual inspection of the tests. A scheme of this effect is presented in Figure 5.2. Previously to the paste drop-off, the bed was working either with the static or the rotating distributor without agglomerates, as shown in Figure 5.2-a. Depending on the drying conditions, the paste drop-off may change the fluidization quality to:

- Fluidized state: the paste was homogeneously distributed and formed small agglomerates that could be fluidized, as sketched in Figure 5.2-b, and thus, negligible changes of the fluidization dynamics were observed.

- Maldistributed state: greater agglomerates were produced, which caused the bed segregation and the formation of small channels over the distributor plate, as described in Figure 5.2-c.

- Defluidized state: stable channels were formed throughout the whole bed, as described in Figure 5.2-d, preventing the bed fluidization.

This classification of the experiments was related to the temperature and humidity measurements using the drying analysis explained above. In this way, Figure 5.3 shows the changes in the drying rate, R_w, and the percentage of water dried, Δm, with time for the three fluidization states observed during the experiments. Also, this figure shows a comparison of both the static and rotating distributor tests for $h_b/D = 1.5$.

Focusing on the analysis of the drying rate and the amount of water removed, the changes in slope of R_w reveal the existence of common drying periods as a function of the bed state. These periods are a characteristic of the experiments included in each state, and they are defined by:

- Period 1: Constant-rate

During the initial period of drying, the sample was dispersed within the inert bed particles. As discussed above, the constant-rate period was too short

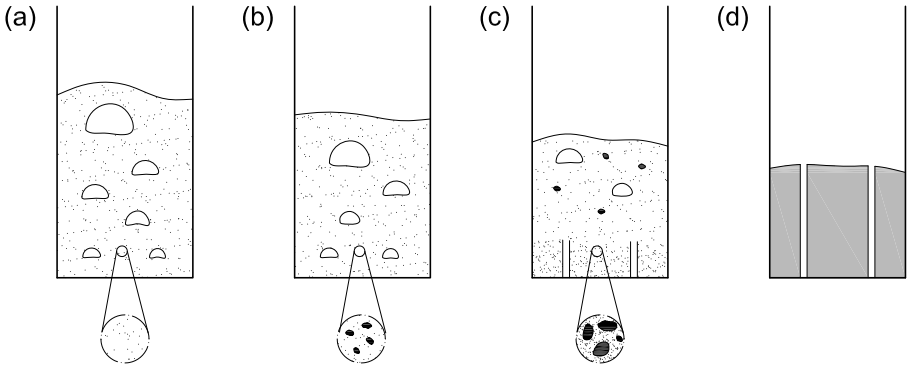

Figure 5.2: Scheme of the fluidization states: (a) Nominal fluidization. (b) Fluidized state. (c) Maldistributed state. (d) Defluidized state.

to be observed, and due to that, this zone is characterized by the maximum drying rate, R_d. The proper mixing between the paste and the inert particles caused the removal of a large amount of water during a short period of time, typically around 20-30 s. This water was mainly dried by the vaporization of liquid from the surface of the particles.

This period was detected in the three fluidization states (Figure 5.3-a/b/c), but depending on the type of liquid absorption by the inert medium the bed dynamics could remain fluidized or change towards to a maldistributed state or even to the complete bed defluidization. The transition to one of these regimes depends on a change in the slope of R_d.

- Period 2: Transition

The dispersed wet particles were covered by a layer of inert particles forming agglomerates of different sizes. Two opposite effects appeared at this stage. On the one hand, the agglomerates tended to settle over the distributor at the dead zones between the holes, reducing the mixing rate and promoting the appearance of channels. On the other hand, as these agglomerates were dried, the cohesive forces were less intensive and the agglomerates become fragile. The particle collisions during fluidization could reduce the size of these agglomerates and thus, the drying time. In any case, the diffusion from inside the agglomerates was the governing drying mechanism. This period typically lasts from 1 to 5 min, and typically appears when the bed of inert particles cannot support the sample to dry. The maldistributed state is shown in Figure 5.3-b by a linear reduction of the drying rate, whereas when the bed is defluidized, some fluctuations caused by big channels can be seen in Figure 5.3-c.

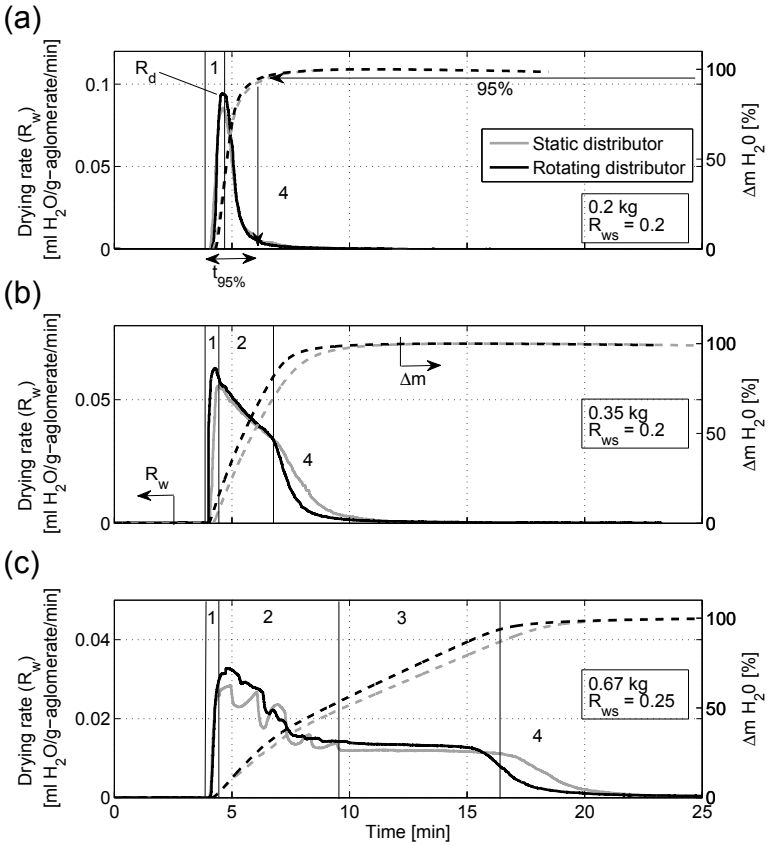

Figure 5.3: Drying rate (R_d), on the left axis, and percentage of water dried (Δm), on the right axis, for static and rotating tests for the: (a) Fluidized state. (b) Maldistributed state. (c) Defluidized state.

- Period 3: Defluidized

This period was shown only when the bed was completely defluidized. Big channels appeared close to the vessel wall with some bubbles at the bed surface. Most of the air flowed through the channels, and the diffusion of water was lower than in the previous zone. When the agglomerates located over the distributor plate were sufficiently wet to contain free moisture, the drying rate showed constant values as presented in Figure 5.3-c. Large drying times and low drying rates characterize this period.

- Period 4: Falling-rate

Once 80-90% of water was removed, the bed reached the fluidization quality previous to the beginning of the drying process. No channelling or dead zones

were observed although small agglomerates were still present inside the bed. At this stage, the drying time, $t_{95\%}$, is defined as the time needed to remove 95% of water from the paste. This period was observed in Figure 5.3-a/b/c for the three fluidization states and ranges from 2 to 5 min.

Concerning the effect of the distributor rotation, higher maximum drying rates were obtained for all the fluidized states except at the end of the drying process, which is the Period 4. Higher R_d values point to a better mixing of the paste within the bed, which means that the rotating distributor enhances the evaporation rates at the beginning of the drying process. Moreover, the shape of the drying rate for the rotating distributor changed faster (and without fluctuations) than for the static distributor when the bed was maldistributed or defluidized, as shown in Figure 5.3-b/c. This effect is explained by the breakage of the agglomerates located over the distributor, which also results in a greater percentage of water dried, and thus, the drying time needed is reduced when employing the rotating distributor.

The experiments considered in Table 5.1 are classified according to the three fluidization states found after the drying analysis. Following the results of the visual classification sketched in Figure 5.2, Figure 5.4 shows the classification of the experiments in the three fluidization states as a function of the mass ratio water-sand present in the bed. These results were obtained for $U_r = 1.6$ varying the bed aspect ratio $h_b/D = 0.5$, 1 and 1.5. Furthermore, the maximum drying rate R_d and the drying time $t_{95\%}$ are also studied.

The visual classification of the tests led to establish vertical limits in Figure 5.4-a1/a2/a3 for the bed aspect ratios considered. The value of the limits decreased with the increase of the bed aspect ratio, as shown comparing Figure 5.4-a1 with Figure 5.4-a2 or Figure 5.4-a3. These limits were also plotted in Figure 5.4-b1/b2/b3 for the maximum drying rate and in Figure 5.4-c1/c2/c3 for the drying time to determine if similar results to the visual classification can be obtained using these three variables.

Regarding the maximum drying rate, high R_d values were obtained for the fluidized state, which were followed by lower values when the bed was maldistributed and minimum values for the defluidized state. As shown in Figure 5.4-b1/b2/b3, R_d values of the maldistributed state were similar to the values of the defluidized state. Therefore, it is difficult to differentiate between maldistributed and defluidized states using the R_d results. Nevertheless, it was possible to identify the fluidized state by the high R_d values.

The drying time, $t_{95\%}$, obtained using the RH-T analysis is presented in

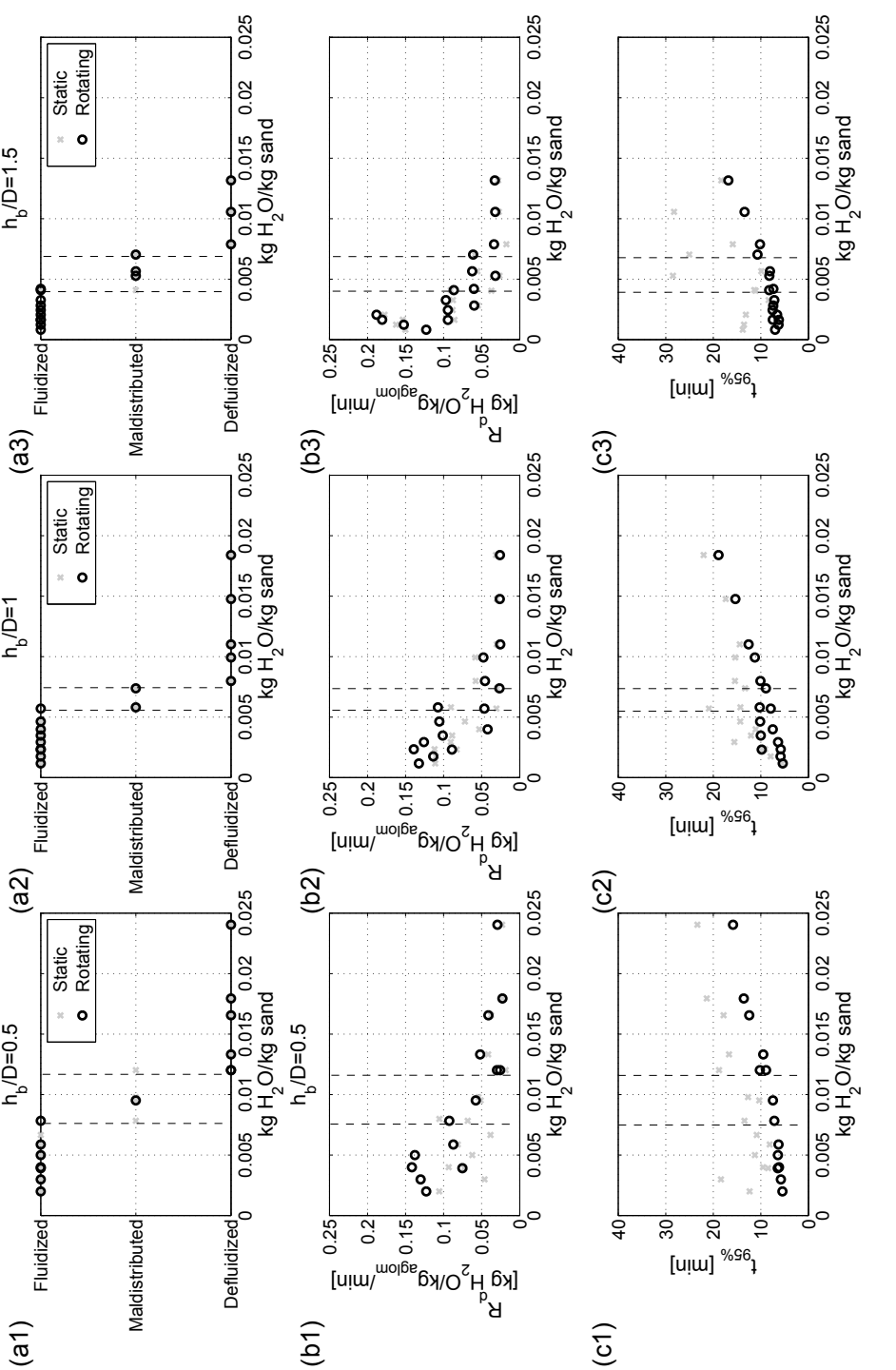

Figure 5.4: Tests classification (a), maximum drying rate (b) (R_d) and drying time (c) ($t_{95\%}$) for the bed aspect ratios of: (1) $h_b/D = 0.5$, (2) $h_b/D = 1$ and (3) $h_b/D = 1.5$.

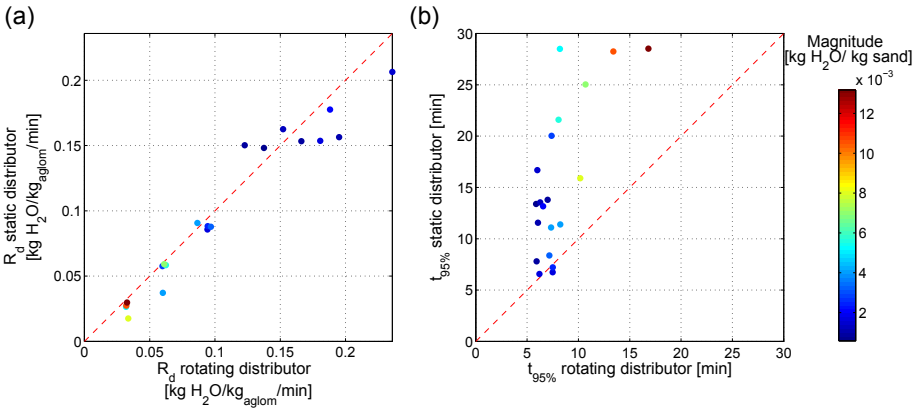

Figure 5.5: Comparison between static and rotating distributor tests for $h_b/D = 1.5$. (a) Maximum drying rate (R_d). (b) Drying time ($t_{95\%}$)

Figure 5.4-c1/c2/c3. In this case, a discrimination between the three states was not possible since the drying time represents a global measurement of the entire process. Thus, the drying time includes all the transition periods described in Figure 5.3, while R_d only reflects the influence of the paste drying on Period 1. On the other hand, it is worth to note the wide range of $t_{95\%}$ obtained for the static distributor tests for all the bed heights considered.

The effect of the rotating distributor on the visual classification of the runs is not clear as shown in Figure 5.4-a1/a2/a3. In contrast, improvements in R_d and $t_{95\%}$ are observed in Figure 5.4 when the distributor is rotating. Higher values of R_d are shown for shallow beds when the bed remains in the fluidized state, due to the mixing improvement caused by the distributor rotation, in agreement with Sobrino *et al.* (2009). Also, lower and more homogeneous drying times were obtained for all bed heights and fluidization states.

A further analysis of the rotating distributor influence for $h_b/D = 1.5$ is presented in Figure 5.5. Figure 5.5-a shows R_d for both the static and the rotating distributor tests in the vertical and horizontal axes, respectively. Furthermore, the data points are plotted in different colors as a function of the water-sand mass ratio in the bed. A similar comparison is shown in Figure 5.5-b employing the drying time, $t_{95\%}$, obtained in both cases.

Concerning R_d, most of the values obtained are similar for both the static and the rotating distributors, as shown in Figure 5.5-a. Thus, no significant influence is shown for deep beds when the distributor is rotating. This confirms the results showed in Figure 5.4, where the rotating distributor effect on R_d

decreased for larger bed heights. On the other hand, the classification of the fluidization states based on R_d can be also detected in Figure 5.5-a, showing lower R_d values at high water-sand mass ratios, corresponding to the defluidized state, and higher R_d values for low water-sand mass ratios at the fluidized state.

Clear differences between both the static and the rotating distributor tests were obtained for the drying time, as can be seen in Figure 5.5-b. As the water-sand mass ratio was increased, higher drying times were needed using the static distributor. The time reduction produced by the rotating distributor is caused by the breakage of channels and agglomerates located over the distributor. Thus, since this region is of great importance in the drying process (Mujumdar, 2006), the drying performance is substantially improved even for deep beds when the distributor rotates.

5.4.2 Multi-resolution analysis

The wavelet transform was applied to the pressure fluctuation signals in order to further understand the characteristics of each drying period. The decomposition level was studied in Figure 5.6. This figure shows the scalogram of the percentage of energy for each wavelet coefficient with the time. As the coefficient level is increased, the energy changes up to around level 10, remaining constant above this value. Therefore, the decomposition level was set to 10 and each pressure fluctuation signal was decomposed into 11 sub-signals. Thus, ten detail sub-signals (D1-D10) and one approximation sub-signal (S10) were obtained for the different bed aspect ratios studied. Figure 5.7 shows the original pressure signal and the sub-signals in which it was decomposed. Each sub-signal was plotted with the same scale. Slight differences between $h_b/D = 0.5$ and $h_b/D = 1.5$ cases were found at sub-signal D7 (Figure 5.7-a/c). Since the central frequency of each sub-signal is described by $f_s/2^{J+1}$, the central frequency of D7 corresponds to 3.1 Hz which is close to the bubbling frequency of the bed, which changes when the bed aspect ratio is increased (Baskakov *et al.*, 1986).

The relative energy of each sub-signal was calculated using Eq. (5.11) to qualitatively investigate the effect of the drying process on the pressure fluctuations. Figure 5.8 shows the energy distribution of the detail sub-signals for the nominal state (prior to starting the drying process) and for the three fluidization states described above. Also, these fluidization states are presented according to the zones obtained in the drying analysis in order to decide whether or not they present common features in their hydrodynamic behavior.

For the nominal state, the energy is mainly distributed between D6 and D8

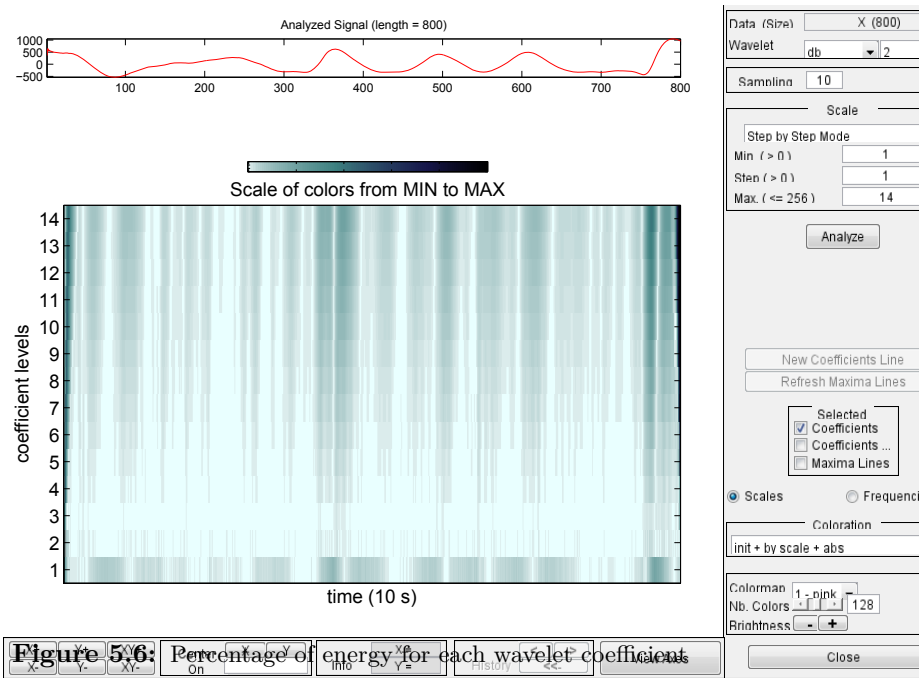

Figure 5.6: Percentage of energy for each wavelet coefficient

since these sub-signals cover the main frequencies of interest in a fluidized bed (van Ommen *et al.*, 2011). Thus, the comparison for each period to the nominal state leads to:

- Period 1 (Figure 5.8-a):

The energy of the details for the three regimes focuses mainly on D6-D8 while low and high frequencies remain similar to the nominal state, almost unaffected by the paste drop-off. The short length of this period (around 30 s) made it difficult to identify the formation of agglomerates or channels that can change the energy distribution. Thus, this short period presents a similar dynamic behavior for all the regimes, since the paste was distributed within the fluidized bed.

- Period 2 (Figure 5.8-b):

This period is present only in the maldistributed and defluidized operating conditions. Comparing to the energy distribution of the nominal case, there is a substantial energy transfer to higher frequencies (D6 and D5) while the characteristic energy of D7 decreases for both the maldistributed and the defluidized states. This energy transference to higher frequencies reveals that the agglomerates formed were settled over the distributor, forming channels, as stated in Chapters 2 and 3. However, some differences appear between the maldistributed and the defluidized energy distributions. For the maldistributed state, there is an energy transfer around 10% mainly to D6 and to a lesser extent to D5. Nevertheless, for the defluidized state, the energy loss by D7 is rather transferred to the higher frequencies of D5. Moreover, the channels also

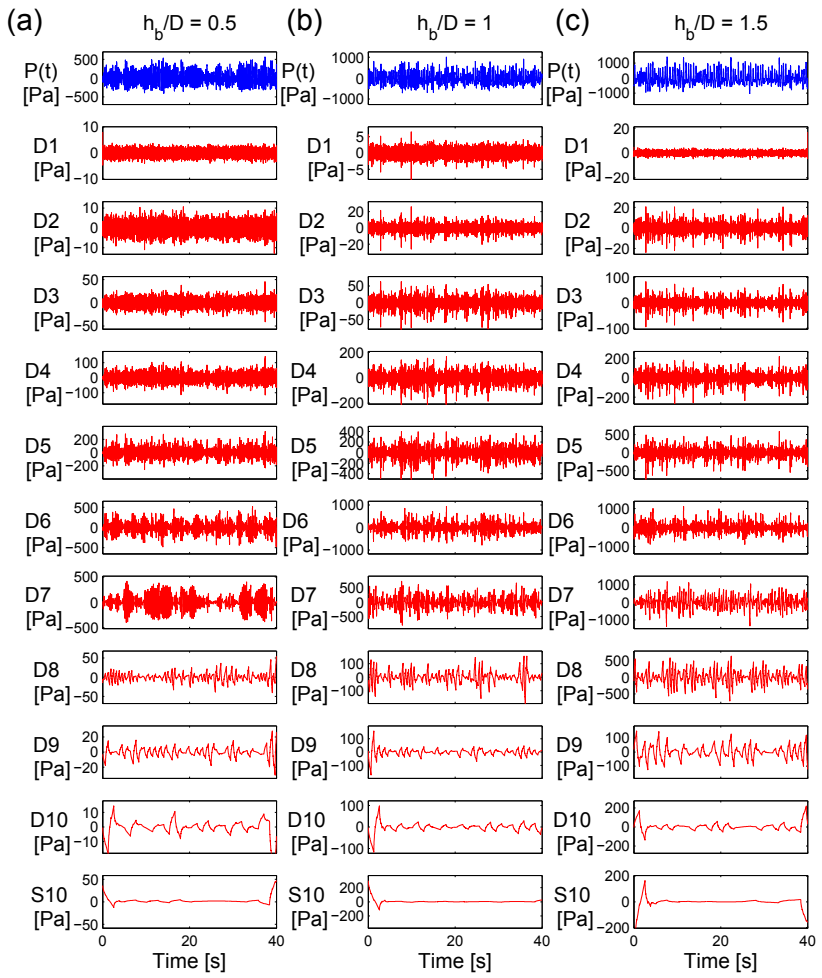

Figure 5.7: Multi-resolution analysis of pressure fluctuations for different bed aspect ratios. (a) $h_b/D = 0.5$. (b) $h_b/D = 1$. (c) $h_b/D = 1.5$.

caused a significant rise in the energy of the low frequencies (D9).

- Period 3 (Figure 5.8-c):

Period 3 only appeared in the defluidized state. Compared to the nominal state, it can be observed that the frequency details D5 and D6 present higher energies due to the presence of channels. Moreover, as a result of such a different energy distribution, the long term behavior of the bed was influenced, and thus, the drying performance was reduced.

- Period 4 (Figure 5.8-d):

According to the energy distribution shown during the falling rate period,

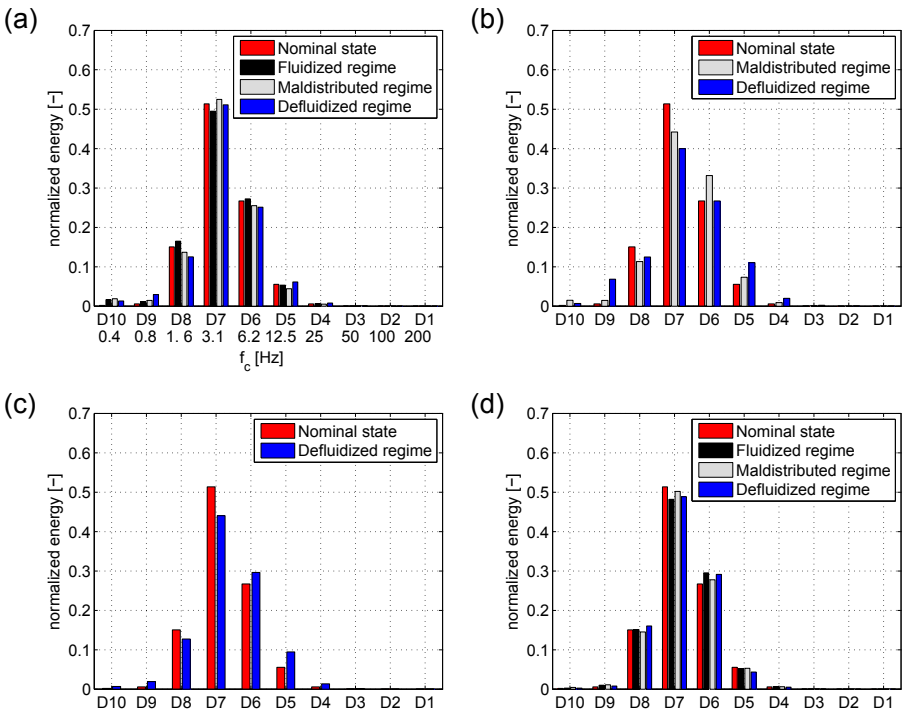

Figure 5.8: Energy of wavelet sub-signals in the drying periods for different fluidization states. (a) Period 1. (b) Period 2. (c) Period 3. (d) Period 4.

the three regimes are similar to the nominal state. Thus, the bed was properly fluidized with the presence of a small amount of agglomerates.

As a result of the multi-resolution analysis, the bed dynamics were proved to be affected by the drying process. The transference of energy between the different scales of the bed dynamics for the maldistributed and defluidized states identified the channels appearance, and the modification of the long-term structures of the bed (i.e. the bubble pattern).

5.4.3 Dynamics of pressure fluctuations

The study of the pressure fluctuation signals through the multi-resolution analysis permitted the study of the drying process as a function of the four drying periods found previously. Thus, it is possible to elucidate the bed dynamics by monitoring the drying performance using the RH-T analysis. In this sense, a question arises about whether or not the characteristic parameters of the drying process (i.e. the drying time) can be obtained from the bed dynamics.

The comparison of the wavelet results with the drying time obtained using the RH-T analysis is not straightforward. To deal with this difficulty, a SPC monitoring scheme was applied to the pressure signals. In this way, a control zone was defined for all the employed variables, which allows the definition of the dynamic time (t_d) as the time elapsed between the loss and the recuperation of the control state.

The standard deviation, σ, average cycle time, t_{av}, and wide band energy of Region t-III, E_{WB3}, Region t-II, E_{WB2}, and Region t-I, E_{WB1}, were used to study the pressure signals. The experiments presented in Figure 5.3 for the static distributor case are analyzed. Furthermore, pressure measurements in the plenum and at $h_b/2$ were studied to analyze the effect of the pressure probe location. Finally, the dynamic time was compared to the RH-T results.

First of all, the experiments with low water-sand mass ratio, classified in the fluidized state, were studied. Figure 5.9 shows σ, t_{av}, E_{WB3}, E_{WB2} and E_{WB1} for the fluidized regime described in Figure 5.3-a. These monitoring tools are plotted in control charts, where two horizontal lines establish the bed control state, UAL and LAL. Furthermore, the drying time $t_{95\%}$ was also plotted in Figure 5.9. In this test, neither the plenum nor the $h_b/2$ results detected the start of the drying process. Only E_{WB3} showed values around the UAL, but with a delay after finishing the drying process. Therefore, no useful information for the estimation of the drying time can be obtained from the control charts. The high mixing degree of the bed homogeneously dispersed the sample, and due to that, the bed dynamics were not affected.

The variation of the monitoring tools when the bed is at the maldistributed regime was plotted in Figure 5.10. The beginning and end of the drying process can be clearly detected with the standard deviation of both the plenum and the $h_b/2$ pressure signals, as shown in Figure 5.10-a1/a2. The decrease of the standard deviation values points to a reduction of the fluidization quality, making possible to measure the recuperation time, t_r. Significant differences were found for t_{av}, E_{WB3} and E_{WB2} comparing the plenum and the $h_b/2$ results. The average cycle time and frequency monitoring tools of the plenum transducer present lower amplitudes in Figure 5.10-b1/c1/d1 than those of the $h_b/2$ sensor, shown in Figure 5.10-b2/c2/d2, which results in a poor estimation of the recuperation time. In this way, negligible fluctuations around the action limits were detected by the plenum probe after the beginning of the drying process. In contrast to the plenum data, the signal at $h_b/2$ identified the presence of channels inside the bed by the out of the control state (Figure 5.9-b2/c2/d2)

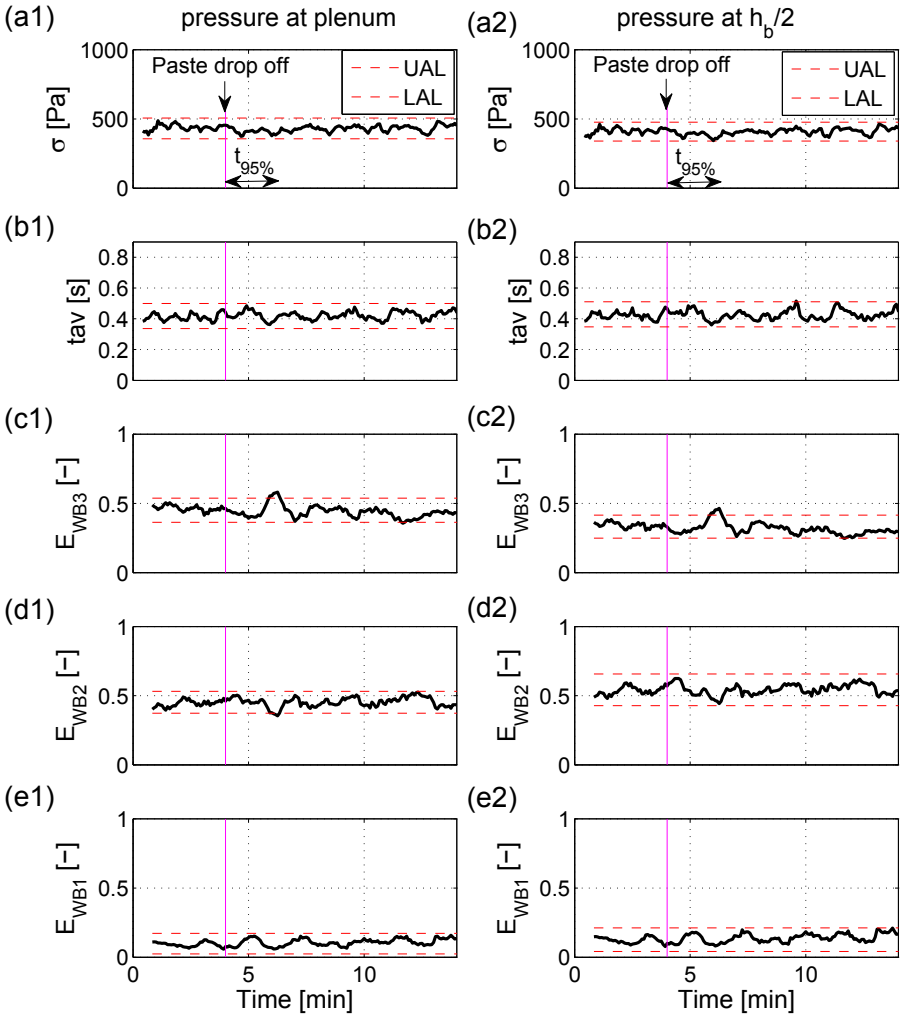

Figure 5.9: SPC results of the fluidized state for (a) the standard deviation (σ), (b) average cycle time (t_{av}), (c) wide band energy of Region t-III (E_{WB3}), (d) Region t-II (E_{WB2}) and (e) Region t-I (E_{WB1}) for (1) pressure sensor located at the plenum, and (2) pressure sensor located at $h_b/2$.

facilitating the estimation of the recuperation time.

Finally, the defluidized regime was successfully detected by both pressure transducers, as can be observed in Figure 5.11. In this test, which corresponds to the static distributor experiment, shown in Figure 5.3-c, the bed was completely defluidized after the paste drop-off. Large channels through the bed were visually observed.

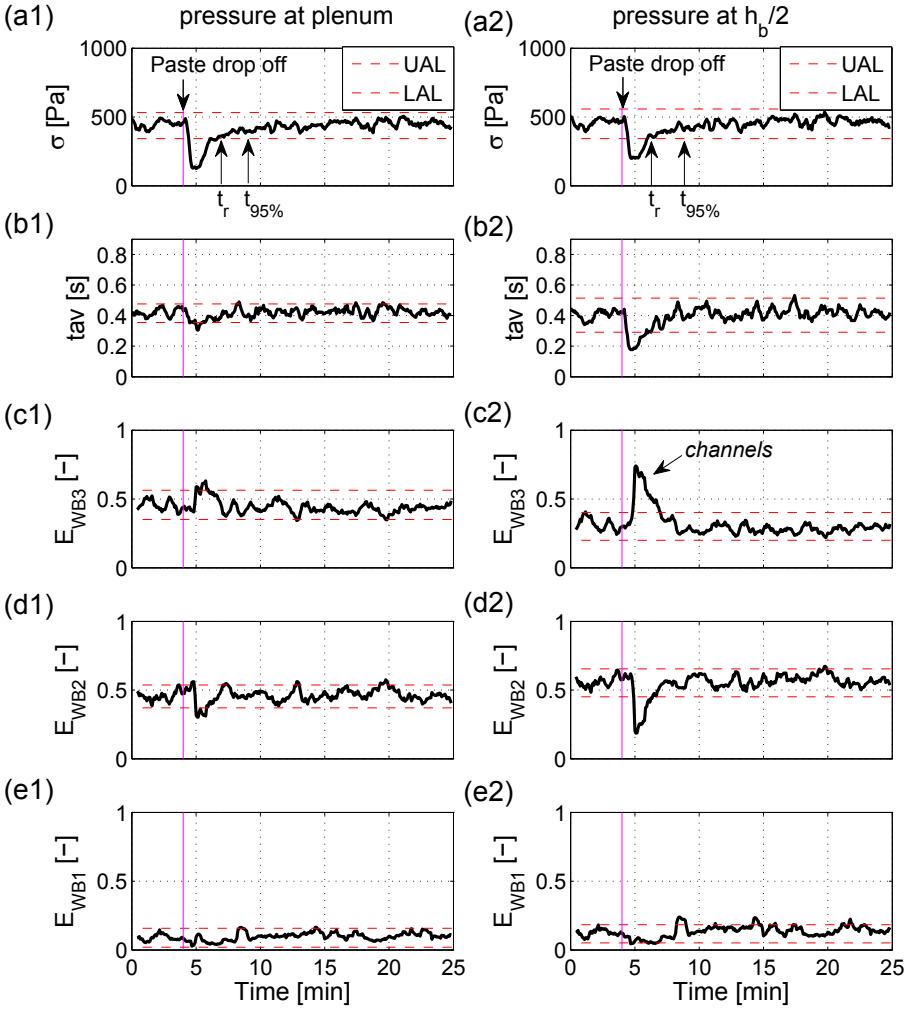

Figure 5.10: SPC results of the maldistributed state for (a) the standard deviation (σ), (b) average cycle time (t_{av}), (c) wide band energy of Region t-III (E_{WB3}), (d) Region t-II (E_{WB2}) and (e) Region t-I (E_{WB1}) for (1) pressure sensor located at the plenum, and (2) pressure sensor located at $h_b/2$.

The bed defluidization was detected by a low plateau of the standard deviation and the average cycle time of both pressure transducers signals. E_{WB3} and E_{WB2} values were also out of the control state as shown in Figure 5.11. In the defluidized state, as for the maldistributed case, all the variables can be used to characterize the drying process by the recuperation time.

As shown in Figures 5.10 and 5.11, the most sensible variables were the

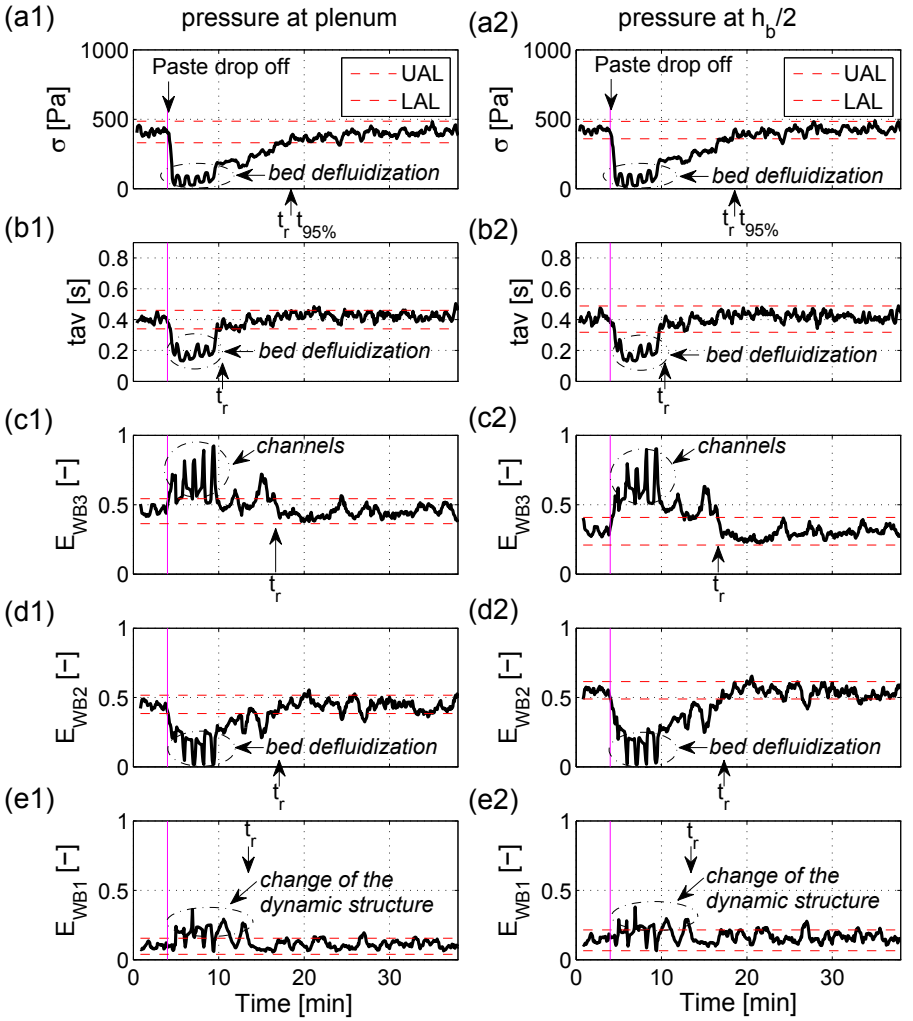

Figure 5.11: SPC results of the defluidized state for (a) the standard deviation (σ), (b) average cycle time (t_{av}), (c) wide band energy of Region t-III (E_{WB3}), (d) Region t-II (E_{WB2}) and (e) Region t-I (E_{WB1}) for: (1) pressure sensor located at the plenum, and (2) pressure sensor located at $h_b/2$.

standard deviation, average cycle time and wide band energy of Region t-III. Thus, these variables together with the SPC scheme were employed to obtain the time needed to recover the fluidization quality, t_r. In this way, Figure 5.12 compares the times obtained using both the RH-T analysis, $t_{95\%}$, and the study of the pressure signals, t_r.

For the shallow bed with the static distributor presented in Figure 5.12-a, a

high correlation is shown for the times estimated with the RH-T analysis and the SPC approach of σ, t_{av}, and E_{WB3}. By comparing the rotating and static distributor tests shown in Figure 5.12-a/b, lower drying times are shown due to the rotating effect on the region next to the distributor. Deeper beds with the static distributor, which are presented in Figure 5.12-c/d, need more time to finish the drying process than to recover the bed dynamics defined by the control state. Furthermore, it is worth to point out the different recuperation times obtained depending on the variable used for the static distributor tests. This informs of a heterogeneous recuperation process. On the other hand, similar drying and dynamic times were obtained for the rotating distributor runs.

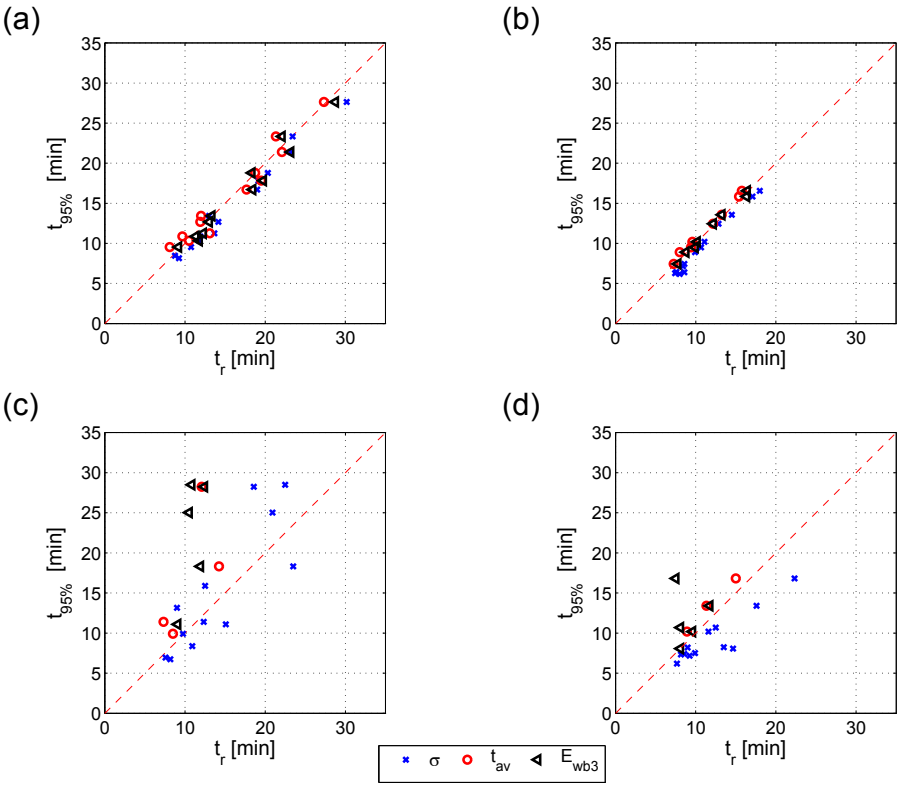

Figure 5.12: Comparison between the drying times estimated with RH-T and the recuperation times estimated with the SPC approach. (a) Static distributor ($h_b/D = 0.5$). (b) Rotating distributor ($h_b/D = 0.5$). (c) Static distributor ($h_b/D = 1.5$). (d) Rotating distributor ($h_b/D = 1.5$).

5.5 Conclusions

Paste drying tests with inert particles as inert medium were studied in a bed equipped with a rotating distributor. The process performance is analyzed using humidity and temperature measurements and pressure fluctuation signals. The paste drying tests can be grouped into: i) fluidized: with negligible changes of the bed dynamics, ii) maldistributed: showing small channels over the distributor plate and iii) defluidized: producing stable channels throughout the bed.

From the drying analysis of the humidity and temperature measurements, the visual classification of the paste drying tests can be also done studying the R_d values. Four characteristic periods are identified for paste drying. Depending on the water-sand mass ratio, the paste can be homogeneously dispersed within the bed particles showing a smooth decay of the drying rate or can form dead zones over the distributor that maintained a constant drying rate. In any case, the diffusion mechanism from inside small agglomerates or big dead zones is the governing drying mechanism.

From the multi-resolution results it can be concluded that the paste drying can affect the low and high frequency details (D9 and D5, respectively) of the pressure signal when the bed state changes towards defluidization, or only the high frequency detail (D5) if the bed is at the maldistributed state. Nevertheless, as tests of the fluidize state barely influences the bed dynamics, the use of the pressure signals to control the drying process is not recommended.

Moreover, the SPC approach allowed the comparison of the humidity and temperature analysis with the bed dynamics by defining the recuperation time. Similar recuperation and drying times are obtained for shallow beds. However, as the bed height is increased, more time is needed to finish the drying process than to recover the fluidization quality for the static distributor tests.

A comparison between the static and the rotating distributor tests showed clear benefits for the operation with the rotating distributor: it increases the values of R_d, reduces the drying time and homogenizes the recuperation of the bed dynamics for all the bed aspect ratios considered. This is caused by the structuring effect of the rotating distributor on the bed dynamics and by the improvement of the breakage of agglomerates and channels located near the distributor plate.

Notation

A_t	Cross sectional area of the bed [m^2]
$d_{j,k}$	Detail coefficient [-]
D	Inner diameter of big fluidized bed vessel [m]
$D_{j,k}$	Detail function
e_J^D	Normalized energy of the detail sub-signal [-]
e_J^S	Normalized energy of the approximation sub-signal [-]
E_J^D	Energy of the detail sub-signal
E_J^S	Energy of the approximation sub-signal
E_{WB}	Wide band energy [-]
f	Frequency [Hz]
f_c	Central frequency [Hz]
f_{cI}	Lower cut-off frequency [Hz]
f_{cII}	Upper cut-off frequency [Hz]
f_s	Sampling frequency [Hz]
h_b	Fixed bed height [m]
J	Decomposition level [-]
H_1	Alternative hypothesis
M_v	Molecular weight of water vapour [g/mol]
m	Mass of water [kg]
N_s	Number of samples [-]
$p_{v,s}$	Saturated vapour pressure of water [Pa]
R	Universal gas constant [J/(molK)]
R_d	Maximum drying rate [ml H_2O/g-agglomerate/min]
R_w	Drying rate [ml H_2O/g-agglomerate/min]
R_{ws}	Water-sand mass ratio [-]
RH	Relative humidity [%]
$s_{j,k}$	Approximation coefficient [-]
$S_{j,k}$	Approximation function
t	Time [s]
t_{av}	Average cycle time [s]
t_r	Recuperation time of the bed dynamics [s]
$t_{95\%}$	Time needed to remove 95% of moisture [s]
T	Temperature [K]
U	Gas velocity [m/s]
U_r	Relative gas velocity [-]

$U_{mf,r}$	Minimum fluidization velocity with rotating distributor [m/s]
$U_{mf,s}$	Minimum fluidization velocity with static distributor [m/s]
$x(t)$	Signal
$\bar{X}$	Process mean value

Greek symbols

Δm	Percentage of dried water [%]
ϕ	Father wavelet function
ψ	Mother wavelet function
σ	Standard deviation
$\hat{\sigma}$	Standard error
$3-\sigma$	Probability limits

Abbreviattions

LAL	Lower action limit
PSD	Power spectra density
SPC	Statistical Process Control
UAL	Upper action limit

References

Adamiec, J. 2002 Drying of waste sludges in a fluidized bed dryer with a mixer. *Drying Technology* 20 (4-5), 839–853.

Akhavan, A., van Ommen, J. R., Nijenhuis, J., Wang, X. S., Coppens, M.O. & Rhodes, M. J. 2009 Improved drying in a pulsation-assisted fluidized bed. *Industrial & Engineering Chemistry Research* 48 (1), 302–309.

Baskakov, A. P., Tuponogov, V. G. & Filippovsky, N. F. 1986 A study of pressure-fluctuations in a bubbling fluidized-bed. *Powder Technology* 45 (2), 113–117.

Briens, L. & Bojarra, M. 2010 Monitoring fluidized bed drying of pharmaceutical granules. *Aaps Pharmscitech* 11 (4), 1612–1618.

Briens, L. A. & Briens, C. L. 2002 Cycle detection and characterization in chemical engineering. *AIChE Journal* 48 (5), 970–980.

Chaplin, G., Pugsley, T. & Winters, C. 2004 Application of chaos analysis to pressure fluctuation data from a fluidized bed dryer containing pharmaceutical granule. *Powder Technology* 142 (2-3), 110–120.

D'Amore, M., Donsi, G. & Massimilla, L. 1979 The influence of bed moisture on fluidization characteristics of fine powders. *Powder Technology* 23 (2), 253–259.

Daud, W. R. W. 2008 Fluidized bed dryers - recent advances. *Advanced Powder Technology* 19 (5), 403–418.

Dong, P., Li, Z., Gao, X., Wu, Z. & Zheng, Z. 2013 Evaluation of hydrodynamic behavior of a fluidized bed dryer by analysis of pressure fluctuation. *Drying Technology* 31 (10), 1170–1176.

Freire, J. T., Ferreira, M. C., Freire, F. B. & Nascimento, B. S. 2012 A review on paste drying with inert particles as support medium. *Drying Technology* 30 (4), 330–341.

Geldart, D. 1973 Types of gas fluidization. *Powder Technology* 7 (5), 285–292.

Gómez-Hernández, J., Sanchez-Prieto, J., Briongos, J. Villa & Santana, D. 2014 Wide band energy analysis of fluidized bed pressure fluctuations signals using frequency a division methodology. *Chemical Engineering Science* 105, 92–103.

Gómez-Hernández, J., Soria-Verdugo, A., Briongos, J. Villa & Santana, D. 2012 Fluidized bed with a rotating distributor operated under defluidization conditions. *Chemical Engineering Journal* 195-196 (0), 198–207.

Johnsson, F., Zijerveld, R. C., Schouten, J. C., van den Bleek, C. M. & Leckner, B. 2000 Characterization of fluidization regimes by time-series analysis of pressure fluctuations. *International Journal of Multiphase Flow* 26 (4), 663–715.

Kannan, C.S., Rao, S.S. & Varma, Y.B.G. 1994 A kinetic-model for drying of solids in batch fluidized-beds. *Industrial Engineering Chemistry Research* 33 (2), 363–370.

Kudra, T., Gawrzynski, Z., Glaser, R., Stanislawski, J. & Poirier, M. 2002 Drying of pulp and paper sludge in a pulsed fluid bed dryer. *Drying Technology* 20 (4-5), 917–933.

Kulkarni, A. A., Joshi, J. B., Kumar, V. R. & Kulkarni, B. D. 2001 Application of multiresolution analysis for simultaneous measurement of gas and liquid velocities and fractional gas hold-up in bubble column using lda. *Chemical Engineering Science* 56 (17), 5037–5048.

Lee, D. H. & Kim, S. D. 1993 Drying characteristics of starch in an inert medium fluidized bed. *Chemical Engineering and Technology* 16 (4), 263–269.

de Martin, L., van den Dries, K. & van Ommen, J. R. 2011 Comparison of three different methodologies of pressure signal processing to monitor fluidized-bed dryers/granulators. *Chemical Engineering Journal* 172 (1).

Mujumdar, A. S. 2006 *Handbook of Industrial Drying*. Taylor & Francis.

van Ommen, J. R., de Korte, R. J. & van den Bleek, C. M. 2004 Rapid detection of defluidization using the standard deviation of pressure fluctuations. *Chemical Engineering and Processing* 43 (10), 1329–1335.

van Ommen, J. R., Sasic, S., van der Schaaf, J., Gheorghiu, S., Johnsson, F. & Coppens, M. O. 2011 Time-series analysis of pressure fluctuations in gas-solid fluidized beds - a review. *International Journal of Multiphase Flow* 37 (5), 403–428.

van Ommen, J. R., Schouten, J. C., vander Stappen, M. L. M. & van den Bleek, C. M. 1999 Response characteristics of probe-transducer systems for pressure measurements in gas-solid fluidized beds: how to prevent pitfalls in dynamic pressure measurements. *Powder Technology* 106 (3), 199–218.

Pan, Y. K., Li, J. G., Zhao, L. J., Ye, W. H., Mujumdar, A. S. & Kudra, T. 2001 Performance characteristics of the vibrated fluid bed of inert particles for drying of liquid feeds. *Drying Technology* 19 (8), 2003–2018.

Reay, D. & Baker, C. G. J. 1985 *Fluidization*, 2nd edn. London: Academic Press.

Reyes, A., Diaz, G. & Marquardt, F. H. 2001 Analysis of mechanically agitated fluid-particle contact dryers. *Drying Technology* 19 (9), 2235–2259.

Sasic, S., Leckner, B. & Johnsson, F. 2006 Time-frequency investigation of different modes of bubble flow in a gas-solid fluidized bed. *Chemical Engineering Journal* 121 (1), 27–35.

Shin, Y. S., Kim, H. C. & Chun, H. S. 2000 Drying of water treatment process sludge in a fluidized bed dryer. *Korean Journal of Chemical Engineering* 17 (1), 22–26.

Sobrino, C., Acosta-Iborra, A., Santana, D. & de Vega, M. 2009 Bubble characteristics in a bubbling fluidized bed with a rotating distributor. *International Journal of Multiphase Flow* 35 (10), 970–976.

Stappen, M. L. M. Vander 1996 *Chaotic hydrodynamics of fluidized beds*. Delft University of Technology.

Tatemoto, Y. & Miyazawa, K. 2011 Drying of suspensions in a fluidized bed of inert particles under reduced pressure. *Drying Technology* 29 (10), 1204–1209.

Wang, Z. H. & Chen, G. H. 2000 Heat and mass transfer in batch fluidized-bed drying of porous particles. *Chemical Engineering Science* 55 (10), 1857–1869.

Watano, S., Yeh, N. & Miyanami, K. 1998 Drying of granules in agitation fluidized bed. *Journal of Chemical Engineering of Japan* 31 (6), 908–913.

Wormsbecker, M., van Ommen, J. R., Nijenhuis, J., Tanfara, H. & Pugsley, T. 2009*a* The influence of vessel geometry on fluidized bed dryer hydrodynamics. *Powder Technology* 194 (1-2).

Wormsbecker, M., T.Pugsley & Tanfara, H. 2009*b* Interpretation of the hydrodynamic behaviour in a conical fluidized bed dryer. *Chemical Engineering Science* 64 (8), 1739–1746.

Yang, T. Y. & Leu, L. P. 2008 Multi-resolution analysis of wavelet transform on pressure fluctuations in an l-valve. *International Journal of Multiphase Flow* 34 (6), 567–579.

Zhao, G. B. & Yang, Y. R. 2003 Multiscale resolution of fluidized-bed pressure fluctuations. *AIChE Journal* 49 (4), 869–882.

Zhao, L. J., Pan, Y. K., Li, J. G., Chen, G. H. & Mujumdar, A. S. 2004 Drying of a dilute suspension in a revolving flow fluidized bed of inert particles. *Drying Technology* 22 (1-2), 363–376.

CHAPTER

SIX

Conclusions

This PhD thesis presents the development and application of the tools needed to characterize a fluidized bed equipped with a rotating distributor for drying applications. These tools are focused on analysis of the pressure time-series and in the design of a monitoring scheme to control the drying tests. Thus, the results are related, on the one hand, with the development of diagnosis and control tools for the study of the operational conditions in a fluidized bed, and, on the other hand, with the improvements found using the rotating distributor in processes with defluidization problems caused by the formation of agglomerates.

Regarding the tools developed, a new methodology for the unbiased and systematical frequency division was proposed in Chapter 3. The reliability of the method was verified for different fluidization velocities, changing the bed aspect ratio and using different pressure probes. The results showed that the frequency limits varied as a function of the fluidization conditions, changing the physical meaning of the frequency regions. The computation of the wide band energy in these frequency regions demonstrated the capability of the new approach to be used as a monitoring tool for agglomeration processes, since it permitted the detection of channel formation and the bed defluidization. The control of the fluidization behavior was carried out by means of the Statistical Process Control theory using variables obtained in both the time and frequency domains. This control scheme presented in Chapter 4 is proposed for the continuous control of a fluidized bed. Methods for determining the window length and the underlying distribution used to compute the control limits were established. The results verified that the definition of the control state improved the detection of slight deviations from the control state.

The rotating distributor introduced a dynamic structure on the fluidized bed. As shown in Chapter 2, the effect of the rotating distributor improves the breakage of the agglomerates located in the region close to the distributor. This

influence difficults the appearance of channels, and thus, reduces the risk of the bed defluidization. Following this result, Chapter 5 presented the application of the rotating distributor to a paste drying process, which was analyzed using the tools developed in Chapters 3 and 4. A comparison between the static and the rotating distributor tests showed clear benefits for the operation with the rotating distributor both for shallow and deep beds: the maximum drying rate was increased, the drying time was reduced and the recuperation of the fluidization quality for all the bed aspect ratios tested was more homogeneous.

Alphabetical list of references

Adamiec, J. 2002 Drying of waste sludges in a fluidized bed dryer with a mixer. *Drying Technology* 20 (4-5), 839–853.

Adris, A. E M. & Grace, J. R. 1997 Characteristics of fluidized-bed membrane reactors: Scale-up and practical issues. *Industrial & Engineering Chemistry Research* 36 (11), 4549–4556.

Agarwal, G., Lattimer, B., Ekkad, S. & Vandsburger, U. 2011 Influence of multiple gas inlet jets on fluidized bed hydrodynamics using particle image velocimetry and digital image analysis. *Powder Technology* 214 (1), 122–134.

Aguado, R., Prieto, R., Jose, M. J. San, Alvarez, S., Olazar, M. & Bilbao, J. 2005 Defluidization modelling of pyrolysis of plastics in a conical spouted bed reactor. *Chemical Engineering and Processing* 44 (2), 231–235.

Akhavan, A., van Ommen, J. R., Nijenhuis, J., Wang, X. S., Coppens, M. O. & Rhodes, M. J. 2009 Improved drying in a pulsation-assisted fluidized bed. *Industrial & Engineering Chemistry Research* 48 (1), 302–309.

Amos, G., Rhodes, M. J. & Benkreira, H. 1996 Calculation of optic fibres calibration curves for the measurement of solids volume fractions in multiphase flows. *Powder Technology* 88 (2), 107–121.

Ariyapadi, S., Holdsworth, D. W., Norley, C. J. D., Berruti, F. & Briens, C. 2003 Digital x-ray imaging technique to study the horizontal injection of gas-liquid jets into fluidized beds. *International Journal of Chemical Reactor Engineering* 1.

Atthajariyakul, S. & Leephakpreeda, T. 2006 Fluidized bed paddy drying in optimal conditions via adaptive fuzzy logic control. *Journal of Food Engineering* 75 (1), 104–114.

Barletta, M., Gisario, A., Guarino, S. & Tagliaferri, V. 2008 Fluidized bed coating of metal substrates by using high performance thermoplas-

tic powders: Statistical approach and neural network modelling. *Engineering Applications of Artificial Intelligence* 21 (8), 1130–1143.

Bartels, M., Lin, W., Nijenhuis, J., Kapteijn, F. & van Ommen, J. R. 2008 Agglomeration in fluidized beds at high temperatures: Mechanisms, detection and prevention. *Progress in Energy and Combustion Science* 34 (5), 633–666.

Bartels, M., Vermeer, B., Nijenhuis, J. & Kapteijn, F. 2009 Methodology for the screening of signal analysis methods for selective detection of hydrodynamic changes in fluidized bed systems. *Industrial & Engineering Chemistry Research* 48 (6), 3158–3166.

Baskakov, A. P., Tuponogov, V. G. & Filippovsky, N. F. 1986 A study of pressure-fluctuations in a bubbling fluidized-bed. *Powder Technology* 45 (2), 113–117.

Book, G., Albion, K., Briens, L., Briens, C. & Berruti, F. 2011 Online detection of bed fluidity in gas-solid fluidized beds with liquid injection by passive acoustic and vibrometric methods. *Powder Technology* 205 (1-3), 126–136.

Briens, L. & Bojarra, M. 2010 Monitoring fluidized bed drying of pharmaceutical granules. *AAPS PharmSciTech* 11 (4), 1612–1618.

Briens, L. A. & Briens, C. L. 2002 Cycle detection and characterization in chemical engineering. *AIChE Journal* 48 (5), 970–980.

Briongos, J. Villa & Soler, J. G. 2003 Free top fluidized bed surface fluctuations as a source of hydrodynamic data. *Powder Technology* 134 (1-2), 133–144.

Brouwer, G. C., Wagner, E. C., van Ommen, J. R. & Mudde, R. F. 2012 Effects of pressure and fines content on bubble diameter in a fluidized bed studied using fast x-ray tomography. *Chemical Engineering Journal* 207-208 (0), 711–717.

Brown, R. C. & Brue, E. 2001 Resolving dynamical features of fluidized beds from pressure fluctuations. *Powder Technology* 119 (2-3), 68–80.

Bruhns, S. & Werther, J. 2005 An investigation of the mechanism of liquid injection into fluidized beds. *AIChE Journal* 51 (3), 766–775.

Burggraeve, A., den Kerkhof, T. Van, Hellings, M., Remon, J. P., Vervaet, C. & Beer, T. De 2011 Batch statistical process control of a fluid bed granulation process using in-line spatial filter velocimetry and product temperature measurements. *European Journal of Pharmaceutical Sciences* 42 (5), 584–592.

Chaplin, G., Pugsley, T. & Winters, C. 2004 Application of chaos analysis to pressure fluctuation data from a fluidized bed dryer containing pharmaceutical granule. *Powder Technology* 142 (2-3), 110–120.

Chilekar, V. P., Warnier, M. J. F., van der Schaaf, J., Kuster, B. F. M., Schouten, J. C. & van Ommen, J. R. 2005 Bubble size estimation in slurry bubble columns from pressure fluctuations. *AIChE Journal* 51 (7), 1924–1937.

Chong, Y.O., Odea, D.P., White, E.T., Lee, P.L. & Leung, L.S. 1987 Control of the quality of fluidization in a tall bed using the variance of pressure-fluctuations. *Powder Technology* 53 (3), 237–246.

Croxford, A. J. & Gilbertson, M. A. 2006 Control of the state of a bubbling fluidised bed. *Chemical Engineering Science* 61 (19), 6302–6315.

D'Amore, M., Donsi, G. & Massimilla, L. 1979 The influence of bed moisture on fluidization characteristics of fine powders. *Powder Technology* 23 (2), 253–259.

Daud, W. R. W. 2008 Fluidized bed dryers - recent advances. *Advanced Powder Technology* 19 (5), 403–418.

Davies, C. E., Carroll, A. & Flemmer, R. 2008 Particle size monitoring in a fluidized bed using pressure fluctuations. *Powder Technology* 180 (3), 307–311.

Dempster, A.P. 1977 Maximum likelihood from incomplete data via em algorithm. *Journal of the Royal Statistical Society.Series B, Methodological* 39 (1), 1–38.

Dong, P., Li, Z., Gao, X., Wu, Z. & Zheng, Z. 2013 Evaluation of hydrodynamic behavior of a fluidized bed dryer by analysis of pressure fluctuation. *Drying Technology* 31 (10), 1170–1176.

Ergudenler, A. & Ghaly, A. E. 1993 Agglomeration of silica sand in a fluidized-bed gasifier operating on wheat straw. *Biomass & Bioenergy* 4 (2), 135–147.

Faure, A., York, P. & Rowe, R. C. 2001 Process control and scale-up of pharmaceutical wet granulation processes: a review. *European Journal of Pharmaceutics and Biopharmaceutics* 52 (3), 269–277.

Felipe, C. A. S. & Rocha, S. C. S. 2007 Prediction of minimum fluidization velocity of gas-solid fluidized beds by pressure fluctuation measurements - analysis of the standard deviation methodology. *Powder Technology* 174 (3), 104–113.

Fisher, R. A. 1925 Theory of statistical estimation. *Mathematical Proceedings of the Cambridge Philosophical Society* 22 (05), 700.

Freire, J. T., Ferreira, M. C., Freire, F. B. & Nascimento, B. S. 2012 A review on paste drying with inert particles as support medium. *Drying Technology* 30 (4), 330–341.

Geldart, D. 1973 Types of gas fluidization. *Powder Technology* 7 (5), 285–292.

Gómez-Hernández, J., Sanchez-Prieto, J., Briongos, J. Villa & Santana, D. 2014 Wide band energy analysis of fluidized bed pressure fluctuations signals using frequency a division methodology. *Chemical Engineering Science* 105, 92–103.

Gómez-Hernández, J., Soria-Verdugo, A., Briongos, J. Villa & Santana, D. 2012 Fluidized bed with a rotating distributor operated under defluidization conditions. *Chemical Engineering Journal* 195-196 (0), 198–207.

Haynes, M., Mengersen, K. & Rippon, P. 2008 Generalized control charts for non-normal data using g-and-k distributions. *Communications in Statistics-Simulation and Computation* 37 (9), 1881–1903.

Heindel, T. J. 2011 A review of x-ray flow visualization with applications to multiphase flows. *Journal of Fluids Engineering* 133 (7), 074001–074001.

Herrera, C. A., Levy, E. K. & Ochs, J. 2002 Characteristics of acoustic standing waves in fluidized beds. *AIChE Journal* 48 (3), 503–513.

Horio, M., Kiyota, H. & Muchi, I. 1980 Particle movement on a perforated plate distributor of fluidized-bed. *Journal of Chemical Engineering of Japan* 13 (2), 137–142.

Hristov, J. 2002 Magnetic field assisted fluidization a unified approach - part 1. fundamentals and relevant hydrodynamics of gas-fluidized beds (batch solids mode). *Reviews in Chemical Engineering* 18 (4-5), 295–509.

Janacek, G. J. & Meikle, S. E. 1997 Control charts based on medians. *Journal of the Royal Statistical Society: Series D (The Statistician)* 46 (1), 19–31.

Johnson, N. L. & Kotz, S. 1970 *Continuous Univariate Distributions, Volume 1*. John Wiley & Sons.

Johnsson, F., Zijerveld, R. C., Schouten, J. C., van den Bleek, C. M. & Leckner, B. 2000 Characterization of fluidization regimes by time-series analysis of pressure fluctuations. *International Journal of Multiphase Flow* 26 (4), 663–715.

Jose, M. J. San, Olazar, M., Alvarez, S., Izquierdo, M. A. & Bilbao, J. 1994 Segregation in conical spouted beds with binary and ternary mixtures of equidensity spherical particles. *Industrial & Engineering Chemistry Research* 33 (7), 1838–1844.

Kage, H., Agari, M., Ogura, H. & Matsuno, Y. 2000 Frequency analysis of pressure fluctuation in fluidized bed plenum and its confidence limit for detection of various modes of fluidization. *Advanced Powder Technology* 11 (4), 459–475.

Kannan, C.S., Rao, S.S. & Varma, Y.B.G. 1994 A kinetic-model for drying of solids in batch fluidized-beds. *Industrial Engineering Chemistry Research* 33 (2), 363–370.

Kano, M., Hasebe, S., Hashimoto, I. & Ohno, H. 2004 Evolution of multivariate statistical process control: application of independent component analysis and external analysis. *Computers & Chemical Engineering* 28 (6-7), 1157–1166.

Kudra, T., Gawrzynski, Z., Glaser, R., Stanislawski, J. & Poirier, M. 2002 Drying of pulp and paper sludge in a pulsed fluid bed dryer. *Drying Technology* 20 (4-5), 917–933.

Kulkarni, A. A., Joshi, J. B., Kumar, V. R. & Kulkarni, B. D. 2001 Application of multiresolution analysis for simultaneous measurement of gas and liquid velocities and fractional gas hold-up in bubble column using lda. *Chemical Engineering Science* 56 (17), 5037–5048.

Lee, D. H. & Kim, S. D. 1993 Drying characteristics of starch in an inert medium fluidized bed. *Chemical Engineering and Technology* 16 (4), 263–269.

Lim, H. O., Seo, M. J. & Kang, Y. 2010 Drying of thermally-weak organic powder in a centrifugal fluidized bed. *Advanced Powder Technology* 21 (2), 131–135.

Lin, W. G., Dam-Johansen, K. & Frandsen, F. 2003 Agglomeration in bio-fuel fired fluidized bed combustors. *Chemical Engineering Journal* 96 (1-3), 171–185.

Liu, Y., Peng, J., Kansha, Y., Ishizuka, M., Tsutsumi, A., Jia, D., Bi, X. T., Lim, C. J. & Sokhansanj, S. 2014 Novel fluidized bed dryer for biomass drying. *Fuel Processing Technology* 122, 170–175.

de Martin, L., Briongos, J. Villa, Aragon, J. M. & Palancar, M. C. 2010 Can low frequency accelerometry replace pressure measurements for monitoring gas-solid fluidized beds? *Chemical Engineering Science* 65 (13), 4055–4064.

de Martin, L., van den Dries, K. & van Ommen, J. R. 2011 Comparison of three different methodologies of pressure signal processing to monitor fluidized-bed dryers/granulators. *Chemical Engineering Journal* 172 (1).

McDougall, S., Saberian, M., Briens, C., Berruti, F. & Chan, E. 2005 Effect of liquid properties on the agglomerating tendency of a wet gas-solid fluidized bed. *Powder Technology* 149 (2-3), 61–67.

Mcfarlane, R. C., Hoffman, T. W., Taylor, P. A. & Macgregor, J. F. 1983 Control of fluidized-bed reactors.1. modeling, simulation, and single-loop control studies. *Industrial & Engineering Chemistry Process Design and Development* 22 (1).

Meili, L., Daleffe, R. V., Ferreira, M. C. & Freire, J. T. 2010 Analysis of the influence of dimensionless vibration number on the drying of pastes in vibrofluidized beds. *Drying Technology* 28 (3), 402–411.

Mettanant, V., Basu, P. & Butler, J. 2009 Agglomeration of biomass fired fluidized bed gasifier and combustor. *Canadian Journal of Chemical Engineering* 87 (5), 656–684.

Molerus, O. 1982 Interpretation of geldart type-a, type-b, type-c and type-d powders by taking into account interparticle cohesion forces. *Powder Technology* 33 (1), 81–87.

Montgomery, D. C. 1997 *Introduction to statistical quality control*, 3rd edn. New York: John Wiley & Sons, Inc.

Mujumdar, A. S. 2006 *Handbook of Industrial Drying*. Taylor & Francis.

Nakagawa, N., Ohsawa, K., Takarada, T. & Kato, K. 1992 Continuous drying of a fine particles-water slurry in a powder-particle fluidized-bed. *Journal of Chemical Engineering of Japan* 25 (5), 495–501.

Nakamura, H. & Watano, S. 2008 Fundamental particle fluidization behavior and handling of nano-particles in a rotating fluidized bed. *Powder Technology* 183 (3), 324–332.

Nordin, A., Ohman, M., Skrifvars, B. J. & Hupa, M. 1996 Agglomeration and defluidization in fbc of biomass fuels- mechanism and measures for prevention. In *Applications of Advanced Technology to Ash-Related Problems in Boilers* (ed. L. Baxter & R. DeSollar), pp. 353–366. Springer.

Ohman, M., Nordin, A., Skrifvars, B. J., Backman, R. & Hupa, M. 2000 Bed agglomeration characteristics during fluidized bed combustion of biomass fuels. *Energy & Fuels* 14 (1), 169–178.

van Ommen, J. R., Coppens, M. O., van den Bleek, C. M. & Schouten, J. C. 2000 Early warning of agglomeration in fluidized beds by attractor comparison. *AIChE Journal* 46 (11), 2183–2197.

van Ommen, J. R., de Korte, R. J. & van den Bleek, C. M. 2004 Rapid detection of defluidization using the standard deviation of pressure fluctuations. *Chemical Engineering and Processing* 43 (10), 1329–1335.

van Ommen, J. R., Nijenhuis, J., van den Bleek, C. M. & Coppens, M. O. 2007 Four ways to introduce structure in fluidized bed reactors. *Industrial & Engineering Chemistry Research* 46 (12), 4236–4244.

van Ommen, J. R., Sasic, S., van der Schaaf, J., Gheorghiu, S., Johnsson, F. & Coppens, M. O. 2011 Time-series analysis of pressure fluctuations in gas-solid fluidized beds - a review. *International Journal of Multiphase Flow* 37 (5), 403–428.

van Ommen, J. R., Schouten, J. C., vander Stappen, M. L. M. & van den Bleek, C. M. 1999 Response characteristics of probe-transducer systems for pressure measurements in gas-solid fluidized beds: how to prevent pitfalls in dynamic pressure measurements. *Powder Technology* 106 (3), 199–218.

Pan, Y. K., Li, J. G., Zhao, L. J., Ye, W. H., Mujumdar, A. S. & Kudra, T. 2001 Performance characteristics of the vibrated fluid bed of inert particles for drying of liquid feeds. *Drying Technology* 19 (8), 2003–2018.

Parise, M. R., Silva, C. A. M., Ramazini, M. J. & Taranto, O. P. 2011 Identification of defluidization in fluidized bed coating using the gaussian spectral pressure distribution. *Powder Technology* 206 (1-2), 149–153.

Polansky, A. M. 2005 A general framework for constructing control charts. *Quality and Reliability Engineering International* 21 (6), 633–653.

Puncochar, M., Drahos, J., Cermak, J. & Selucka, K. 1985 Evaluation of minimum fluidization velocity in gas fluidized beds from pressure fluctuations. *Chemical Engineering Communications* 35 (1-6), 81–87.

Quevedo, J., Pfeffer, R., Shen, Y., Dave, R., Nakamura, H. & Watano, S. 2006 Fluidization of nanoagglomerates in a rotating fluidized bed. *AIChE Journal* 52 (7), 2401–2412.

Reay, D. & Baker, C. G. J. 1985 *Fluidization*, 2nd edn. London: Academic Press.

Reyes, A., Diaz, G. & Marquardt, F. H. 2001 Analysis of mechanically agitated fluid-particle contact dryers. *Drying Technology* 19 (9), 2235–2259.

Ruthiya, K. C., Chilekar, V. P., Warnier, M. J. F., van der Schaaf, J., Kuster, B. F. M., Schouten, J. C. & van Ommen, J. R. 2005 Detecting regime transitions in slurry bubble columns using pressure time series. *AIChE Journal* 51 (7), 1951–1965.

Sasic, S., Leckner, B. & Johnsson, F. 2006 Time-frequency investigation of different modes of bubble flow in a gas-solid fluidized bed. *Chemical Engineering Journal* 121 (1), 27–35.

van der Schaaf, J., Johnsson, F., Schouten, J. C. & van den Bleek, C. M. 1999 Fourier analysis of nonlinear pressure fluctuations in gas-solids flow in cfb risers - observing solids structures and gas/particle turbulence. *Chemical Engineering Science* 54 (22), 5541–5546.

van der Schaaf, J., van Ommen, J. R., Takens, F., Schouten, J. C. & van den Bleek, C. M. 2004 Similarity between chaos analysis and frequency analysis of pressure fluctuations in fluidized beds. *Chemical Engineering Science* 59 (8-9), 1829–1840.

van der Schaaf, J., Schouten, J. C. & van den Bleek, C. M. 1998 Origin, propagation and attenuation of pressure waves in gas-solid fluidized beds. *Powder Technology* 95 (3), 220–233.

van der Schaaf, J., Schouten, J. C., Johnsson, F. & van den Bleek, C. M. 2002 Non-intrusive determination of bubble and slug length scales in fluidized beds by decomposition of the power spectral density of pressure time series. *International Journal of Multiphase Flow* 28 (5), 865–880.

Schouten, J. C. & van den Bleek, C. M. 1998 Monitoring the quality of fluidization using the short-term predictability of pressure fluctuations. *AIChE Journal* 44 (1), 48–60.

Shewhart, W. A. 1925 The application of statistics as an aid in maintaining quality of a manufactured product. *Journal of the American Statistical Association* 20, 546–548.

Shewhart, W. A. 1930 Economic quality control of manufactured product. *Bell System Technical Journal* 9 (2).

Shin, Y. S., Kim, H. C. & Chun, H. S. 2000 Drying of water treatment process sludge in a fluidized bed dryer. *Korean Journal of Chemical Engineering* 17 (1), 22–26.

Silva, C. A. M., Parise, M. R., Silva, F. V. & Taranto, O. P. 2011 Control of fluidized bed coating particles using gaussian spectral pressure distribution. *Powder Technology* 212 (3), 445–458.

Silvennoinen, J. 2003 A new method to inhibit bed agglomeration problems in fluidized bed boilers. *ASME Conference Proceedings* 2003, 377–385.

Sobrino, C., Acosta-Iborra, A., Santana, D. & de Vega, M. 2009 Bubble characteristics in a bubbling fluidized bed with a rotating distributor. *International Journal of Multiphase Flow* 35 (10), 970–976.

Sobrino, C., Almendros-Ibanez, J. A., Santana, D. & Vega, M. De 2008 Fluidization of group b particles with a rotating distributor. *Powder Technology* 181 (3), 273–280.

Soria-Verdugo, A., Garcia-Hernando, N., Almendros-Ibanez, J. A. & Ruiz-Rivas, U. 2011 Motion of a large object in a bubbling fluidized bed with a rotating distributor. *Chemical Engineering and Processing* 50 (8), 859–868.

vander Stappen, M. L. M. 1996 Chaotic hydrodynamics of fluidized beds.

Stephens, M. A. 1970 Use of komogorov-smirnov,cramer-von mises and related statistics without extensive tables. *Journal of the Royal Statistical Society Series B-Statistical Methodology* 32 (1), 115–&.

Tatemoto, Y. & Miyazawa, K. 2011 Drying of suspensions in a fluidized bed of inert particles under reduced pressure. *Drying Technology* 29 (10), 1204–1209.

Vermaat, M. B., Ion, R. A., Does, R. J. M. M. & Klaassen, C. A. J. 2003 A comparison of shewhart individuals control charts based on normal, non-parametric, and extreme-value theory. *Quality and Reliability Engineering International* 19 (4), 337–353.

Visser, H. J. M., van Lith, S. C. & Kiel, J. H. A. 2008 Biomass ash-bed material interactions leading to agglomeration in fbc. *Journal of Energy Resources Technology* 130 (1), 011801.

Wang, Z. H. & Chen, G. H. 2000 Heat and mass transfer in batch fluidized-bed drying of porous particles. *Chemical Engineering Science* 55 (10), 1857–1869.

Watano, S., Yeh, N. & Miyanami, K. 1998 Drying of granules in agitation fluidized bed. *Journal of Chemical Engineering of Japan* 31 (6), 908–913.

Welch, P. 1967 The use of fast fourier transform for the estimation of power spectra: a method based on time averaging over short, modified periodograms. *IEEE Transactions on Audio and Electroacoustics* 15 (2), 70.

Werther, J. 1999 Measurement techniques in fluidized beds. *Powder Technology* 102 (1), 15–36.

Wilkinson, D. 1995 Determination of minimum fluidization velocity by pressure fluctuation measurement. *Canadian Journal of Chemical Engineering* 73 (4), 562–565.

van Willigen, F. K., Christensen, D., van Ommen, J. R. & Coppens, M. O. 2005 Imposing dynamic structures on fluidised beds. *Catalysis Today* 105 (3-4), 560–568.

van Willigen, F. K., van Ommen, J. R., Turnhout, J. Van & Bleek, C. M. Van Den 2004 Bubble size reduction in electric-field-enhanced fluidized beds. In *AIChE Annual Meeting, Conference Proceedings*, pp. 2795–2799.

Wormsbecker, M., van Ommen, J. R., Nijenhuis, J., Tanfara, H. & Pugsley, T. 2009*a* The influence of vessel geometry on fluidized bed dryer hydrodynamics. *Powder Technology* 194 (1-2).

Wormsbecker, M., Pugsley, T. & Tanfara, H. 2009*b* Interpretation of the hydrodynamic behaviour in a conical fluidized bed dryer. *Chemical Engineering Science* 64 (8), 1739–1746.

Xie, C. G., Huang, S. M., Hoyle, B. S., Thorn, R., Lenn, C., Snowden, D. & Beck, M. S. 1992 Electrical capacitance tomography for flow imaging - system model for development of image-reconstruction algorithms and design of primary sensors. *IEE Proceedings-G Circuits Devices and Systems* 139 (1), 89–98.

Yan, R., Liang, D. T., Laursen, K., Li, Y., Tsen, L. & Tay, J. H. 2003 Formation of bed agglomeration in a fluidized multi-waste incinerator. *Fuel* 82 (7), 843–851.

Yang, T. Y. & Leu, L. P. 2008 Multi-resolution analysis of wavelet transform on pressure fluctuations in an l-valve. *International Journal of Multiphase Flow* 34 (6), 567–579.

Yourstone, S. A. & Zimmer, W. J. 1992 Nonnormality and the design of control charts for averages. *Decision Sciences* 23 (5), 1099–1113.

Zhao, G. B. & Yang, Y. R. 2003 Multiscale resolution of fluidized-bed pressure fluctuations. *AIChE Journal* 49 (4), 869–882.

Zhao, L. J., Pan, Y. K., Li, J. G., Chen, G. H. & Mujumdar, A. S. 2004 Drying of a dilute suspension in a revolving flow fluidized bed of inert particles. *Drying Technology* 22 (1-2), 363–376.

List of publications

The results of this PhD thesis have been published in the following papers:

- Gómez-Hernández, J., Soria-Verdugo, A., Villa Briongos, J. & Santana, D. 2012 Fluidized bed with a rotating distributor operated under defluidization conditions. *Chemical Engineering Journal* 195-196,(0) 198 - 207.

- Gómez-Hernández, J., Sánchez-Prieto, J., Villa Briongos, J. & Santana, D. 2014 Wide band energy analysis of fluidized bed pressure fluctuation signals using a frequency division method. *Chemical Engineergin Science* 105, 92 - 103.

- Gómez-Hernández, J., Soria-Verdugo, A., Villa Briongos, J. & Santana, D. 2014 Statistical Process Control of fluidized beds: Application to paste drying process. *Submitted for publication in Powder Technology.*

- Gómez-Hernández, J., Soria-Verdugo, A., Villa Briongos, J. & Santana, D. 2014 Multi-resolution analysis of paste drying in a rotating-distributor fluidized bed. *Submitted for publication in Drying Technology.*

and presented in the following conference:

- Gómez-Hernández, J., Soria-Verdugo, A., Villa Briongos, J. & Santana, D. 2013 Design of a Statistical Strategy to the Control of a Fluidized Bed Equipped with a Rotating Distributor. In *The 14th International Conference on Fluidization - From Fundamentals to Products.*

Other works of the author are:

- Villa Briongos, J., Sobrino, C., Gómez-Hernández, J. & Santana, D. 2013 Characterization of flow-induced vibrations in gas-solid fluidized beds: Elements of the theory. *Chemical Engineering Science* 93, 181 - 196.

- Gómez-Hernández, J., van Ommen, J. R., Wagner, E.C., & Mudde, R. F. 2014 A fast reconstruction algorithm for time-resolved X-ray tomography in bubbling fluidized beds. *Submitted for publication in Powder Technology.*